Sea of Electrodes Array (SEA): Customizable 3D High-Density High-Count Neural Probe Array Technology

by

Seyed Amin Sandoughsaz Zardini

A dissertation submitted in partial fulfillment
of the requirements for the degree of
Doctor of Philosophy
(Electrical Engineering)
in the University of Michigan
2019

Doctoral Committee:

Professor Khalil Najafi, Chair
Assistant Professor Omar J. Ahmed
Professor Yogesh Gianchandani
Professor Emeritus Kensall D. Wise

Seyed Amin Sandoughsaz Zardini

aminsa@umich.edu

ORCID iD: 0000-0003-1290-1466

DEDICATION

To my parents, Shahrbanoo and Mahmoud

To my sister, Fatemeh

and in the loving memory of my great-grandmother, Khanum Sultan

ACKNOWLEDGMENTS

First and foremost I would like to thank my advisor, Professor Khalil Najafi. He is truly a role model for leadership with integrity. He taught me that low-hanging fruits are not worth pursuing and gave me the opportunity to try, fail and learn throughout my PhD studies. His intelligence, passion for learning, and humane and humble attitude towards others have always been inspiring for me. Working with him is one of the best things that happened in my life.

I would like to thank my other thesis committee members, Professor Kensall Wise, Professor Yogesh Gianchandani and Professor Omar Ahmed for their time and valuable comments on my thesis. In particular, I would like to express my sincere appreciation to Professor Omar Ahmed and Vaughn Hetrick for conducting the *in vivo* experiments and useful discussions.

I would like to thank all my former and present friends and colleagues in WIMS^2 center for all their help, friendship and support. In particular, I'd like to thank Dr. Ali Darvishian, Dr. Mahdi Sadeghi, Mr. Sajal Singh, Ms. Behnoush Rostami, Dr. Tal Nagourney, Dr. Stacey Tang, Dr. Jae Yoong Cho, Dr. Ali Besharatian and Dr. Daniel Egert. I would like to thank the staff of the Lurie Nanofabrication Facility (LNF) for all their help and support.

I had an amazing time in Ann Arbor thanks to all my wonderful friends. In particular, I would like to thank Ali Darvishian, for being an incredibly nice and supportive friend, and Rebecca, for all her support and encouragement and all the amazing time we had together over the past couple of years.

Last but not least, I wish to thank my parents, my sister, my brother-in-law and my lovely nieces for their unconditional love and support. Words can't express my love for them!

iii

TABLE OF CONTENTS

LIST OF TABLES

LIST OF FIGURES

ABSTRACT

Accurate mapping of neural circuits and interfacing with neurons for control of brain-machine interfaces require simultaneous large-scale and high spatiotemporal resolution recordings and stimulation of neurons in multiple layers and areas of the brain. Conventional penetrating micro-electrode arrays (MEAs) are limited to a few thousand electrodes at best, with limited volumetric 3D spatial resolution. This is mainly due to the types of fabrication technologies and available designs and materials for making such probes. Based on the strengths and shortcomings of the available MEAs, we present a new fabrication technology for a new class of 3D neural electrode array that provides the characteristics of a near-ideal neural interface.

This research addresses some of the limitations of previous works in terms of electrode scale, density and spatial coverage (depth and span). In order to realize a scalable 3D out-of-plane array of extremely dense, slender, and sharp needles with recording sites at each of their tips, a number of techniques are developed. These includes: 1- A custom-developed silicon DRIE process to make deep (500 µm) high aspect-ratio (20-30) thru-wafer holes with controlled sidewall slope, 2- A method of extending the thru-wafer holes depth by aligning and then fusion bonding multiple silicon substrates already having holes etched in them, 3- A process for conformal refilling of ultra-deep (~2 mm) ultra-high aspect-ratio (80-100) holes with dielectric and conductive films using LPCVD process, 4- Methods of forming recording sites using self-aligned mask-less metallization processes, and 5- A method based on wet silicon etching to dissolve away the support substrate containing the refilled holes to release the electrodes.

Using these technologies, we have fabricated millimeter-long (1.2mm), narrow (10-20µm diameter), sharp (submicron tip size), high-density (400 electrodes/mm^2) high-count (5000+) silicon electrode arrays. Electrodes robustness, insertion and recording functionality have been demonstrated by acute *in vivo* recordings in rats under anesthesia using 2×2 and 3×3 arrays, where local field potentials (LFP) have been recorded.

Innovative features of this technology could be utilized to produce arrays with arbitrary 3D design to target specific brain structures to achieve 3D spatial coverage over the convoluted topography of the brain. These include: 1- Length of side-by-side electrodes can be varied from tens of microns to several millimeters independently. 2- Electrodes spacing can be modified by the designer to obtain a desirable density and distribution of the array needles. 3- Electrode cross-sectional size can be controlled to obtain extremely fine, sharp and slender needles, crucial for minimizing tissue damage and improving chronic stability of implanted probes. 4- Any desired distribution of electrodes with customizable length, diameter and pitch across the array can be obtained to realize near-ideal application-specific neural probes.

Potential capabilities of this work are investigated. These include integration of optical waveguides and chemical sensors and drug delivery channels to create sophisticated multi-modal multi-channel probes for electrophysiological studies of brain at the cellular levels. Limitations of developed DRIE, bonding, and LPCVD processes and tissue volume displacement by high-density arrays are discussed and a number of solutions are proposed. These results suggest maximum electrode length of ~2.5 mm and 20 µm thick electrodes. A maximum density of ~225 electrodes/mm^2 for 10 µm thick electrodes is suggested for chronic applications.

Chapter 1: Introduction

1.1 Brain Organization and Function

Being the size of two clenched fists and weighing about three pounds, the human brain has around one hundred billion nerve cells (neurons) connected by hundred trillion connections (synapses) which are heterogeneously distributed throughout the brain making it "the most complex object in the known universe" as described by the eminent neuroscientist, Christof Koch [1-2]. Neurons, the primary components of the nervous system, are long cells with dendrites on one end and axon terminals on the other. Dendrites of one neuron are connected to the axon terminals of other neurons forming an extremely complex network of interconnected neurons that communicate with each other via electrical events called "action potentials" and chemical neurotransmitters. A neuron transmits an electrical action potential signal through its axon which causes the release of a chemical neurotransmitter at the synaptic junction. The neurotransmitter travels across the synaptic junction to be received by the receiving neuron's dendrite. The sum total of dendritic inputs determines whether the target neuron will fire an action potential [3]. Figure 1.1 illustrates a simplified depiction of brain neural network, structure of a neuron and neuronal communication mechanism as briefly described above.

Understanding the brain functions and decoding its underlying neuronal circuits relies on realizing why a neuron fires an action potential and how it propagates in the brain neural network which makes it a challenging problem considering the massive number of neurons and their extremely

dense and complex interconnected network [6-8]. Therefore, accurate mapping of neuronal circuits requires tools that can track neural signals at various spatial scales from single neuron to clusters of neurons, and interactions between various brain regions [9] with sufficient temporal resolution. In other words, neuroscience studies need a large-scale high spatiotemporal resolution probing device. Neuroscience studies can be generally categorized to systems neuroscience and clinical neuroscience. Systems neuroscience studies brain structure and function by exploring neural pathways, neural circuits, and larger brain networks as well as high-level mental functions such as memory, consciousness, language, etc. Clinical neuroscience is focused on the scientific study of fundamental mechanisms explaining the brain and central nervous system diseases and disorders with a goal of developing diagnostic and therapeutic tools and techniques. Neuroscience community has used various techniques such as optical [10], magnetic [11,12], chemical [13] and electrical [14-17] for scientific and clinical applications. Considering the spatiotemporal resolution of these techniques, implantable electrophysiological recording and stimulation neural probes are a promising tool to decipher the brain neural circuits [22].
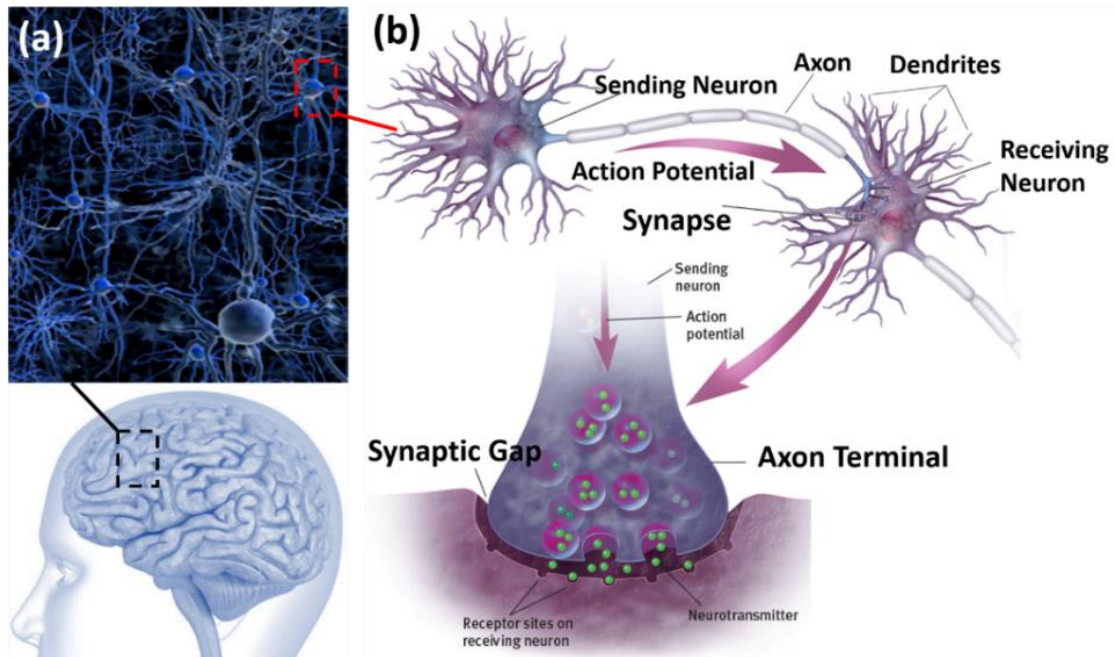
Figure 1.1: (a) Conceptual illustration of the human brain complex neural network. [http://www.me.gatech.edu/featured_robotsrecordbrainactivity] (b) Neural electrochemical communication via electrical action potential signal and chemical neurotransmitter at the synaptic junction (Image from [5]).

1.2 Neural Interfaces: Electrophysiological Recording

A neural interface is a bidirectional transducer used to communicate with neurons in the central nervous system (CNS) or nerves in the peripheral nervous system (PNS). This communication is established through the interface site which can be realized by electrodes, waveguides and fluidic ports for electrical, optical and chemical recording and stimulation, respectively. As mentioned before, considering the spatiotemporal resolution of available techniques, electrophysiological recording and stimulation neural probes are a promising tool to decipher the brain neural circuits [22]. Electrophysiological neural interface technologies are widely used to study the brain by mapping neural circuits. In this technique, brain electrical signals are recorded by electrodes placed in various locations. In electroencephalography (EEG), the electrodes are placed on the scalp, recording a spatiotemporally smoothed version of the brain local field potentials (LFPs). The soft

3

and hard tissues between the signal source and the recording electrode distort and attenuate the signal and therefore, individual neuron activity cannot be distinguished [15]. To improve the spatial resolution of the recording and reduce the distortion and attenuation caused by the skull and intermediate tissue, electrocorticography (ECoG) employs subdural electrodes to record neural signals directly from the surface of the cerebral cortex [15]. To further improve the recording spatiotemporal resolution and enhance the signal quality, implantable brain-penetrating electrodes are used to directly record from an individual neuron. This provides a tradeoff between the recording spatiotemporal resolution, fidelity and invasiveness. Implantable electrodes are a promising approach for decoding brain neural circuits, as MEMS and microfabrication technologies can be utilized to enable micro-electrode arrays (MEAs) obtain large-scale high spatiotemporal recording and stimulation of neurons with reduced invasiveness.

The focus of this thesis is on the design and development of user-definable scalable 3D high-density high-count micro-electrode arrays for extracellular recording to understand the brain neural circuits and for potential neural prosthesis applications

1.3 Micro-Electrode Arrays

One of the earliest neural action potential recording using a micro-electrode array was demonstrated in 1939 by Hodgkin and Huxley [23]. Later in 1950s, metal microwires were used to record neural extracellular electrical signals. These electrodes were metal wires that were insulated except at the recording site at the tip of the wire [25]. To increase the number of electrodes, wire bundles were made using manual assembly [26]. This type of micro-electrodes can be manufactured easily at low cost, however it suffers from lack of accuracy, repeatability, limited electrode density and count due to manual assembly. To address these issues, Wise and

Angell utilized thin-film and microfabrication technologies in 1970s and introduced a new generation of neural probes known as silicon-based neural micro-probes [17,24]. Later in 1980s, Wise and Najafi at the University of Michigan continued working on developing silicon micro-probes which led to the famous "Michigan Probe" [27-32]. Figure 1.2 shows the silicon-based micro-probes developed by Wise and Najafi. These probes have a planar design with multiple recording sites patterned across the length of the probe, the shape and thickness of the probe shank was defined using micromachining techniques.

In 1991, another type of silicon-based probe was developed and introduced at the University of Utah. As shown in Figure 1.3, the Utah Electrode Array (UEA) has a three-dimensional out-of-plane design which is manufactured by creating deep trenches in thick silicon substrates to form silicon pillars followed by chemical etching to from an array of micro-needles. Micro-needles are insulated by an insulation layer except at the tips which are coated with metal to form the recording site [33-36].

Wise, 1970   **Najafi, 1985**
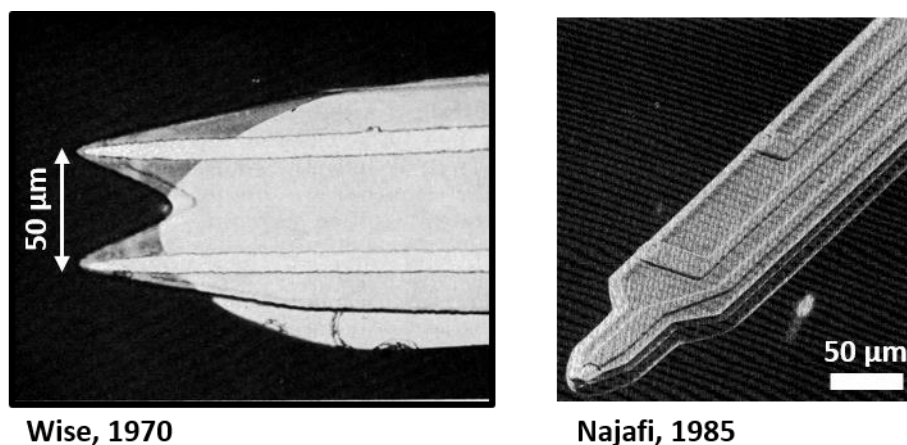
Figure 1.2: One of the earliest planar silicon-based microfabricated neural probes developed by K. D. Wise in 1970 with two recording sites [17] (left) and developed at the University of Michigan by K. Najafi in 1985 with 4 recording sites [27] (right).
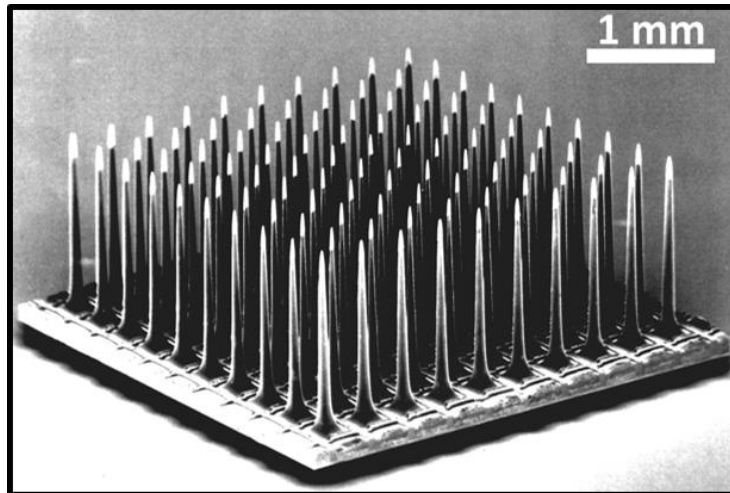
Utah Electrode Array, 1991

Figure 1.3: Utah Electrode Array (UEA) developed at the University of Utah in 1991. UEA has a 3D out-of-plane structure with 100 recording sites at the tip of each micro-needle [37].

Many types of MEAs with various designs, materials, electrode density and electrode count have since been developed using MEMS and microfabrication technologies. Considering the focus of this thesis, we will mainly review the high-density high-count electrode arrays in the next section.

1.4 Current State of Neural Micro-Electrode Arrays Technology

Microelectrodes have been widely used to study the nervous system by recording the electrochemically generated extracellular potentials by a single neuron or a group of neurons. This approach has facilitated understanding of a single neuron operation and about the functions of some neural structures. However, it is not an efficient way to decode the underlying neural circuits which is crucial for mapping the brain and understanding how the nervous system works. This shortcoming mainly arises from the fact that conventional microelectrodes only record from a single point in tissue at a time. Better understanding of neural circuit is obtained by simultaneous

recording from and/or stimulating of higher number of neurons with higher resolution. Therefore, multi-site arrays of electrodes can play a significant role in neuroscience and medical fields.

1.4.1 Electrode Count

The ever-increasing need to map larger collections of neurons has pushed the scientific and engineering community to develop new technologies and designs capable of allowing this, but with limited success and progress. As highlighted by Stevenson & Kording [38], the number of simultaneously recorded neurons has approximately doubled only every 7 years since the 1950's. The number of available sites in neural probes for simultaneous recording has been doubled almost at the same rate since 1930's, as shown in Figure 1.4. This data clearly demonstrates that our understanding of neural circuits and structures has been limited and contained by the lack of suitable multi-channel probes. This limitation is driven by the types of fabrication technologies and available deigns and materials for making such probes. The need to increase the number of sites is motivated by the need for accurately mapping the brain circuits, which will be improved by increasing the number of simultaneously recorded neurons in various parts of the brain. Moreover, high-density electrode arrays are required to obtain higher spatiotemporal resolution and better understanding of the brain network functionalities.

Using no more than a few hundred small electrodes in the brain, people with paralysis have been able to control prosthetic arms for things like self-feeding and computer control [39, 40]. Reliable interfacing with the nervous system may be able to treat an even wider range of medical conditions, but because signals are mixed at the level of single cells, one must be able to access thousands or millions of individual neurons or nerve fibers to record from or control the system. Some efforts are being made toward arrays with tens of thousands of electrodes, but these have fundamental

challenges. Systems with penetrating electrodes are limited in number of electrodes and are difficult to properly package and integrate. Systems using surface electrodes have poor signal specificity. Drawing on decades of work on truly integrated neural microsystems at the University of Michigan, we have developed a technology capable of manufacturing high-density electrode arrays scalable to millions of electrodes with high spatiotemporal resolution. This technology is capable of making extremely sharp and small electrodes, the size of capillaries that fit through the interstitial spaces between cells, with minimal damage. In addition, this technology enables future integration of closely-packed electrical, optical and chemical reading/stimulating electrodes providing neuroscientists great opportunities in studying neural interactions under various circumstances.
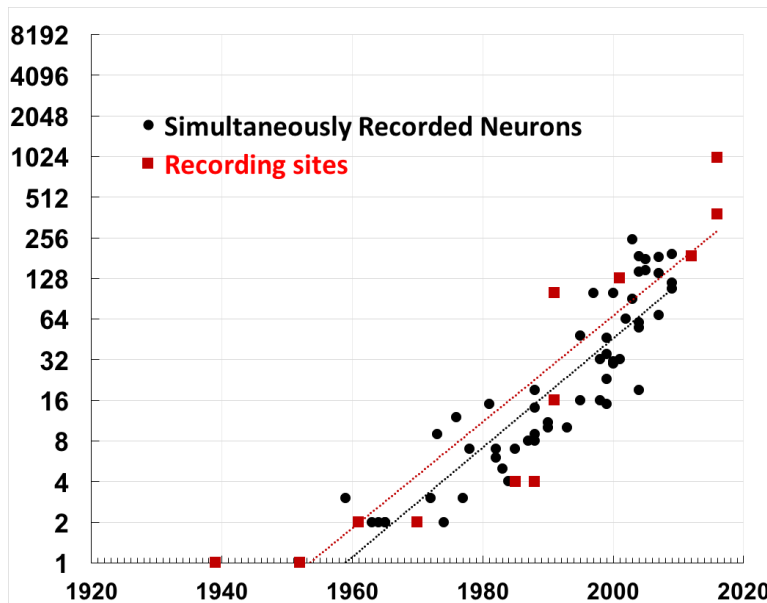
Figure 1.4: Simultaneously recorded neurons and number of recording sites available for simultaneous recording in a neural array over the past few decades (adapted from Stevenson & Kording [38]). The number of simultaneously recorded neurons has doubled approximately every 7 years since 1950's, and the number of recording sites in a probe array available for simultaneous recording has double approximately at the same rate.

1.4.2 Electrode Array Structural Design and Spatial Coverage

Traditionally, sites on a multi-site neural probe can be arranged in a number of ways, referred to as linear (1D or 1.5D), planar or areal (2D), and volume (3D), as shown in Figure 1.5. Not all of these different arrangements can be easily fabricated. Linear 1D probes provide a series of individual sites along the length of a shank. This simple structure has indeed been extremely useful for many years because it has allowed researchers to use these penetrating depth probes to study neural circuits in the cortex by allowing access to different neural regions. One of the most famous examples of linear 1D arrays is the Michigan probe. These linear 1D arrays are still extremely useful and utilized widely by the neuroscience community. One of the most advanced 1.5D probes (i.e., probes with many groups of a few sites distributed primarily along the probe shank) is reported in [21] and has ~966 sites along a 10mm long probe. 2D arrays consist of many sites distributed on multiple probe shanks to record from neurons along an imaginary plane formed by the sites. Many penetrating probe technologies offer multiple shanks to house these neurons. For example, reference [41] reports 1000 electrodes on five parallel shanks [41]. In such 2D probes, the recording plane is primarily perpendicular to the surface of the cortex (i.e., the recording plane is the same as the plane formed by the probe shanks). 2D probes can alternatively be formed by an array of electrodes whose tips form the recording sites, which form a recording plane. In this case, the recording plane is primarily parallel to the cortical surface, allowing recording from a single neural layer. The most well-known, and probably most widely-used, probe of this kind is the Utah Electrode Array (UEA) [19] (shown in Figure 1.3), which is fabricated using planar microfabrication from silicon. 2D arrays have also been demonstrated with significant improved capabilities and with many more sites by bundling insulated microwires or fibers [42,43], or by assembling carbon fibers [44-47], each of which forms a recording site at the tip. Injectable macro-

9

porous networks or recording sites formed on extremely thin and flexible layers of polymers have also been reported by [48-50]. These recording electrodes are formed in a 2D fashion on a polymer substrate, which is then rolled up and injected through a delivery needle. The rolled film opens up once in tissue and ostensibly forms a 2.5D arrays of recording sites. The location and exact distribution and shape of location of the sites is obviously not controllable. The Utah probe, like the microwire or carbon bundles, is 3D in structure but primarily 2D in its recording ability. The slanted Utah array [51] allows recording from multiple neural layers with its recording plane angled to the cortical surface, and is referred to as a 2.5D probe. Most of these 1D and 2D probes exhibit excellent in-depth spatial resolution, however their poor areal coverage due to their large shank size or large shank-shank separation limits their use in applications which require large-scale recording within a specific depth of brain. In this case, probes with wider shanks or multiple parallel probes are needed to cover a larger area which both will result in more tissue damage and reduced chronic stability. Out-of-plane electrode arrays can potentially have sufficient planar (areal) coverage, however they have a poor depth coverage. These shortcomings, in terms of latitudinal and longitudinal spatial resolution, have hindered true three-dimensional neural studies with high spatial resolution.
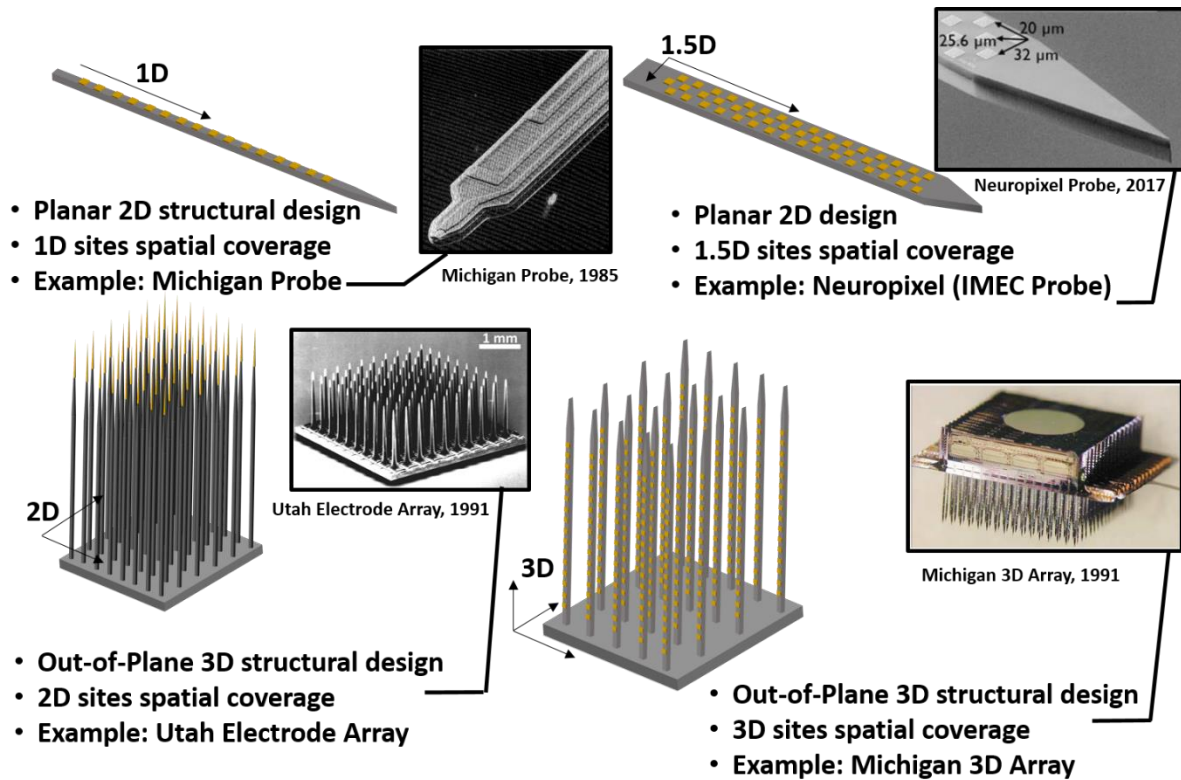
Figure 1.5: Electrode arrays structural design and spatial coverage.

3D recording arrays should be capable of recording from neurons distributed in a volume of tissue. Multiple sites are distributed along the length of several shanks, which are themselves distributed along an area of tissue. The distribution and layout of the shanks and the sites located along their length defines the volume from which recordings can be obtained. The Michigan group demonstrated one of the earliest 3D probes of this kind for both recording and stimulation [52-54]. The 3D system consisted of 2D multi-shank silicon probes fabricated using planar microfabrication techniques and then assembled onto a platform with precisely arranged features to accommodate and align the 2D probes into the final 3D structure. Rios at Caltech [55] has also recently demonstrated a large-count 3D probe by stacking several individual planar multi-shank and multi-site silicon probes, instead of assembling them through a platform as the Michigan group

did. The Michigan system also included electronics on individual probes or on the supporting platform for signal amplification and multiplexing to enable recording from all sites simultaneously. These two systems separated in time by almost 20 years represent true 3D recording probes. The structure of both of these probes is also similar to the UEA, that is the probes consist of many electrodes (shanks), with the difference being that the Michigan/Caltech electrodes can each support a linear array of recording sites, whereas the Utah electrodes could each support only one recording site at the tip of each electrode. Table I summarizes the comparison of recently reported high-density 2D and 3D neural electrode arrays. Several extensive review papers have been published by researchers that provide extensive review of the state-of-the-art probe technologies. One of the more recent papers is by Seymour which provides more detailed description of some of the systems highlighted here [56].
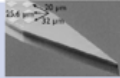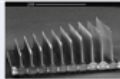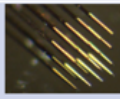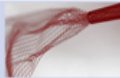
Electrode Array	Array Image	Structural Design	Spatial Coverage	Site Location C = Controlled NC=Not-Controlled	Number of Recording Sites	N_{Sh}= Number of Shanks N_S = Sites per Shank	Spatial Resolution in Depth, microns	Planar Spatial Resolution	Electrode Density Sites/mm2	Shank Dimension
Neuropixel [21]		2D	1.5D	C	966	N_{Sh}=1 N_S=966	20	NA	1380 Sites/mm^2	L=10mm W=70µm T=20µm
Slanted UEA [51]		3D	2.5D	C	100	N_{Sh}=100 N_S=1	NA	> 200µm	25 Sites/mm^2	L= 300-800 µm Ø = 100 µm
Stacked [55]		3D	3D	C	1024	N_{Sh}=16 N_S=64	12-65	250-1000 µm	1706 Sites/ mm^3	L= 1mm W= 65µm T = 21µm
Bundle [42]		3D	2D	NC	100	N_{Sh}=100 N_S=1	NA	1 mm	1 Site/mm^2	L = 0.3-1 mm Ø=30-50µm
Injectable Mesh [50]		3D	2.5D	NC	16/32	NA	250	50 µm	80 Sites/mm^2	L= 6.5mm W = 1mm T < 1
Carbon Fibers [47]		3D	2.5D	C	16	N_{Sh}=16 N_S=1	NA	150um	~44 Sites/mm^2	L=0.5-5 mm Ø = 8.4 µm

Table 1: Comparison of the state of the art high-density/high-count 2D and 3D neural microelectrode arrays.

1.4.3 High-Density High-Count Electrode Arrays Strengths and Shortcomings

Table 1 summarizes the state-of-the-art high-density high-count electrode arrays and compares their features and specifications from various aspects. In this section, strengths and shortcomings of each of these probes will be discussed.

The Neuropixel probe has one of the highest number of available recording sites and site density, however its spatial coverage is 1.5D, therefore, in order to obtain 3D spatial coverage across various brain regions, multiple probes need to be implanted which increases tissue damage and adds to the complexity of the system. The Slanted UEA is a commercially available probe and one of the most widely used probes by the neuroscience community (it is the only electrode array approved by FDA for human studies), however the UEA has limited electrode count, density and shank length. Furthermore, its large electrode shank size causes tissue damage which degrades the chronic stability of recording. The stacked probe developed by Rios et al [55] has a 3D spatial coverage with high electrode count, however it has a low planar spatial resolution. Bundle arrays have a relatively simple manufacturing process and can potentially offer large electrode count and high site density but they suffer from lack of controllability over site location as electrodes splay out during insertion in tissue. The injectable mesh developed by Lieber group at Harvard [48-50] has small cross-sectional dimensions which is critical for recording stability, however it has limited electrode count and density. The Carbon fiber array has demonstrated long chronic stability [57] due to fiber's small cross-sectional size [58-60]; however, it is made using manual assembly which is labor-intensive and is prone to accuracy and repeatability issues and electrode count and density cannot be scaled easily.

Although the above-mentioned probes, and others currently under development through several federally-funded programs like the NIH BARIN initiative, have advanced the state of the art in probe technology in terms of electrode count and structure, there still is significant room for improvement and advancement. For many applications, a three-dimensional, high spatial resolution neural recording and stimulation probe array is needed. One such application is in mapping of the hippocampus with a seahorse shape (human brain) or ram's horn shape (rat brain) with extremely dense neuron cells and an arbitrary 3D shape. For decades, neuroscientists have been deprived of a true 3D array with sufficient density and number of recording sites to simultaneously access large number of dense neurons in an arbitrary volume due to technological barriers.

1.5 Research Objectives and Thesis Contributions

The main goal of this research is to develop a new class of extremely dense, high-count, and versatile electrode arrays for interfacing with neural structures. Such electrode arrays can provide researchers with the ability to record from many thousands of neurons and to also potentially reduce damage to tissue due to their small size. The developed fabrication technology and new device structure will allow the fabrication of electrode substrates consisting of a large array of sharp, long, and narrow electrodes, each of which can interface with the surrounding tissue in the vicinity of its tip region. Each electrode can support one site for interfacing with tissue, and many electrodes can be densely packed (with a spacing of $>10\mu m$) since each electrode is extremely small. This technology will also allow the user to design a multi-shank/electrode array with any number of shanks placed in any arbitrary fashion on a substrate with any arbitrary shape. In addition, the technology developed in this work will enable integration of optical waveguides and microfluidic channels along with electrical recording/stimulation.

The work in this thesis makes the following contributions:

- Design and development of a fabrication technology for producing customizable three-dimensional out-of-plane high-density high-aspect-ratio high-electrode-count electrode arrays for neural recording and capable of manufacturing scalable (thousands and eventually millions of electrodes) arrays of extremely dense (up to 2500 electrodes/mm^2), sharp and slender electrodes. This technology enables fabrication of customized application-specific arrays of electrodes with various side-by-side shank length (tens of micrometers to several millimeters), diameter (as small as 10 µm), spacing (as close as 10 µm), tip shape and sharpness (submicron size with small opening angle) and arbitrary distribution across the array. These are achieved by developing a number of techniques including:

  - A custom-developed DRIE process to make deep high aspect-ratio thru-wafer holes with controlled sidewall slope,

  - A method of extending the thru-wafer holes depth by aligning and then fusion bonding multiple silicon substrates already having holes etched in them,

  - A process for conformal refilling of ultra-deep (mm-long) ultra-high aspect-ratio holes with dielectric and conductive films,

  - Methods of forming the recording sites using self-aligned mask-less metallization processes.

- Design and fabrication of millimeter-long, narrow, sharp (submicron tip size), high-density high-count silicon electrode arrays using the developed technologies. Arrays of electrodes with various side-by-side length, density, cross-sectional size and distribution is fabricated to demonstrate the technology capabilities in producing user-defined 3D electrode arrays.

- The capabilities and limitations of the developed technologies is studied through theoretical calculations, FEM simulations and experimental data. These includes:
  - Investigation of the maximum electrode length for successful penetration through pia mater and the underlying tissue,
  - Capabilities and limitations of the developed DRIE process in obtaining ultra-deep ultra-high aspect-ratio thru-wafer holes with controlled sidewall slopes,
  - Limitations of the ultra-deep ultra-high aspect-ratio holes refilling process to predict the upper limits of the holes aspect-ratio that can be refilled using the LPCVD process,
  - Capabilities and limitations of the wafer bonding technique is studied and a number of solutions are proposed to mitigate the bonding process challenges to increase the maximum length of the electrodes.

- Verification of the developed SEA array functionalities by performing acute *in vivo* local field potential (LFP) recordings in a rat barrel field cortex. The array was able to seamlessly penetrate the pia mater and tissue with no tissue dimpling or electrode buckling thanks to the sharp tip. Acute histology results showed successful penetration through the white mater with no electrode bending or deviation.

- Development of a fabrication technology that enables realization of integrated multi-modal probes. This technology is capable of integrating electrodes with electrophysiological, optical and chemical recording and stimulation modalities.

In summary, the ultimate contribution of this research is the development of a new technology to manufacture a user-definable 3D electrode array with electrode-count and volumetric spatial resolution well beyond the state-of-the-art.

1.6 Organization of the Thesis

Chapter 1 includes the motivation of this thesis, background and current status of Micro-Electrode Arrays (MEAs) technology, research objectives and contributions of this thesis. Chapter 2 introduces a near-ideal neural probe features and presents a qualitative and quantitative design approach to obtain an electrode array that provides the features of a near-ideal probe. Chapter 3 describes the fabrication technology used to produce a silicon-based penetrating three-dimensional high-density high-count electrode array that is capable of realizing a near-ideal electrode array. Chapter 4 presents the experimental results including fabrication results, characterization data and acute *in vivo* studies results. Chapter 5 provides details about unique features, potential functionalities and limitations of the neural electrode array technology developed in this thesis. Chapter 6 concludes the work and proposes future steps in this research.

Chapter 2: Design of a Near-Ideal Implantable Neural Electrode Array

2.1 Near-Ideal Implantable Neural Probe Features

Despite many research activities, we are still some ways from building an "ideal" probe. In fact, the "ideal" probe for mapping the activities of individual neurons and neural circuits might not be in reach for many more decades because the ideal probe needs to record from many neurons through a 3D volume of tissue, and be able to achieve this with no damage. However, we can come close to this ideal probe, and possibly produce a "near-ideal" probe with features that help overcome the shortcomings of existing probes.

What are these desirable physical features for a 'near-ideal" probe?

Figure 2.1 conceptually depicts this near-ideal probe for neuroscience and clinical applications, including hippocampus mapping. Many applications require a probe with the following features:

1) Customizable user-defined design:

– Electrode count and distribution: control over electrode/shank count and distribution within the volume being accessed;

– Electrode shank length: variable side-by-side shank length (L) to cover the irregular shape of various brain regions and minimize tissue damage to regions lying above and within it;

18

– Electrode density (spatial resolution): high spatial resolution in any arbitrary plane (P_1) and in depth (P_2)

2) Insertion and tissue damage:

– Tip shape and sharpness: a sharp and well-defined tip that allows easy initial insertion into the top tissue (pia), and further penetration into the underlying tissue (cortical mater);

– a tapered cross section approaching the tip of the shank;

– small shank cross-section to minimize tissue damage and improve chronic stability;

3) Site positioning and placement: control over the position and placement of recording/stimulation site positions following implantation;

4) Multi-modality: ability to record/stimulate electrically, and interface optically and chemically through a single shank.

In other words, we want a probe which can provide a large array of individual electrodes with controllable length, spacing, footprint, area distribution, shank and tip shape and sharpness. Further, if the probe could provide an optical and chemical interface with the tissue in addition to electrical recording/stimulation, many new results previously unattainable could be achieved.

Such a high-density array of electrodes capable of electrical, optical, and chemical interfacing with a large number of neurons in tissue could help expand our fundamental understanding of brain circuits in all of their complexity. The applications for such high-density, large-count, and multi-modal probes are many.
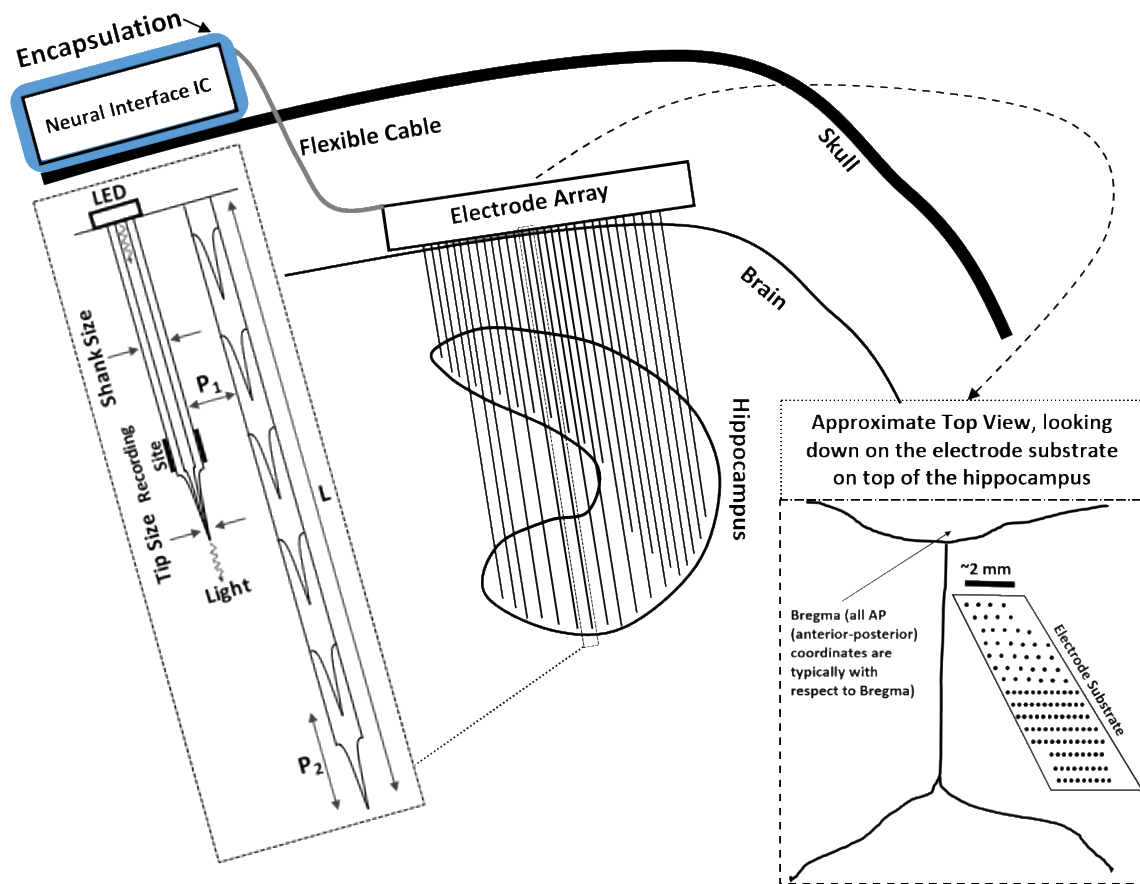
Figure 2.1: Conceptual illustration of a "near-ideal" probe for recording and manipulation of rat hippocampal neurons: Hippocampus dense neurons require an electrode array with arbitrary-shaped 3D spatial coverage with high spatial resolution in all dimensions. P_1 is the planar spatial resolution and P_2 is the in-depth spatial resolution which is obtained by varying the length (L) of side-by-side electrodes. Changing of electrode length together with the small size shank and sharp tip reduces tissue damage, thus improving chronic stability.

2.2 Design of a Near-Ideal Neural Probe

In this section, we will present a qualitative and quantitative design of a near-ideal neural electrode array based on the guidelines described in the previous section.

2.2.1 Electrode Array Structural Design and Spatial Coverage

As mentioned before, accurate mapping of complex brain neural circuits requires a neural interface that can access many neurons in different layers and across various brain regions, therefore a true 3D electrode array is preferred. An example of such application is recording and manipulation of hippocampal neurons as shown in Figure 2.1. A rat's hippocampus has a 3D irregular ram's horn shape with high neuron density, therefore, a near-ideal neural probe should be capable of accessing the neurons in 3D with high dexterity. One approach is to implant many planar electrodes individually or through stacking method as developed by [52,55]; however, this results in increased tissue displacement which negatively affects the chronic stability of the recording. Another approach is to use a 3D out-of-plane structural design similar to Utah electrode arrays. The Utah arrays only allow recording from the tip of the electrode shanks, therefore, are 2D or 2.5D (in Slanted Utah array) arrays as shown in Figure 2.2 [61]. Furthermore, they do not really utilize any of the precision microfabrication techniques, which limits how small, compact and dense it can make an electrode array. Therefore, the desired electrode array structural design is a **3D out-of-plane geometry** with small and dense electrodes to cover many neurons in any 3D volume with high spatial resolution and minimal tissue damage.
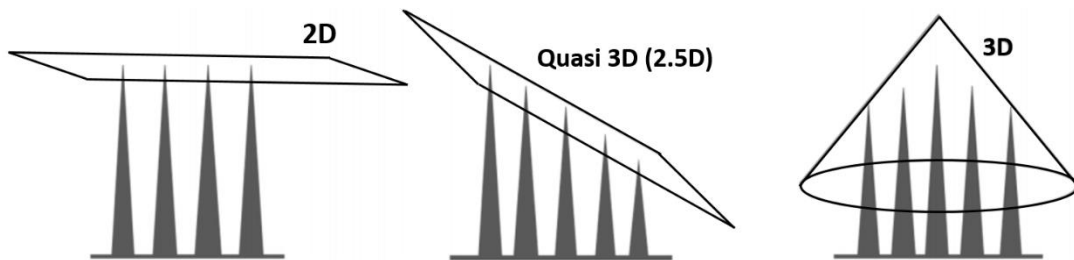
Figure 2.2: Spatial coverage of MEAs with various structural design [61]. Available out-of-plane arrays such as Utah Array (UEA and USEA) provide 2D and 2.5D spatial coverage with low resolution. An array of small electrodes with 3D and dense spatial coverage is desired.

2.2.2 Customizability of Electrode Array

The human brain consists of many different regions and layers with different surface convolution, neuron types, density and irregular-shaped tissues. Therefore, a neural electrode array design should be tailored based on the application and the region of study. As an example, the hippocampus has a seahorse or ram's horn shaped tissue positioned across different depths of the brain with densely packed neuronal structures [62-64] as shown in Figure 2.1. Thus, a near-ideal neural electrode array technology should be capable of manufacturing arrays with various electrode count, density, length, shank/tip size and distribution (layout). We will quantitatively investigate the above design parameters (length, shank/tip size, density) and their practical limitations in the following sections.

2.2.2.1 Electrode Geometry Effects on Insertion

Ideally, electrodes with minimum shank thickness (diameter) are preferred to minimize the tissue response caused by glial scarring during insertion and post-implantation. Furthermore, electrode shanks should provide sufficient mechanical robustness to survive various compression and tensile forces during the insertion and post-implantation [24]. Mechanical failures that can possibly occur during insertion of electrodes are bending/yielding, rapture, and buckling. For rapture to happen, the axial force applied to the electrode tip should exceed the ultimate compressive strength. Similarly, yield occurs when the applied stress to the electrode exceeds the maximum tensile yield strength. In the case of an electrode during insertion into the tissue, rapture and yield are unlikely to be responsible for mechanical failure as the ultimate compressive strength and the maximum tensile yield strength are much larger than the critical buckling load [65]. Rapture and yield failures mainly depend on the material properties while buckling failure is more dependent on the geometry

of the electrode. In practice, buckling can prevent electrode penetration, insertion misalignment, breakage or tissue fracturing [66]. Therefore, we focus on the critical buckling load to study the effect of electrode geometry on insertion and to present a quantitative analysis of design parameters such as shank diameter, length and tip size/shape using theoretical analyses and FEM simulations.

Critical buckling load (force) is the maximum load which a column can bear before buckling and can be calculated using Euler's column formula as shown in equation (1), where P_{cr} is the Euler's critical load, E is the elastic modulus, I is the relative area moment of inertia, L is the unsupported length of the column and K is the column effective length factor. Any load larger than the critical buckling load results in buckling failure. There are five buckling modes for a column which determine the value of K in this formula. Based on the tissue insertion experiments done by Marshall et. al [65], the buckling mode is shown to have boundary conditions of a column with one end fixed and the other end hinged, therefore, the column effective length (K) value will be 0.7.

$$P_{cr} = \frac{\pi^2 EI}{(KL)^2} \qquad\qquad (1)$$

$$I = \frac{\pi D^2}{64} \qquad\qquad (2)$$

2.2.2.2 Finite Element Model (FEM) Simulation Results

In this section we will study the effects of geometry on the insertion of electrodes in the brain pia mater and tissue using critical buckling load simulations in COMSOL Multiphysics 5.1. (COMSOL, Inc., MA, USA).

Setup

We have studied the effects of electrode geometry on tissue insertion using the linear buckling analysis in COMSOL Multiphysics. Figure 2.3 shows the 3D and 2D images of the simulated electrode geometry and materials in these studies which are chosen to represent the fabricated electrodes described in chapter 3. As shown below, the electrode geometry consists of two parts, a cylindrical base shank with length of L_1, inner radius of R_1, thickness of T, which sets the outer radius to be (R_1+T), and a top electrode part which has a conical shape with sharp tips for easier penetration into brain tissue. The conical tip part has a length of L_2, with the base inner radius of R_2, outer radius of (R_2+T) and tip radius of R_3. As mentioned in the previous section, for the buckling load analysis a fixed-hinged boundary condition is chosen, meaning that the shank base is fixed and the tip has a hinged boundary condition in the shank axial direction with no lateral displacement as illustrated in Figure 2.4. Table 2 shows the material properties used in these simulations.
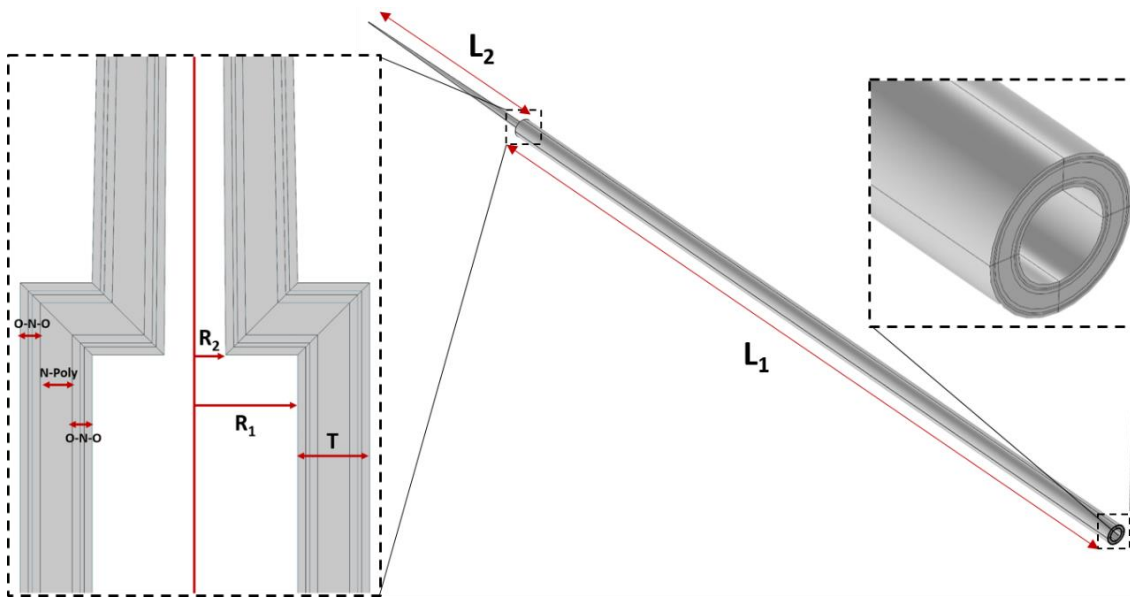
Figure 2.3: 2D and 3D structure of modeled electrode geometry and materials in COMSOL Multiphysics.
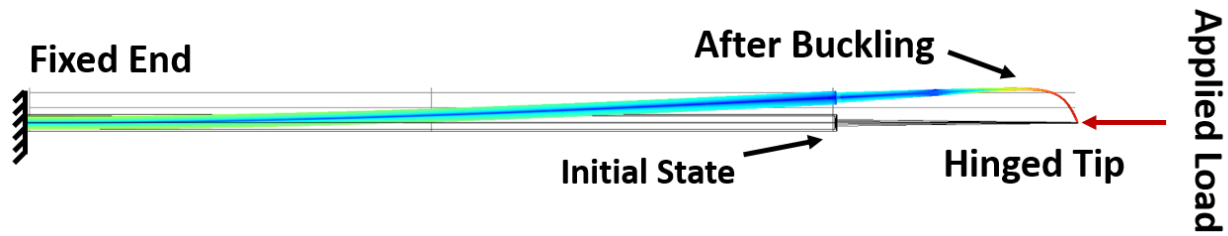
Figure 2.4: Boundary conditions of linear buckling load analysis: Electrode shank base is fixed while the electrode tip has a hinged boundary condition.

Material	Young's Modulus	Poisson Ratio	Density (kg/mm^3)
Polysilicon	160 GPa	0.22	2320
SiO$_2$	70 GPa	0.17	2200
Si$_3$N$_4$	250 GPa	0.23	3100

Table 2: Material properties used in the buckling load analysis simulations.

2.2.2.2.1 Electrode shanks cross-sectional size (diameter)

Electrodes with minimum shank diameter are preferred to minimize the tissue response caused by glial scarring during insertion and post-implantation. However, there is a tradeoff between shank diameter and critical buckling load, i.e., thinner shanks have a smaller critical buckling load which makes them more susceptible to buckling failure. In this section we use FEM simulations to study the effect of the shank diameter on the critical buckling load to determine the minimum shank diameter required for successful insertion into the pia mater and the brain tissue underneath it. In this simulation the values shown in Table 3 are used for the shank geometry.

25

Neural electrode insertion forces through the pia mater of a rat brain have been measured to be approximately 0.5 to 2 mN in different studies using various electrode geometries and materials [67-75]. Penetration forces are highly dependent on the electrode tip shape, size and sharpness, with larger tips exhibiting larger penetration forces [67-75]. Also tips with larger opening angle require higher forces for penetration [67]. The opening angle is the acute angle of the probe tip from edge to edge as shown in Figure 2.5 [75]. Probes with tip opening angles of $<20^{\circ}$ have shown easy penetration through dura without dimpling, while probes with opening angle of $>40^{\circ}$ have exhibited difficult dura penetration [75,76]. Other studies using silicon probes have shown the significance of tip opening angle on the insertion forces, as reducing the tip angle has reduced the penetration forces exponentially [73,75].
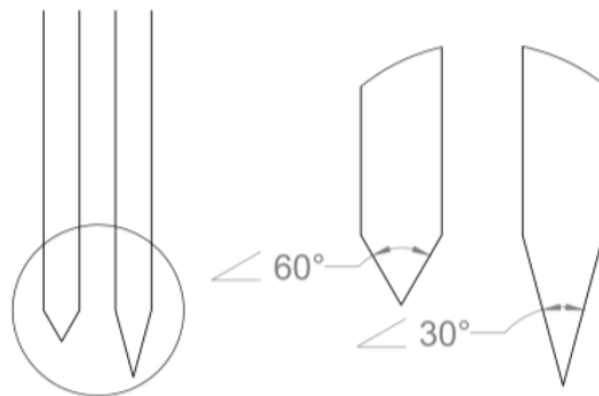
Figure 2.5: The electrode tip opening angle is defined as the acute angle of the tip from edge to edge [75]. Smaller tip opening angle results in smaller insertion force and easier penetration.

Patel et al. [65] demonstrated insertion forces of 780 µN for 6.8 µm diameter Carbon fiber electrodes with blunt tips which means the required stress for successful penetration through mater to be around 20 MPa. Najafi et al. reported the rat pia penetration stress to be between 0.04 mN/µm^2 and 0.12 mN/µm^2 for Michigan probes with a cross-sectional area of 900 µm^2 and 1200

μm^2 respectively with the tip opening angle of 60° [77]. Jensen et al. used various tapered probes with different tip opening angles and shank diameters to measure the pia penetration forces in rats. They reported penetration forces of 0.48-1.15 mN for various electrodes [67]. The closest probe used in this work to our structure was a tungsten electrode that was manually electro-sharpened with an opening angle of 4° and shank diameter of 50 μm. This probe exhibited a penetration force of ~0.62 mN [67]. The probe structures used in our simulations have an opening angle of 3° which is very close to the tungsten electrode in [67]. Although Jensen's shank diameter is much larger, the size and shape of the tip is the main determining factor for estimating penetration forces and buckling loads. Therefore, we assume the required pia penetration forces to be 0.62 mN, although we expect it to be smaller for our probe as the shank diameter is smaller. This is a very conservative but safe assumption for determining the penetration forces and critical buckling load values.

As shown in Table 3, the R_1 and R_2 values are changed in the range of 6-10 μm and 2-5 μm, respectively, and the critical buckling load is simulated for all the combinations of these values. Figure 2.6 shows the simulation results for the critical buckling load values for various combinations of R_1 and R_2 values. To ensure successful penetration, the critical buckling load should be larger than 0.62 mN. The R_1, R_2 value combinations that satisfy this criteria are marked by dashed lines in the plot. Figure 2.7 shows the simulated critical buckling load values for electrode structures with smaller R_1, R_2 values. These results (Figure 2.6 and 2.7) show that the minimum R_1, R_2 values that show critical buckling load of >0.62 mN are 5 μm and 5 μm, respectively. Figure 2.6 clearly shows that the radius of the conical tip base (R_2) has more effect than the cylindrical shank base inner radius (R_1), as changes across the y-axis of the plot is more significant than changes across the x-axis.

Cylindrical Base Length (L₁)	**1000 μm**
Conical Tip Length (L₂)	**200 μm**
Shank Thickness (T)	**4 μm**
Tip Radius (R₃)	**0.5 μm**
Base Inner Diameter (R₁)	**Swept [6-10 μm]**
Tip Base Diameter (R₂)	**Swept [2-5 μm]**

Table 3: The electrode geometry parameters used in the buckling load simulations. The effect of cylindrical base and conical tip base diameter on critical buckling load is investigated by varying the R_1 and R_2 values.
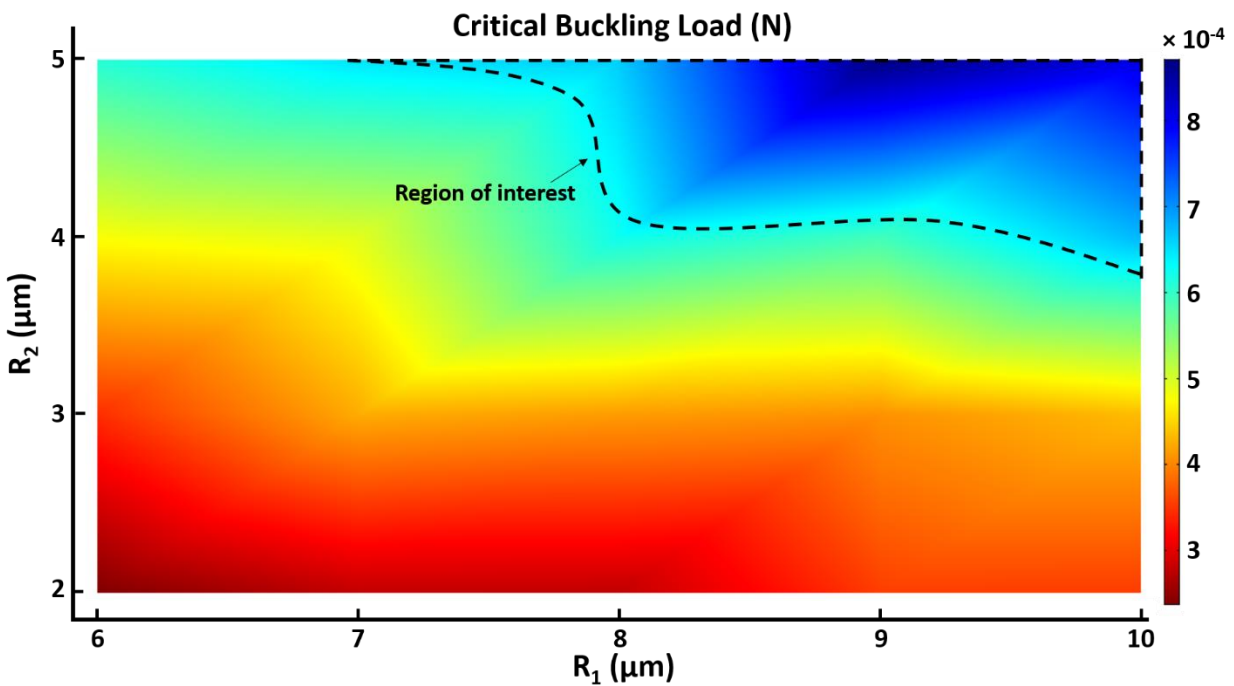
Figure 2.6: Simulation results of critical buckling load of electrodes with various R_1 and R_2 values. The marked area with dashed line represents the electrode R_1 and R_2 values that exhibit critical buckling load larger than 0.62 mN.
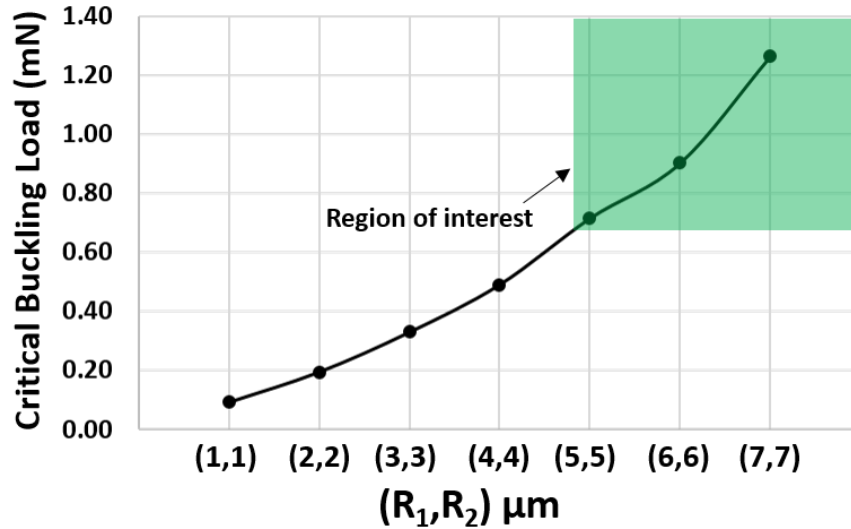
Figure 2.7: Simulation results of critical buckling load of electrodes with equal R_1 and R_2 values. The marked area in green shows the electrode R_1 and R_2 values that exhibit critical buckling load larger than 0.62 mN.

These simulation results suggest that to obtain critical buckling loads of larger than 0.62 mN to ensure successful pial penetration, R_1 and R_2 should be ≥ 5 μm.

Figure 2.8 demonstrates the effect of R_1 and R_2 values on the electrode buckling shape and von Mises stress distribution along the electrode at the critical buckling load applied to the tip of the electrode. As shown, in electrodes with smaller R_2, buckling mainly occurs at the conical part of the tip and since this part has a smaller diameter, the critical buckling load will be much smaller compared to an electrode with larger R_2. Also, the stress concentration at the tip with equal applied force (load) will be much higher in electrodes with smaller R_2 and makes it more susceptible to buckling and breakage.

As mentioned before, smaller shank cross-sectional size is desired, however, different applications require electrodes with various lengths, and there is a tradeoff between electrode length and the

29

critical buckling load. Therefore, to determine the minimum R_1 and R_2 values, we have performed linear buckling load simulations on electrodes with various lengths. These simulations suggest the smallest cross-sectional sizes to obtain electrodes up to 5 mm long that have critical buckling load of lager than 0.62 mN are $R_1 \geq 9$ µm and $R_2 \geq 5$ µm. The details of these results will be discussed in the next section.

To reduce the stress concentration factor around the stepped shank and improve the mechanical robustness, values of R_1 and R_2 are chosen closer for a smoother transition [4] as shown in Figure 2.9. Ideally, electrodes with $R_1 = R_2$ are desired, however due to fabrication technology challenges (discussed in chapter 5), R_1 has to be larger than R_2. Therefore, $R_1 = 9$ µm and $R_2 = 5$ µm are the minimum sizes to satisfy the critical buckling load conditions, technology limitations and reduced tissue displacement by minimizing the cross-sectional sizes.

2.2.2.2.2 Electrode Shank Length

The length of the electrode is another parameter that determines the shank critical buckling force, meaning that longer electrodes exhibit smaller critical buckling force. Depending on the species and the target brain region, electrodes with shank length of 0.2 mm to 100 mm are needed [75]. Using the values obtained for R_1 and R_2 in the previous section, we simulated the critical buckling force of electrodes with various L_1, L_2, R_1 and R_2 values to obtain a safe range of electrode length that ensure successful rat brain pial penetration without buckling and breakage. In this simulation the following values are chosen for the shank geometry. Figure 2.10 shows the simulation results of the critical buckling load for various combinations of L_1, L_2 and $R_1 = R_2 = 5$µm values. These results show that for electrodes with $R_1 = R_2 = 5$µm, the maximum length to obtain critical buckling load larger than 0.62 mN is very limited (<3mm) which limits the electrode array neural

applications. Figure 2.11 shows simulations results of critical buckling load of electrodes with R_1 = 7 μm, R_2 = 5 μm and various L_1 and L_2 values. As shown, the maximum length to obtain critical buckling load larger than 0.62 mN is limited to 4mm.

Figure 2.12 results show that for electrodes with cross-sectional sizes of R_1 = 9 μm, R_2 = 5 μm, the length can be increased to 6 mm and still obtain critical buckling load of $\geq$ 0.62 mN. For most neural applications, in particular, in rodent species, these lengths are sufficient. These simulation results also suggest that the best way to obtain sufficiently large critical buckling load for long electrodes is to keep the conical part length (L_2) short, as this part has the smaller thickness.
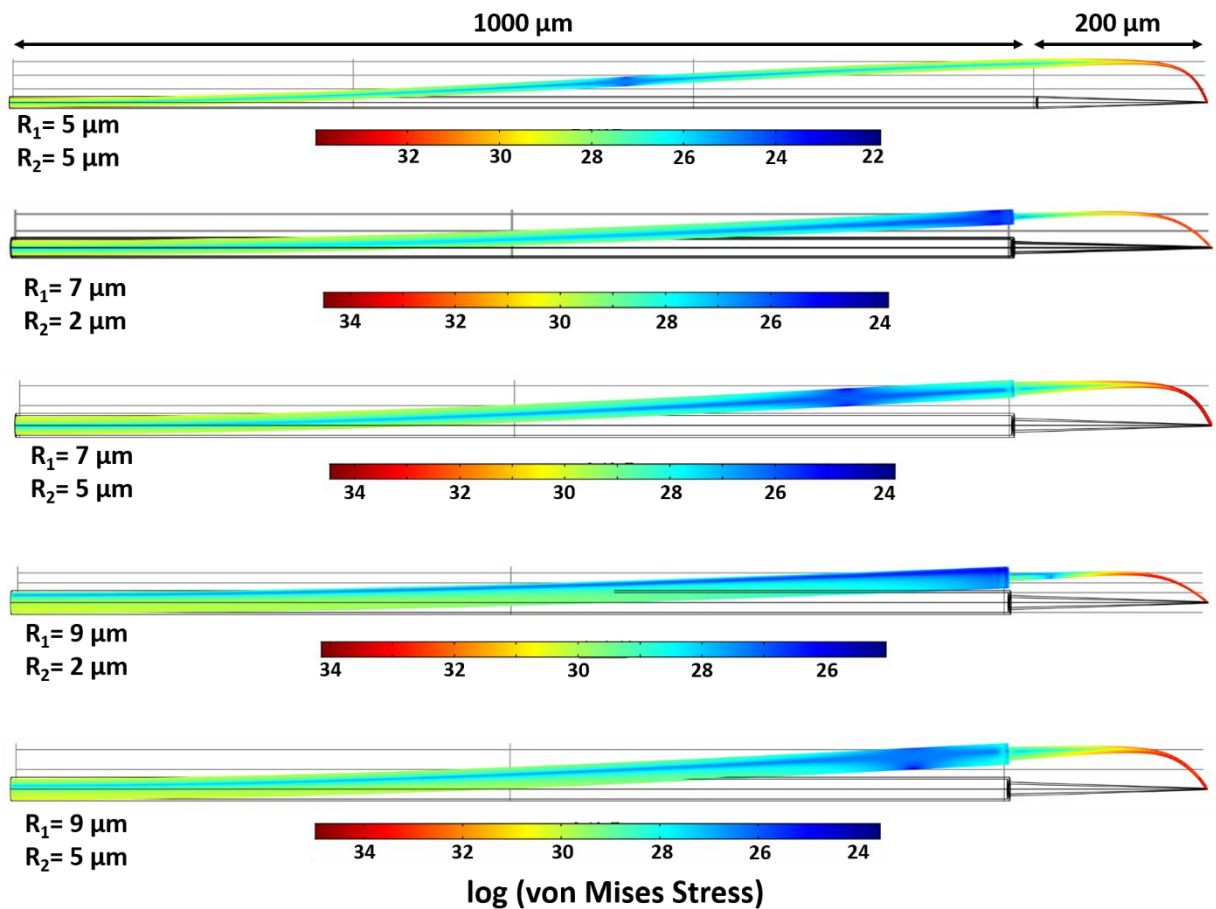
Figure 2.8: Electrodes buckling shape and von Mises stress distribution along the electrodes with various R_1 and R_2 sizes at critical buckling loads.
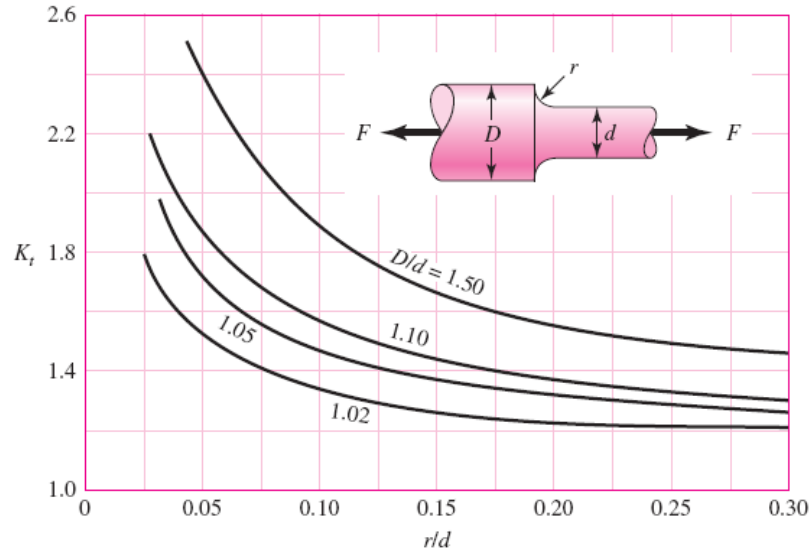
Figure 2.9: Theoretical stress concentration factor (K_t) for round shafts with shoulders with various D, d and r sizes. As shown, smoother transition at the shoulder (more beveling with larger r) reduces the stress concentration. Also, the stress concentration is reduced for shafts with smaller D/d [4].

Cylindrical Base Length (L_1)	**Swept [1-12 mm]**
Conical Tip Length (L_2)	**Swept [0.2-0.3 mm]**
Shank Thickness (T)	**4 μm**
Tip Radius (R_3)	**0.25 μm**
Base Inner Diameter (R_1)	**5, 7, 9 μm**
Tip Base Diameter (R_2)	**5 μm**

Table 4: The electrode geometry parameters used in the buckling load simulations. The effect of cylindrical base and conical tip base length (L_1 and L_2) and base inner diameter (R_1) on critical buckling load is investigated by varying the L_1, L_2 and R_1 values.
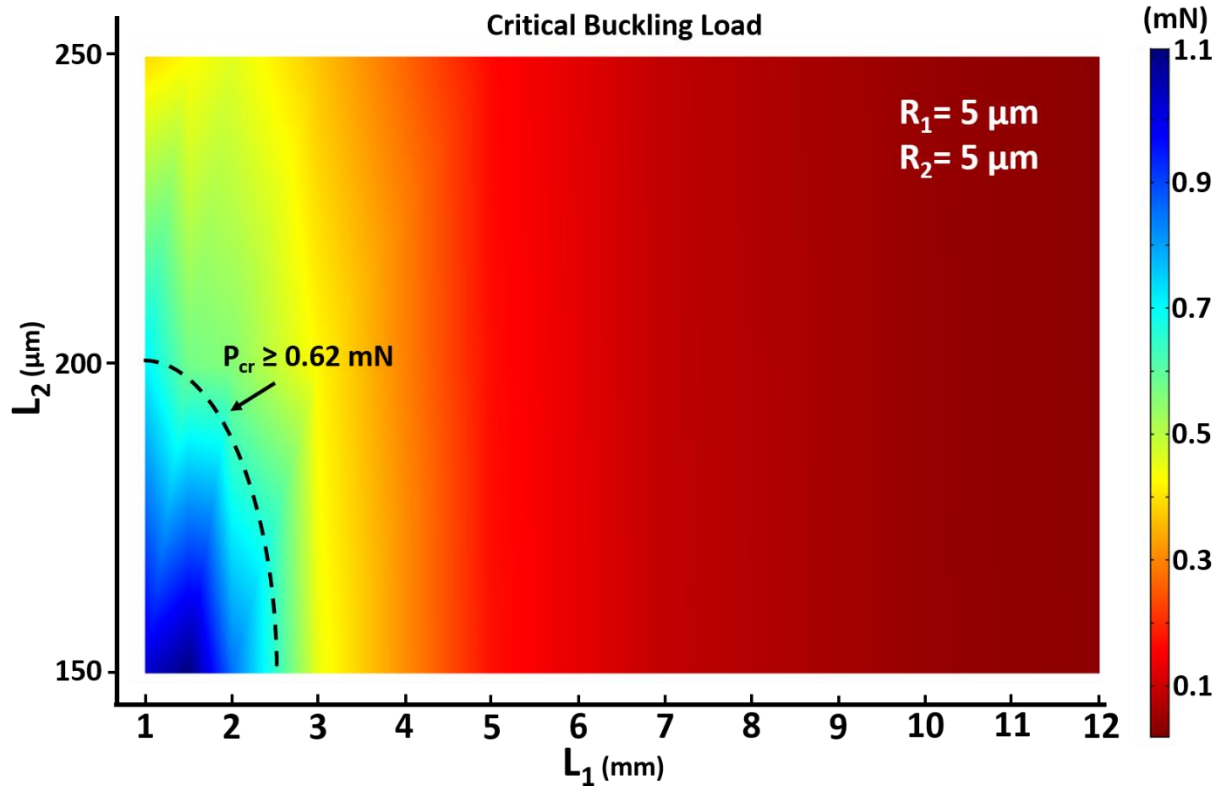
Figure 2.10: Simulation results of critical buckling load of electrodes with $R_1 = R_2 = 5$ μm and various L_1 and L_2 values. As shown, in electrodes with $R_1 = 5$ μm, the maximum length to obtain critical buckling load larger than 0.62 mN is very limited (<3mm) which limits the electrode array neural applications.

Figure 2.13 visually demonstrates the effect of L_1 on the electrode buckling shape and von Mises stress distribution along the shank. As shown, in electrodes with smaller L_1, buckling mainly occurs at the conical part since this part has a smaller diameter, while for longer electrodes, buckling occurs along the longer cylindrical part of the shank.
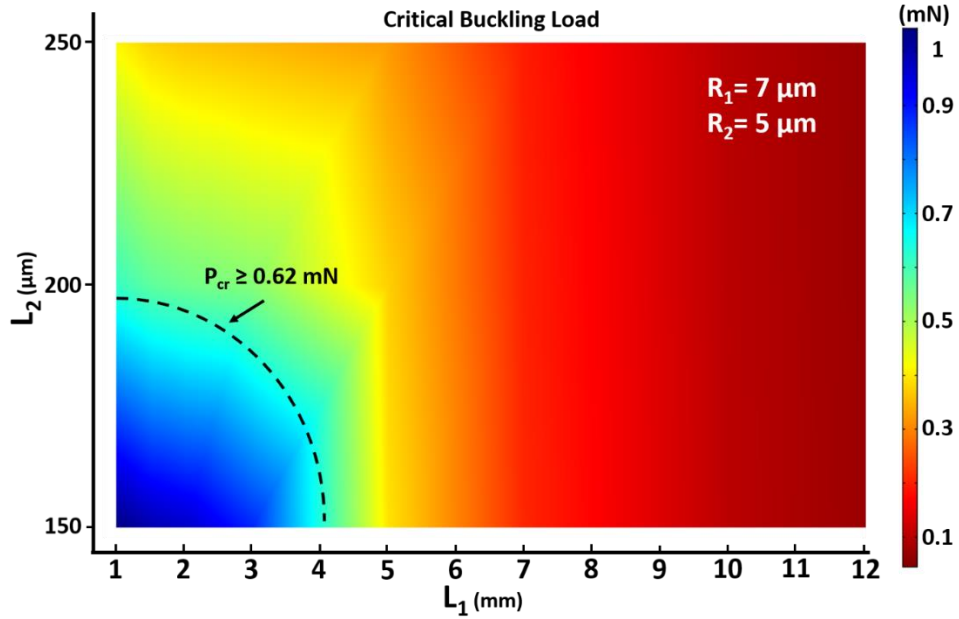
Figure 2.11: Simulation results of critical buckling load of electrodes with $R_1 = 7$ μm, $R_2 = 5$ μm and various L_1 and L_2 values. As shown, the maximum length to obtain critical buckling load larger than 0.62 mN is limited to 4mm.
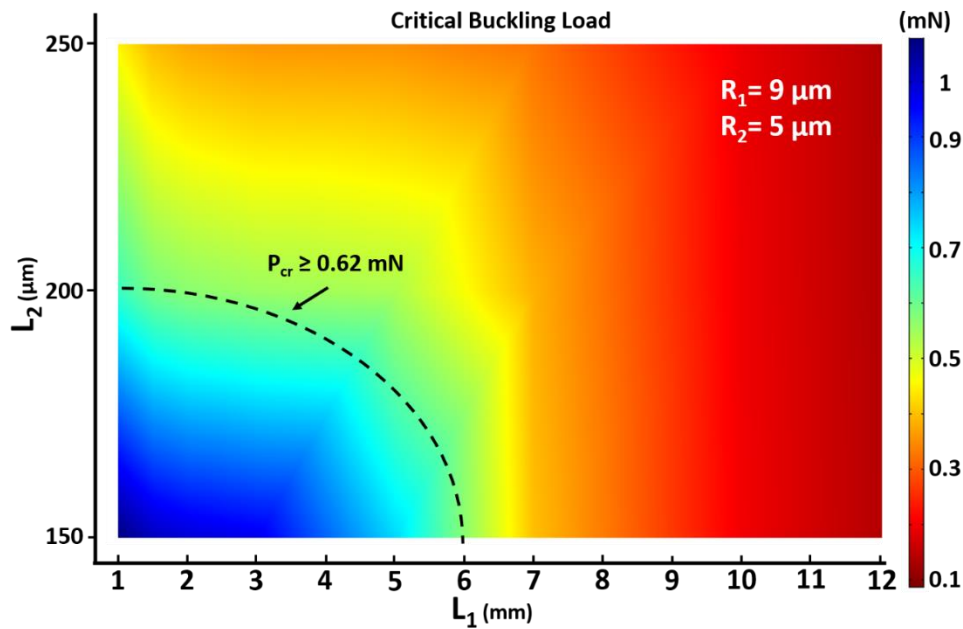
Figure 2.12: Simulation results of critical buckling load of electrodes with $R_1 = 9$ μm, $R_2 = 5$ μm and various L_1 and L_2 values. As shown, electrodes with these cross-sectional sizes and as long as 6 mm can exhibit critical buckling load of larger than0.62 mN which is sufficient for many neural applications.
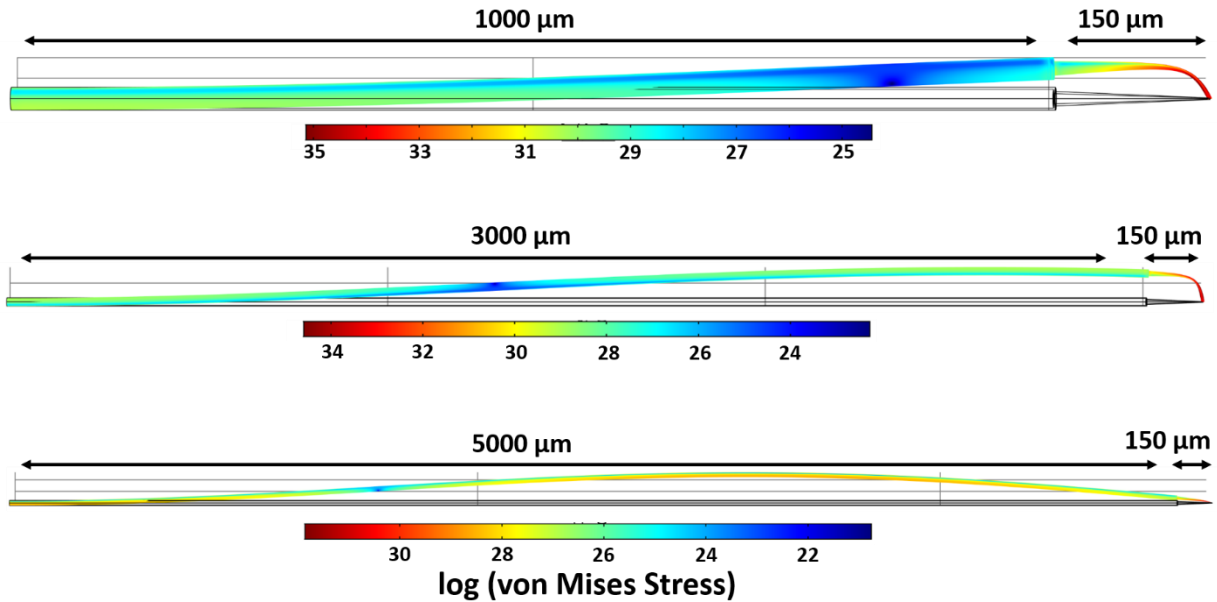
Figure 2.13: Effect of electrode length on the buckling shape and von Mises stress distribution along the shank. In shorter electrodes buckling mainly occurs along the conical part of the tip while in longer electrodes, buckling is more evident along the cylindrical part of the shank.

2.2.2.2.3 Electrode Shank Tip Diameter

Another parameter that determines the penetration force is the tip shape, sharpness and size. Blunt tips, conical tips with larger opening angles, and tips with larger diameter exhibit higher penetration forces which results in dimpling and increased tissue damage. In our design, we focus on sharp tips with various tip diameters. We have simulated the critical buckling load of electrode shanks with various length (L_1) and tip diameter ranging between 0.5μm and 4 μm as shown in Figure 2.14. These results show that electrodes with smaller tip diameters (sharper tips) have a smaller critical buckling load. This is due to the fact that the conical tip part base has a fixed diameter (R_2) and reducing the tip diameter (R_3) will reduce the diameter along the conical tip part, therefore, lower forces are sufficient to cause buckling of the conical part close to the tip as shown in Figure 2.15(A). However, it should be noted that in these simulations, in order to calculate the critical buckling load, it is assumed that the electrodes are prevented from penetrating the pia. This

35

assumption is required for critical buckling load calculations. In practice, electrodes with smaller tip size require smaller insertion force and therefore are less susceptible to buckling failure despite having smaller critical buckling load. In other words, the results shown in Fig. 2.14 should not be considered as the required penetration forces for various electrode tip sizes.

Figure 2.14 also suggests that by increasing the electrode length, the critical buckling load is mainly determined by the electrode length and therefore a decrease in critical buckling load is observed as the electrode length is increased as shown in Figure 2.15(B). In other words, in longer electrodes, buckling occurs at lower insertion forces due to buckling at the long cylindrical part of the shank while in shorter electrodes, buckling occurs at the conical tip where it has a smaller diameter and is more prone to buckling. These results suggest that to obtain critical buckling load of larger than 0.62 mN the tip size should be larger than 0.6 μm.
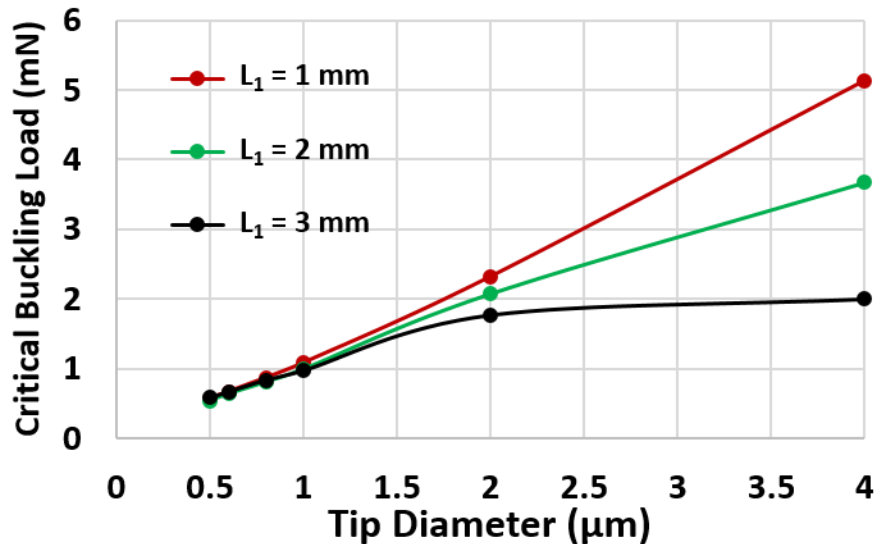
Figure 2.14: Simulated critical buckling load values for electrodes with various tip size and length. Electrodes with tip diameter ≥ 0.6 μm for various lengths exhibit sufficient critical buckling load for successful pial penetration.

Tip Diameter: 0.5 µm

A

Tip Diameter: 2 µm

Tip Diameter: 0.5 µm, Length: ~ 1.2 µm

B

Tip Diameter: 0.5 µm, Length: ~ 5.2 µm
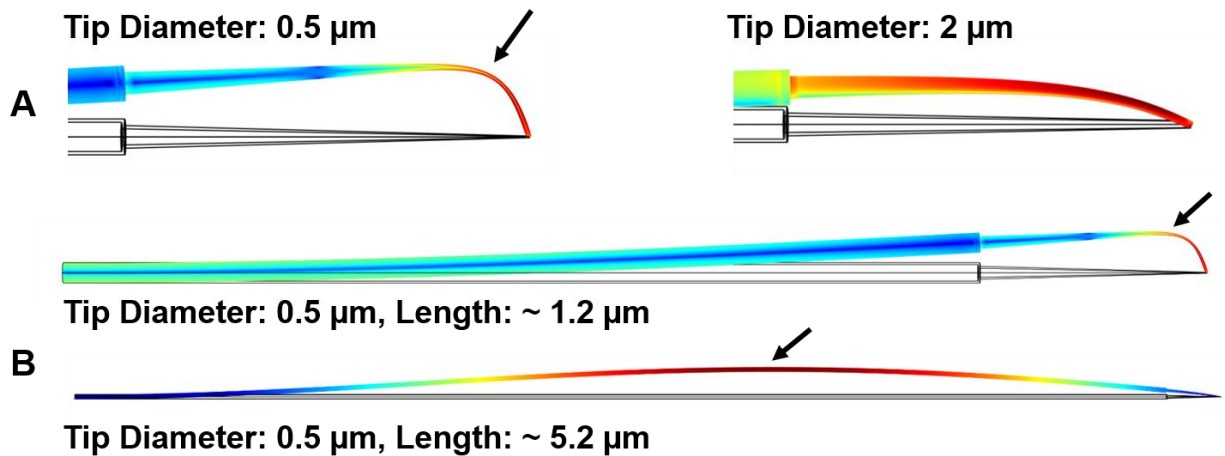
Figure 2.15: Effect of electrode tip size and length on critical buckling load: (A) Effect of tip diameter on the buckling of electrodes, as shown reducing the tip diameter results in reduced thickness of the conical tip section and therefore larger buckling close to the tip. (B) Effect of electrode length on the buckling of electrodes, in longer electrodes the buckling occurs along the long cylindrical base of the electrode whereas in short electrodes the buckling mainly occur along the conical tip section.

2.2.2.2.4 Electrode Penetration through Pia Mater Simulations

In this section we study the penetration of an electrode through the rat brain pia mater using a finite-element model. Figure 2.16 shows an axisymmetric indentation model of a layered structure developed in COMSOL 5.3a. The model consists of three components, an electrode, a thin elastic layer representing the pia mater membrane and an elastic bulk material representing the brain tissue beneath the pia. The electrode geometry parameters obtained in previous sections are used in this simulation as shown in Table 5.

Cylindrical Base Length (L₁)	1 mm
Conical Tip Length (L₂)	0.15 mm
Shank Thickness (T)	4 μm
Tip Radius (R₃)	0.3 μm
Base Inner Diameter (R₁)	9 μm
Tip Base Diameter (R₂)	5 μm

Table 5: Electrode geometry parameters used in the pia mater penetration simulations.

The pia layer 3D model is a cylinder with a thickness of 10 μm and diameter of 1 cm. Similarly the brain tissue has a cylindrical structure with height and diameter of 5 mm and 1 cm respectively. Table 6 presents the material properties used in the brain model to accurately match the rat brain structure [75, 78-81]. To examine whether the electrode can successfully penetrate through the pia layer without buckling, we applied a force at the other end of the electrode and simulated the von Mises stress distribution through the pia layer volume. The applied force is chosen to be below the electrode critical buckling force. Based on the linear buckling simulation results obtained in previous sections, the critical buckling load of the electrode used in this simulation is around 665 μN. Therefore, we applied a load much smaller than the critical buckling load (100 μN) to the electrode to prevent buckling. Figure 2.17 shows the von Mises stress distribution in the 3D model of the electrode-pia-tissue structure. These simulations show that the pia layer stress reaches as high as 120 MPa which is much larger than the required stress needed for penetration through pia (40 MPa) as reported in [67, 77, 82]. Therefore, this model predicts the designed electrode is capable of penetrating the rat pial membrane without buckling. Also, the small volumetric stress concentration is a sign of minimal dimpling and tissue stress which demonstrate the importance of tip size and sharpness.
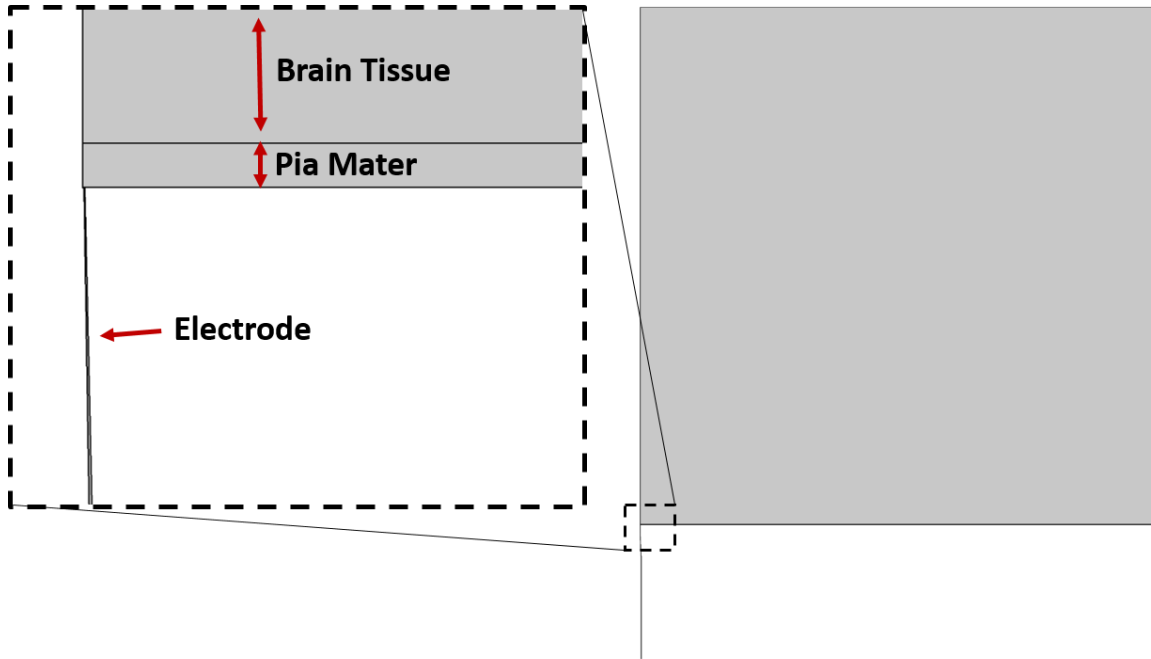
Figure 2.16: An axisymmetric model of layered structure representing a rat brain tissue, pia mater layer, and a penetrating electrode. The electrode geometry parameters and tissue properties used in the simulation are shown in Table 5 and 6 respectively.

Material	Young's Modulus	Poisson Ratio	Density (kg/mm³)
Pia Mater	15.8 MPa	0.45	1130
Brain Tissue	30 kPa	0.45	1050

Table 6: Material properties used in the brain model to accurately match the rat brain structure [75, 78-81].
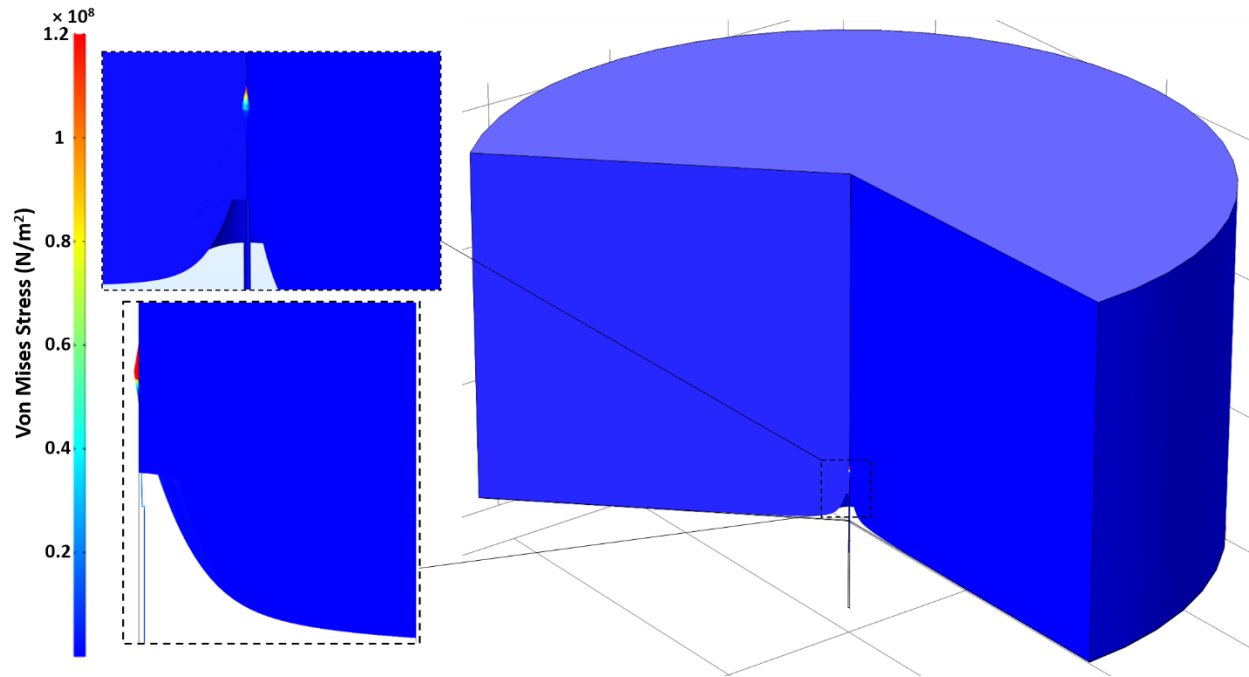
Figure 2.17: Von Mises stress distribution in the 3D model of the electrode-pia-tissue structure. By applying a 0.1 mN load the pia layer stress reaches as high as 120 MPa which is much larger than the required stress needed for penetration through pia (40 MPa). Therefore, this model predicts the designed electrode is capable of penetrating the rat pia membrane without buckling, also, the small volumetric stress concentration is a sign of minimal dimpling and tissue stress which demonstrated the importance of tip size and sharpness.

2.3 Conclusions

In this chapter, the features of a near-ideal neural interface technology are described and used as a guideline to design and develop a new electrode array technology. These features include:

- Control over electrodes length, count, distribution and density across the electrode array to obtain 3D spatial coverage.

- High spatial resolution in any arbitrary plane to obtain high-density large-scale electrode arrays.

- Small cross-sectional size with tapered shank sidewalls profile approaching an ultra-sharp tip to minimize tissue damage during and post implantation.

- Multi-modal recording and stimulation of neurons using electrophysiological, optical and chemical methods.

FEM simulations were used for analysis of electrode insertion through the rat brain pia mater using critical buckling load simulations in COMSOL Multiphysics. The simulation results suggest a minimum inner diameter of 10 µm and 14 µm for the base of the cylindrical and conical parts, respectively, and maximum length of 6 mm to ensure pial penetration without buckling. In these simulations the pial penetration force is assumed to be 0.62 mN based on the values reported in literature for other electrodes with very similar tip shape and size.. Using these results, the final electrode geometry was determined (length of 1.2 mm, base outer diameter of 22 µm with sharp submicron tips) which showed successful pia penetration with insertion forces well below the electrode critical buckling load. These electrode design parameters were used for the electrode array as discussed in the following chapters.

Chapter 3: Fabrication Technology

3.1 Introduction

As explained in the previous chapter, many different kinds of multi-channel electrodes are available today, utilizing different fabrication technologies. One can categorize these fabrication technologies into two broad classes. One utilizes assembly and manipulation of individual electrodes (such as carbon fibers or microwire bundles) to fabricate the final array structure. This approach could work well when making only a few complete systems, and where high precision is not needed in either making the individual electrodes (e.g., control of dimensions, tip shape, sharpness, etc.), or in controlling the features of the multi-electrode array (e.g., minimum distance between electrodes, distribution pattern of electrodes). Although some of these aspects could be better controlled using mechanized tools, ultimately these systems are limited to at best a few thousand electrodes, and provide limited precision and control for applications that require such precision. The second approach relies on planar microfabrication technologies, such as those used for semiconductor electronics fabrication. This approach provides excellent control over device dimensions, material properties, and pattern and shapes on a two-dimensional plane. Anything that can be fabricated on a silicon wafer, can be fabricated with precision and extreme control and freedom over layout and shape. The main drawback of this approach is that anything that needs to have a third dimension and be thicker than ~0.5mm (which is the thickness of a standard 4" diameter silicon wafer) cannot be fabricated in silicon. The Utah electrode array is the only silicon 3D array not needing assembly following fabrication. However, it does not really utilize any of

the precision microfabrication techniques, which limits how small or compact and dense it can make an electrode array.

The fabrication technology developed in this work (SEA technology) will allow us to combine the best features of both of these approaches. The SEA technology can radically increase the density and count of these electrode arrays. We have developed a technology capable of fabricating electrodes with a diameter of less than 10-20 µm near the bottom and less than 1µm at the tip, with lengths as large as several millimeters. An areal density of more than 400 electrodes/mm^2 is obtained which can be increased to densities as high as 2500 electrodes/mm^2 assuming a diameter of 10 µm and spacing of 10 µm between electrodes. Although such a dense array could displace as much as 25% of the tissue and thus not desirable in many applications, the technology is still capable of producing such an array, thus providing the user complete freedom in designing the pattern and distribution of these electrodes for a given application. The fabrication technology does not change, only the layout that the user defines on photolithographic masks used to produce the array will have to be modified. The technology is capable of producing electrodes as small as a few microns in diameter and several millimeters long.

3.2 Sea of Electrodes Array (SEA): Fabrication Technology

In this section, we will describe in detail the fabrication technology to produce silicon-based micro-electrode arrays. The SEA manufacturing process employs a scalable technology to fabricate a new generation of 3D arrays with high-density high-electrode-count neural recording electrodes made from silicon. To overcome the shortcomings and issues of previously reported arrays, a fabrication process based on refilling deep ultra-high aspect-ratio holes in a silicon substrate with deposited layers followed by etching away the support substrate to leave thousands and eventually

43

millions of electrodes, is developed. In the following sections of this chapter, first we describe the refilling-based technology to make conical micro-needle electrodes and then we present a fabrication process to obtain millimeter-long functional electrodes for neural recording.

3.2.1 Refilling Technology

Figure 3.1 shows an overview of the refilling-based fabrication technology. Details of each step are discussed in the following sub-sections. The fabrication process begins with a custom high aspect-ratio deep reactive ion etching (DRIE) of holes in a p-type (100) silicon wafer (Figure 3.1A). DRIE Aspect Ratio Dependent Etching (ARDE) effect and DRIE lag effect are utilized to obtain a tapered profile at the bottom of the holes, which is required to obtain electrodes with conical shape and sharp tips. These holes are then refilled with multiple layers of low-pressure chemical vapor deposited (LPCVD) films to form the electrode conductor and insulator layers. In the current process, we deposit the following layers in order: 1) a sacrificial polysilicon layer (which is etched away in the final structure) of a few microns in thickness to reduce the hole diameter and thus the final needle shank diameter (Figure 3.1B); 2) a composite layer consisting of LPCVD Oxide-Nitride-Oxide (ONO) to form the outer insulator of each individual electrode (Figure 3.1B); 3) a second LPCVD polysilicon layer that is highly doped to form the conductive core of the electrode (Figure 3.1C); and 4) a second LPCVD ONO inner insulator layer (Figure 3.1C). The ONO insulator layers are used for electrical insulation and protection of the n-type polysilicon layer in the following wet etching of the silicon substrate needed to reveal the electrodes. At this point the holes refilling step by LPCVD layers is completed and the top surface of the wafer is flat. The top dielectric ONO layers are removed selectively to provide electrical access to the core polysilicon conductor and a metal layer is deposited in these contact regions to create pads for electrical connection to each of the sites (Figure 3.1C). In Figure 3.1 we only

show one individual electrode. Needless to say, the process can form hundreds of thousands of these needles side by side. The next step is to expose the tip and coat it with a conductor to form the recording/stimulation site. This is achieved by doing a maskless blanket silicon plasma etch to expose the electrodes and then using an oxynitride RIE etch to expose only the tip by etching the outer ONO layer and metallizing the tip, typically with gold, using a double-layer lift-off technique (Figure 3.1D). Details of the tip dielectric etching and metallization are discussed in the following sections. Next, a wet silicon etchant such as EDP is used to dissolve the substrate and sacrificial polysilicon, leaving behind insulated and instrumented electrodes (Figure 3.1E). The details of the above process steps are discussed in the following sections. It is noted that another research group [113] had proposed and fabricated an electrode array using the RIE and refill technology to refill 250 µm deep and 5-10 µm diameter holes in silicon substrates using LPCVD tungsten (W) films to make an electrode array for extracellular in vitro application. However, this technology is not capable of producing the implantable and dense arrays that are needed for cortical applications.
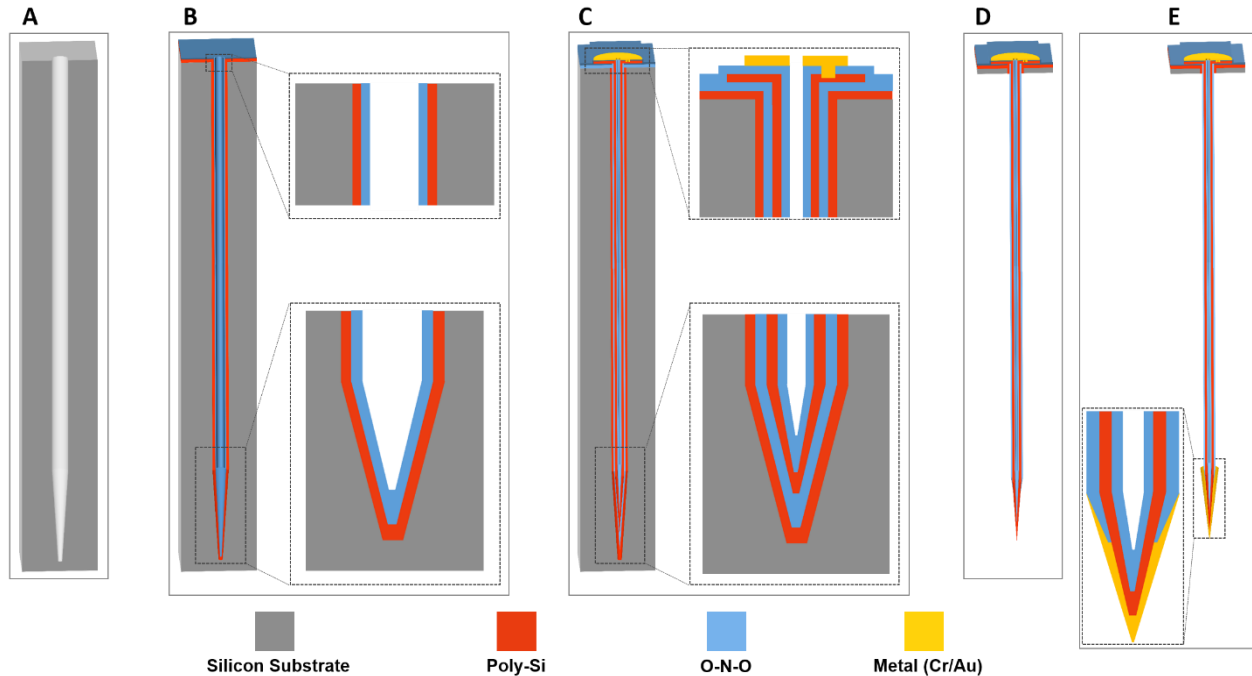
Figure 3.1: High-density high-electrode-count probe array fabrication technology. (A) Deep ultra-high aspect-ratio DRIE of <25µm diameter holes, DRIE lag effect is utilized to get tapered profile at the bottom of holes which is required to obtain sharp electrode tips. (B) Refilling of holes with multiple low-pressure chemical vapor deposited (LPCVD) films: 1- sacrificial polysilicon to reduce shank thickness, 2- outer oxide-nitride-oxide (ONO) insulator. (C) n-type polysilicon and ONO LPCVD as the electrode conductive core and the inner ONO insulator layer respectively followed by Contact pads patterning on wafer top to electrically access the electrode conductive core. (D) Maskless DRIE of silicon substrate to expose the electrodes followed by RIE etching of the ONO layer at the tip to expose the n-type polysilicon and electrodes tip metallization using a lift-off process to form ohmic contact to obtain proper impedance required for electrophysiological recording. (E) Dissolving the substrate and sacrificial silicon by EDP etching.

3.2.1.1 Deep High-Aspect-Ratio DRIE

A customized fixed-parameter DRIE recipe is used to form the deep high-aspect-ratio holes. It also utilizes DRIE lag effect [83-85] to taper the bottom of the holes to form sharp tips (Fig. 3.1A). Tip sharpness is critical for array implantation into the brain tissue, for reducing tissue damage and consequently increasing chronic stability as discussed in the previous chapter. We used an inductively coupled plasma (ICP) STS Pegasus etcher to conduct all the experiments. The standard

recipe has fixed process parameters throughout the etch. The deposition sub-cycle is 2 seconds long with a 13.56 MHz ICP power of 2000 W, pressure of 24 mTorr, and C_4F_8 flow of 250 sccm. The etch sub-cycle is 2.6 seconds with the ICP power at 2800 W, 380 kHz RF bias power at 60 W, pressure at 30 mTorr, SF_6 flow at 390 sccm, and O_2 flow at 39 sccm. Table 7 shows the DRIE process parameters used to make deep holes with tapered sidewall profile.

To obtain the deep etching with tapered profile and converged sidewalls to form a sharp tip, the DRIE process is performed for 210 minutes to ensure it has reached its limits due to DRIE lag effect. A thick oxide hard mask along with a thick photoresist film was needed to provide sufficient masking materials for the long DRIE process. As shown in Figure 3.2, ~10 μm-thick SPR220 (7.0) photoresist in addition to 2 μm-thick SiO_2 layer is used as the DRIE mask materials. Circular holes with different diameters ranging from 15-35 μm are etched with the fixed-parameter recipe. As shown in Figure 3.3, 15 μm and 25 μm holes are etched to <400 μm and 482 μm within 210 min respectively. The 35 μm holes, however, are etched all the way through the wafer (~550 μm). Tapering and convergence of sidewalls are observed at the bottom of the holes. Since the holes converge to submicron points at the very bottom, sharp points cannot observed by cleaving the silicon wafers. Due to the ion flux and ion energy dependency on in-plane aspect-ratio (Ø/Ø for holes and L/W for trenches), obtaining high-aspect-ratio in hole/via etching is more difficult than etching a trench with the same width as the hole diameter. After DRIE processing is done, the remaining photoresist/oxide mask layer is stripped before the following LPCVD films depositions.

DRIE Recipe	Etch			Passivation	
	380 kHz Bias Power	Step Time	Pressure	Step Time	Pressure
	(Watt)	(s)	(mTorr)	(s)	(mTorr)
Fixed	60	2	30	2.6	24
Time	210 min				

Table 7: DRIE process parameters (fixed-parameter recipe) used to make deep holes with tapered sidewall profile.
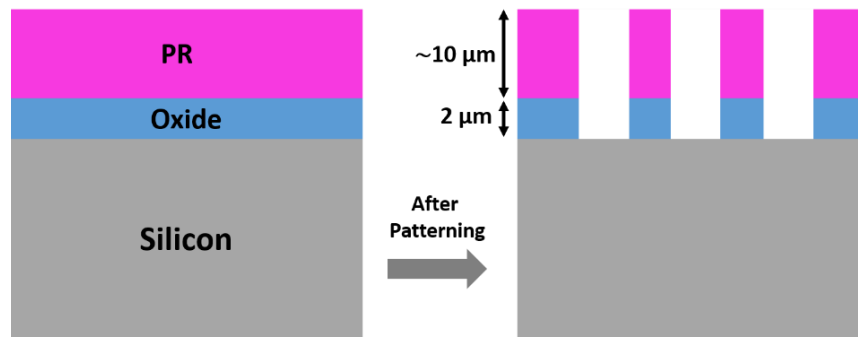
Figure 3.2: DRIE masking material used for ultra-deep high-aspect-ratio long DRIE processes.
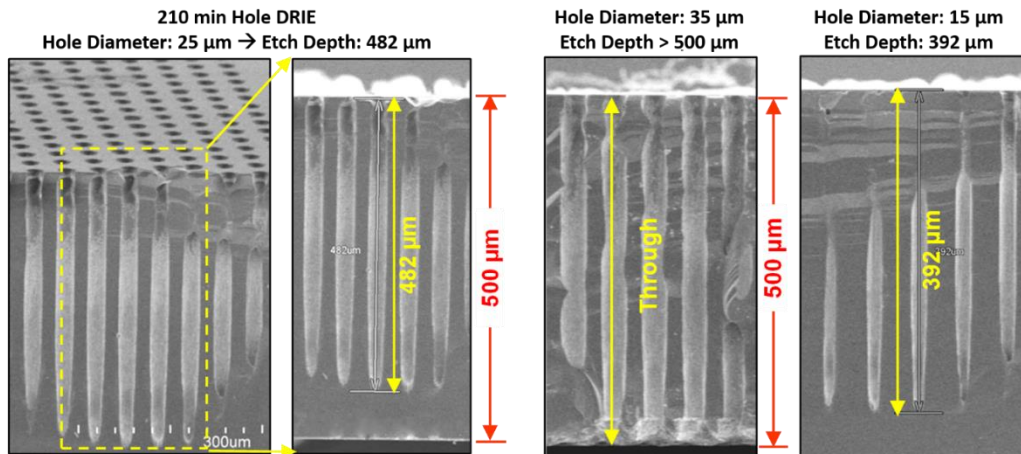
Figure 3.3: SEM images of holes with various diameter etched for 210 min with the fixed-parameter process. The bottom of the holes converges to a sharp point and etch is terminated.

3.2.1.2 Refilling Holes with LPCVD Films Deposition

To obtain high quality, conformal and uniform deposition inside the deep high aspect ratio etched holes, low pressure chemical vapor deposition (LPCVD) is used. LPCVD is a chemical vapor deposition technique that uses heat to initiate a reaction of a precursor gas on the solid substrate to form a solid phase material. In LPCVD, the substrates are usually heated and the reactions occur as gas species hit the substrate, therefore, the deposited films have very high quality and uniformity. The low pressure environment in the LPCVD process reduces the unwanted gas phase reactions and collisions, therefore, gas species reach all area, even narrow gaps and channels, which results in a uniform and conformal deposition.

The following LPCVD depositions are done to form the electrodes structural materials:

1- **Sacrificial Layer:** A 4 μm-thick polysilicon as the sacrificial layer to reduce the final electrode shank diameter,

2- **Outer Insulator Layer**: An oxide-nitride-oxide (ONO) composite layer with a total thickness of 1.25 μm as an electrical insulation layer and a protective layer (etch stop) in the following wet silicon etching process.

3- **Conductive Core Layer:** An n-type in-situ doped polysilicon layer with a thickness of 2 μm as the electrode conductive core.

4- **Inner Insulator Layer:** Another oxide-nitride-oxide (ONO) insulator layer as the inner insulator and etching protection layer with a total thickness of 1.25 μm.

Figure 3.4 schematically depicts the deposited LPCVD layers relative position inside the etched holes. Table 8 presents the LPCVD process details used to deposit the above films.
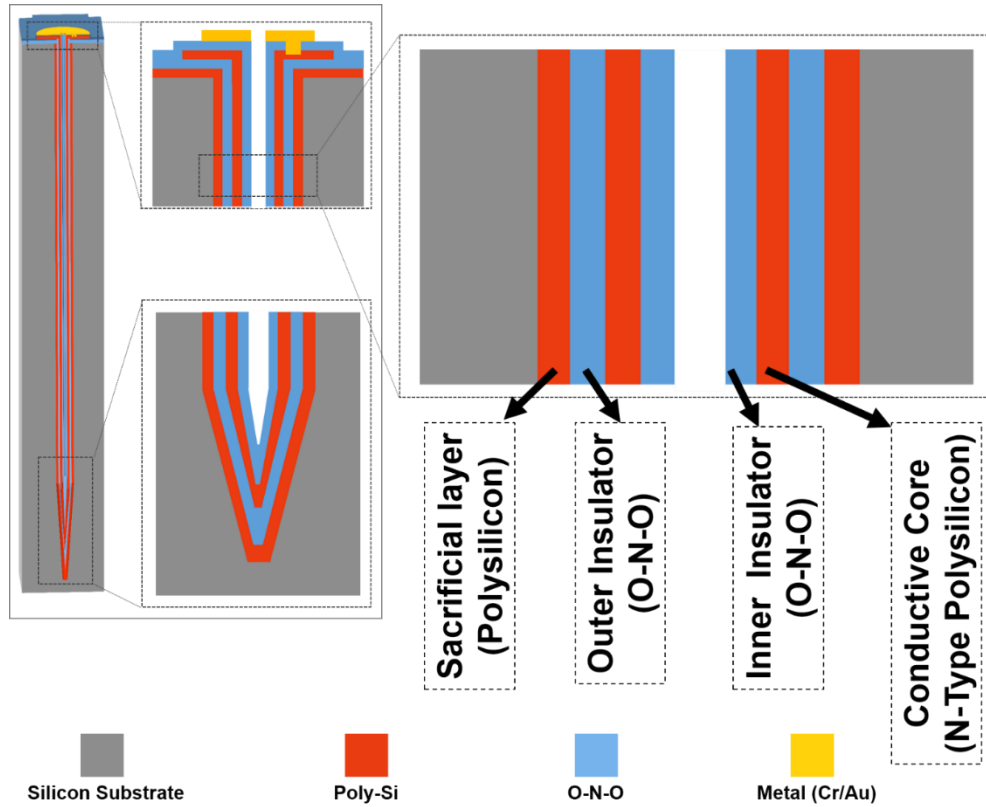
Figure 3.4: Deposited LPCVD films to refill the etched holes. Polysilicon is used as the sacrificial layer, ONO is used as the insulation and etch stop layer, and doped polysilicon is used as the conductive core.

LPCVD Process	Pressure (mT)	Temperature (ºC)	Process Gases	Gas Flows (sccm)	Deposition Time (min)	Dep. Rate (Å/min)	Avg. Film Thickness (Å)	Deposition Non-uniformity%	Avg Stress (MPa)
Polysilicon	220	585	SiH$_4$	85	910	44	~ 40000	1.22	+288
HTO	350	900	DCS/N$_2$O	60/120	135	37	~ 5000	1.90	-170
Nitride	200	800	DCS/NH$_3$	50/150	47	53	~ 2500	1.66	+1076
N-type Polysilicon	300	585	SiH$_4$/PH$_3$	70/30	606	33	~ 20000	0.84	+335

Table 8: LPCVD process parameters used to deposit the polysilicon, high temperature oxide (HTO), silicon nitride and n-type polysilicon layers.

3.2.1.3 Electrode Tip Metallization and Releasing the Electrodes

Figure 3.5 illustrates on approach for tip metallization to form the recording sites discussed earlier. This tip metallization process begins with a mask-less short (10 min) standard DRIE process to etch the silicon substrate and expose a certain length of the electrode tips (Figure 3.5 A). Next, the outer ONO layer is etched using an oxynitride RIE etch to expose the n-type polysilicon at the tip (Figure 3.5B). Next a blanket deposition of a 2 μm-thick Al layer is done using sputtering to obtain good step coverage and sidewall deposition (Figure 3.5C) followed by photoresist coating and reflow to expose the sharp part of the tip. The PR reflow process is done on a hotplate at 115 $^{\circ}$C for 20 minutes in atmospheric pressure (Figure 3.5D). Next, an oxygen plasma etch is carried out to remove the thinner parts of the PR layer on the tip exposing the Al layer (Figure 3.5E). The tip Al layer is then over-etched to form undercut in the Al layer underneath the PR which will facilitate the lift-off process later (Figure 3.5F). Next, a Cr/Au layer is deposited on the electrode tips using an evaporator. This tip metallization process is finished by a lift-off process to etch away the Al and PR layers. Figure 3.6 shows the SEM images of the electrode tips throughout this tip metallization process.

A) Electrode exposing

B) Outer ONO etch to expose N-Poly

C) Thick Al deposition

D) PR coating and reflow to expose the tip Al layer

E) Oxygen Plasma to etch the thinner PR layer parts

F) Tip Al over-etching to form undercut under the PR layer

G) Cr/Au deposition using evaporation technique

H) Al and PR lift-off

Silicon Substrate   ONO   N-type Polysilicon

Aluminum   Photoresist   Site Metal Layer (Cr/Au)

Figure 3.5: Electrode tip metallization process to form the recording sites. (A) Exposing the electrode tips using a maskless short DRIE to etch the silicon substrate, (B) exposing the n-type polysilicon layer at the tip by etching the outer ONO layer, (C) thick Aluminum layer deposition using sputtering as the sacrificial layer, (D) PR spin coating and reflow to expose the tip Al layer, (E) oxygen plasma etching to remove the thinner PR layer on the exposed tip, (F) over-etching of the tip Al layer to form an undercut under the PR layer, (G) recording site metal layer (Cr/Au) deposition using electron-beam evaporation technique, (H) Al and PR layers lift-off using wet etching in Al etchant.
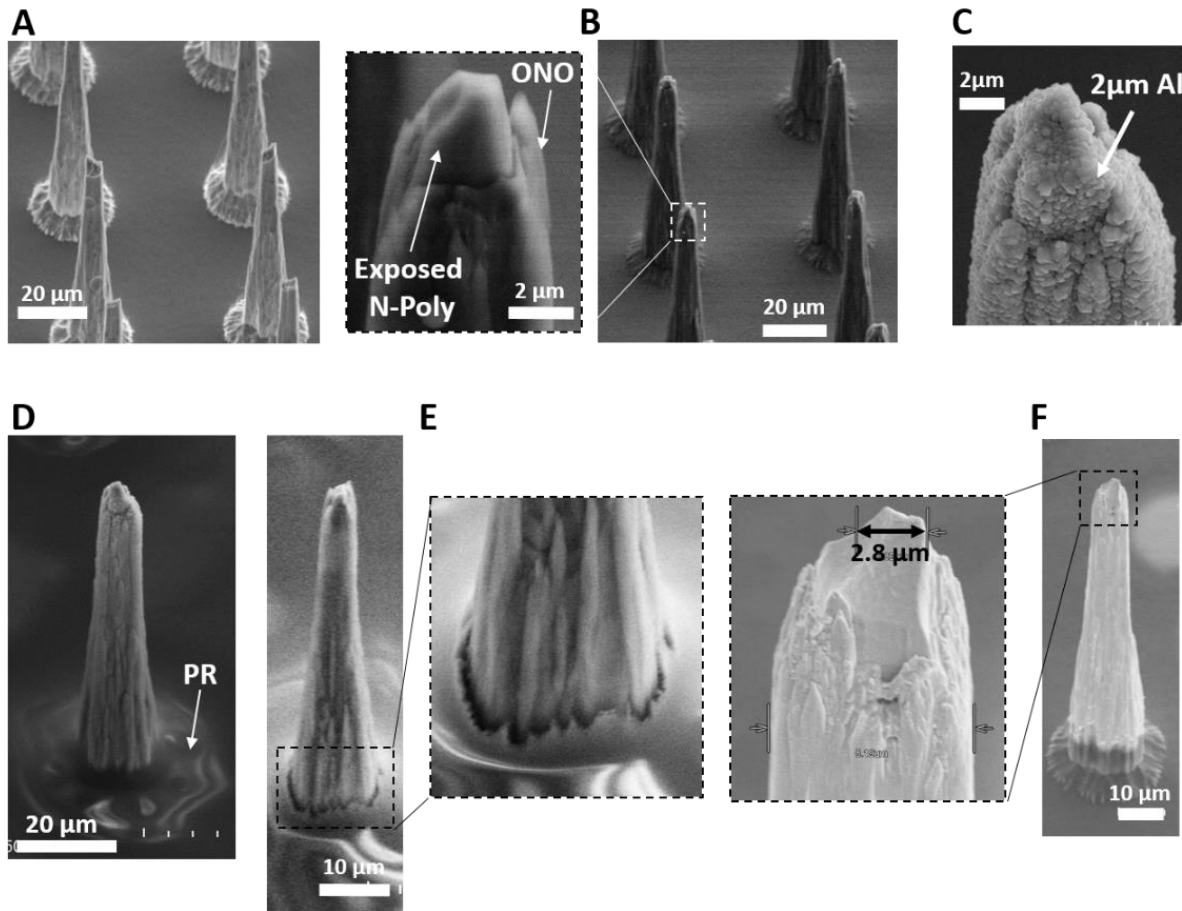
Figure 3.6: SEM images of the electrode tips throughout the tip metallization process. (A) Electrode tips exposing after etching the first few tens of microns of the silicon substrate, (B) exposing the n-type polysilicon layer at the tip, (C) after thick sacrificial Al layer deposition, (D) After PR coating, reflow, oxygen plasma etching and Al over-etching, the undercut under the PR is evident in the SEM image, (E) electrode tips is metallized after Cr/Au layer deposition and lift-off.

In order to release the electrodes, the thick silicon substrate needs to be removed while electrodes remain intact, therefore, an etching technique with ultra-high selectivity between silicon and oxide/nitride etching is needed. Most dry etching techniques have oxide/nitride etch rates comparable to silicon etch rate, and are not suitable for this application. Anisotropic wet silicon etching processes such as KOH, TMAH and EDP however, exhibit very high selectivity between silicon and oxide/nitride etching. We used Ethylenediamine Pyrocatechol (EDP) etching technique

53

due to its high etch selectivity and etch rates. We measured the EDP etch rate for silicon to be around 80 μm/hour at 115 °C while it does not etch oxide or nitride at any appreciable rates.

This tip metallization process resulted in a low yield (<5%) due to a number of reasons. First, in most high-density arrays (with 50 μm pitch), because the photoresist has high viscosity it covers the entire surface of the dense array of tips. This will prohibit exposing the tips by oxygen plasma etching (Figure 3.5 D and E) and result drastically lowers the lift-off yield as shown in Figure 3.7. Second, the tip metal layer was delaminated after the EDP etching step as shown in Figure 3.8. This could be due to the poor adhesion of Cr/Au layers to the electrodes surface which can be improved by further cleaning of the electrodes before site metal deposition step. Although using this process, the recording site surface area can be accurately controlled, this metallization process is only compatible with arrays of electrodes with the same height (length), therefore another recording site formation process is developed to be used for arrays with variable electrode lengths as described in section 3.2.2.3.
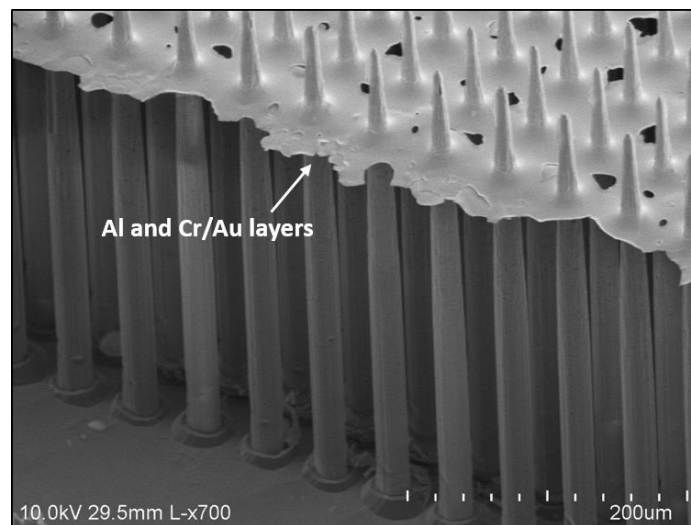
Figure 3.7: Lift-off process failure: poor conformal coverage of high-density electrodes with photoresist layer prohibits exposing the tips by oxygen plasma etching which is based on the difference of the photoresist thickness at the tips and the bottom surface.
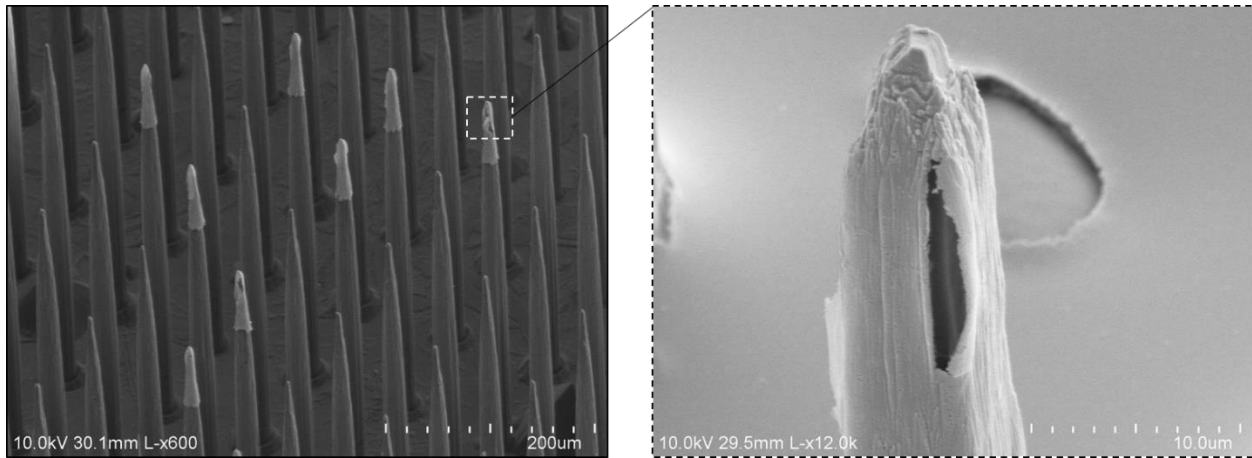
Figure 3.8: Delamination of the tip metal layer during the releasing process (EDP etching) which is mainly due to the poor adhesion of metal layers to the electrode surface.

3.2.2 Modified Process to Obtain Millimeter-long Electrodes

Human Brain neural recording/stimulation applications require electrodes with lengths of 1 to 100 mm [75], while centimeter-long probes are needed mainly for reaching deep structures in human subjects, millimeter-long probes are needed even for non-human subject. In the fabrication process presented in Figure 3.9, the electrode length is defined by the DRIE Aspect-Ratio Dependent Etch (ARDE) and DRIE lag effects, therefore, for opening holes with a diameter of <30 μm, the electrode length is limited to ~500 μm. In order to obtain neural arrays with millimeter-long electrodes, we have developed another novel process which is based on bonding of multiple silicon wafers. This approach starts with preparing multiple separate wafers containing through-wafer etched holes using a special ultra-deep high-aspect-ratio DRIE process (UDRIE) as described in the following section. One wafer is etched using the custom DRIE recipe described in the previous section to utilize the DRIE lag effect to form the tip shape and sharpness (Figure 3.9 (a)). This

55

and all other wafers are bonded to form mm-deep holes as shown in Figure 3.9 (b). These long

holes are again refilled with the same fabrication process described in Figure 3.1 to obtain mm-

long electrode arrays. The details of each one of these steps are discussed in the following sections.
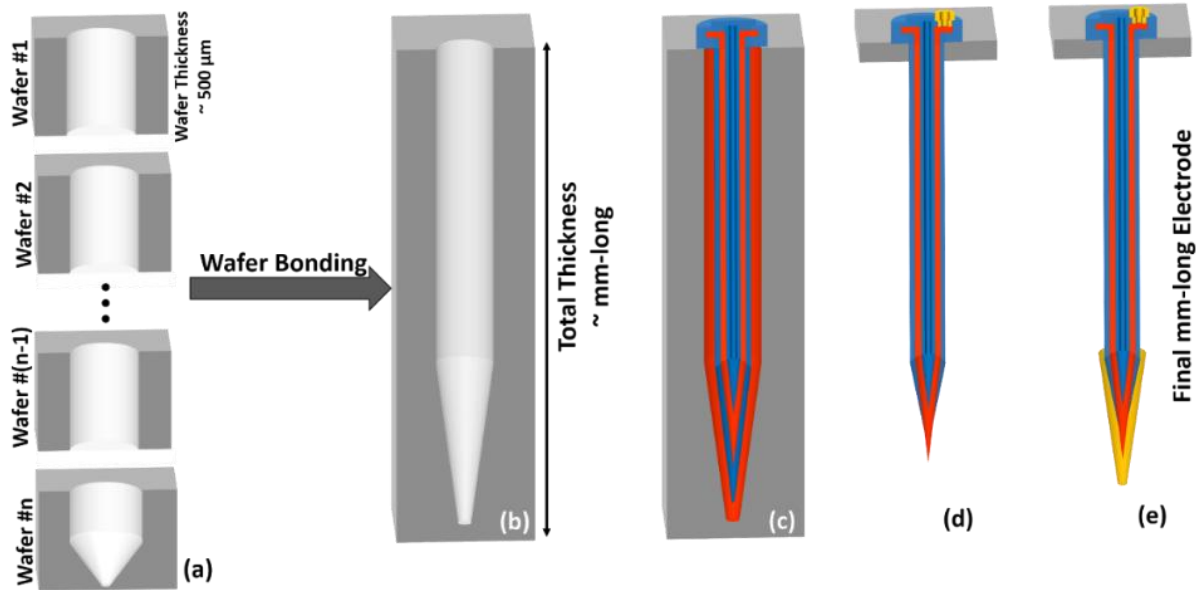
Figure 3.9: Fabrication of millimeter-long needles: (a) Process starts with preparing multiple separate wafers containing through-wafer etched holes using ultra-deep high-aspect-ratio ramped recipe and one wafer etched using a custom DRIE recipe to utilize the DRIE lag effect to form the tip shape and sharpness. (b) Next, all the wafers are bonded to form a mm-deep hole, (c-e) then the holes will be refilled with the same fabrication process described in Fig. 3.1 to obtain mm-long electrode arrays.

3.2.2.1 Custom-Developed Ultra-Deep Ultra-High Aspect-Ratio DRIE Recipe (UDRIE)

We have developed a modified DRIE process to minimize the standard DRIE process shortcomings (ARDE induced tapered sidewall/etch termination/DRIE lag, and pattern dependency) presented in the previous section. Ultra-deep ultra-high AR features with controlled sidewall slope are obtained by dynamically ramping the Bosch DRIE process parameters [83-83].

This section will present detailed description of this modified DRIE process with ramped process parameters and comparison with the standard fixed-parameter recipe.

We use an inductively coupled plasma (ICP) Surface STS Pegasus etcher to conduct all the experiments. Standard DRIE recipes have fixed process parameters throughout the etch step. The etcher is operated at 13.56 MHz ICP power level of 2800 W and 380 kHz RF bias power at 60 W in the etch sub-cycle and 2000 W ICP power in the passivation sub-cycle. C_4F_8 and SF_6 gas species are alternated between the passivation and etching steps at 24 mTorr and 30 mTorr chamber pressure, respectively. Holes with different diameters ranging from 15–35 μm are also etched with the standard fixed-parameter recipe. As shown in Figure 3.3, 15 μm holes are etched to <400 μm within 210 min. The apparent etch rate is close to that of 5 μm trenches at ~2 μm/min. The 35 μm holes however are beyond being etched all the way through the wafer (~550 μm). Tapering and convergence of sidewalls are observed at the bottom of the holes. Since the holes converge to submicron points at the very bottom, sharp points are not observed by cleaving the silicon wafers. Due to the ion flux and ion energy dependency on in-plane aspect-ratio (Ø/Ø for holes and L/W for trenches), obtaining HAR DRIE in hole/via etching is more difficult than etching trench with the same width as the hole diameter. This standard fixed-parameter recipe is used as a baseline recipe to develop and tune the dynamic recipe with ramped process parameters to achieve straight sidewalls and flat feature bottom. We attempt to address the key DRIE shortcomings (ARDE induced sidewall tapering, etch depth limitations and DRIE lag; and pattern dependency) in order to achieve ultra-deep ultra-high AR silicon etch by further developing and characterizing a modified Bosch DRIE process initially proposed by Owen et al. [85]. Since these issues mainly originate from the reduction in transport of etchant agents and ion bombardments at the bottom of deep features as the AR increases, Bosch DRIE process parameters are continuously ramped to

optimize the DRIE conditions at each depth as the etch proceeds. The STS Pegasus ICP DRIE etcher allows process parameters to be ramped from a start value to an end value. The ramp rates of different parameters are set in order to maintain as constant and high etch rate as possible as AR increases. Then the overall etch time (recipe duration) is set to reach a desired etch depth. The start and end values of the various parameters are calculated from the product of ramp rate and etch duration. Three parameters of the DRIE process are ramped: 380 kHz RF bias platen power, etching and passivation sub-cycle duration, and chamber pressure. It should be noted that the start and end values need to be characterized for specific feature sizes, etch patterns and target depths. For example, for 2-10 μm trench width, the following set of ramped parameters are found to best compensate the reduced etch rate and result in deep HAR structures by enhancing the etching agents effect during the total 150 min DRIE duration: the 380-kHz bias power during etch step is increased from 60 W to 140 W; the etch sub-cycle duration starts at 2.6 s and is ramped up to 5.6 s; and the passivation step duration is increased from 2 s to 3.5 s. The chamber pressure is also changed throughout the process: the passivation step chamber pressure is ramped up from 24 mTorr to 34 mTorr whereas the etch step chamber pressure is ramped down from 30 mTorr to 15 mTorr. The relevant parameters for the fixed and ramped processes are compared in Table 9.

In contrast to the converged bottoms shown in Figure 3.3, the ramped parameter process can create flat bottoms even for etching circular holes as shown in Figure 3.10. Etch rate is also increased compared to the fixed-parameter recipe. 25 μm diameter holes are etched to >500 μm within 150 min using the ramped process while 210 min of the original fixed-parameter process only obtained maximum depth of <400 μm. The in-plane AR (length /width, L/W) of the etched features also play an important role on the etch rate. 15 μm wide trenches reach a depth of more than 520 μm whereas the 15 μm diameter circular holes only reach a depth of ~400 μm with the same

58

150 min ramped DRIE process. A rectangular pattern (8 µm×50 µm) is also etched deeper than

15 µm diameter circular holes. This verifies that etch rate is also in-plane AR (W/L) dependent.

Long lines etch considerably faster than circular holes of the same width, or of even larger width.

Recipe	Etch			Passivation	
	380 kHz Bias Power	Step Time	Pressure	Step Time	Pressure
	(Watt)	(s)	(mTorr)	(s)	(mTorr)
Fixed	60	2	30	2.6	24
Ramped	60→140	2.6→5.6	30→15	2→3.5	24→34
Time	150 min				

Table 9: Fixed-Parameter vs. Ramped-Parameter DRIE process parameters [Tan17] for a 150-minute DRIE duration.
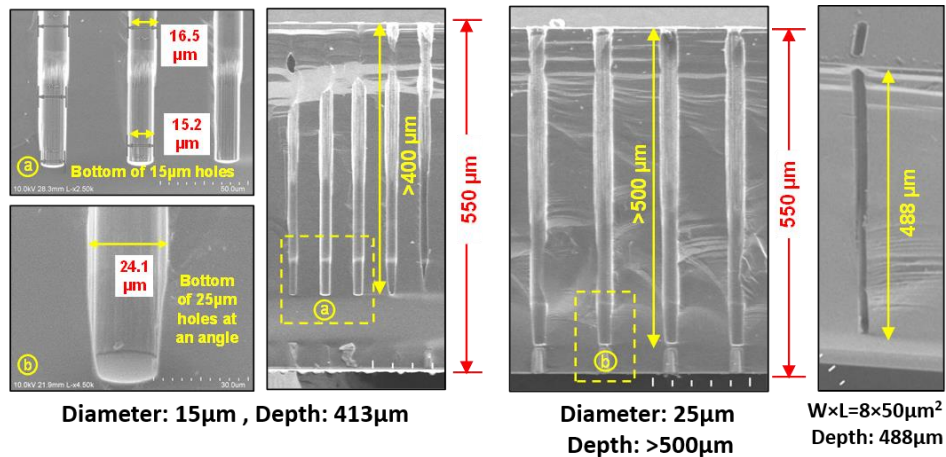
Figure 3.10: Ramped-parameter DRIE recipe results: Higher etch rate, larger depth, relatively straight sidewalls and flat bottom are obtained compared to the fixed-parameter recipe. 25 µm diameter holes are etched to >550 µm within 150 min using the ramped-parameter recipe, while 210 min etch by fixed-parameter DRIE recipe only reaches maximum depth of <400 µm.

3.2.2.2 Wafer Bonding using Silicon Fusion Bonding

Silicon fusion bonding is the joining together of two silicon substrates without the use of any additional intermediate layers or adhesives [86]. There are two types of silicon fusion bonding, hydrophobic and hydrophilic. In hydrophobic bonding, silicon surfaces are rendered hydrophobic by removing native oxide on the silicon surfaces which is done by immersing in hydrofluoric acid (HF) [87]. After HF treatment, the silicon surfaces are mainly terminated by hydrogen and fluorine [88]. The bonding mechanism of hydrophobic silicon surfaces is due to the bonding between Si-F and H-Si across silicon substrate pairs [89]. In hydrophilic silicon bonding however, the silicon wafers are immersed in a standard RCA solution to make the silicon surfaces hydrophilic. After surface treatment with RCA and plasma surface treatment, the silicon wafers start to bond as soon as they get in atomic contact even at room temperature due to hydrogen bonds between hydroxyl groups and water molecules adsorbed on the wafer surfaces [90]. In both hydrophobic and hydrophilic silicon fusion bonding methods, after the pre-bonding step at room temperature, the wafers have to go through an annealing process for increasing the bond strength. Depending on the bonding method, the annealing temperature can be between 150-1100 °C. However, for successful full wafer bonding, annealing temperatures greater than 800 °C is recommended [87,91]. The bonding strength of hydrophobic fusion bonding during the room-temperature pre-bonding is weaker than that of hydrophilic bonding and is more susceptible to failure by surface contaminations, therefore, we have used the hydrophilic fusion bonding method with the following steps:

    1) RCA cleaning of silicon wafers

    2) Plasma surface treatment

3) Aligning and room-temperature pre-bonding

4) High-Temperature Annealing

3.2.2.2.1 RCA Cleaning

Silicon fusion bonding is very sensitive to surface contaminations, strong void-free bonding is contingent on clean surfaces with no particles, organic and/or ionic contaminations, therefore, after the DRIE step, the remaining DRIE mask materials (PR and oxide) will be stripped and then wafers are cleaned using the standard RCA cleaning:

1) Standard Clean 1 (SC-1, Organic clean): NH_4OH : H_2O_2 : Deionized H_2O (1:1:5) (at 85 ^{o}C, 15 minutes)

2) Standard Clean 2 (Sc-2, Ionic clean): HCl : H_2O_2 : Deionized H_2O (1:1:6) (at 85 ^{o}C, 15 minutes)

After RCA cleaning, wafers are rinsed and dried using Spin Rinse Dryer (SRD).

3.2.2.2.2 Plasma Surface Treatment

It has been demonstrated that using a combination of RCA and plasma activation provides the best pre-bond strength for room-temperature hydrophilic silicon fusion pre-bonding [87]. Various gases plasma including O_2, N_2, H_2 can be used. Plasma surface activation enhances the chemical reactivity of the surface with water and other chemicals to form silanol bonds [92]. Another effect of plasma surface treatment is increasing surface charging forming field effects across the bonding surfaces, which increases the atomic mobility of reacting species in the interfaces of mating surfaces. Therefore, plasma surface treatment results in stronger pre-bonding between the silicon surfaces [87,93]. Based on these studies, we performed a N_2 plasma right after the RCA cleaning using the Suss MicroTec NanoPREP 12 tool that generates a N_2 plasma scanning over the wafer

surface in air. The plasma power, number of scanning iterations and scanning speed can be modified for various surface activation applications. We used a plasma power of 500 W and 6 scanning iterations. Another important step after the plasma activation and before pre-bonding is to increase the number of bonds between the surface hydroxyl groups and water molecules. This can be done by rinsing and drying the wafers. After the plasma surface treatment, wafers are ready for the pre-bonding step.

3.2.2.2.3 Wafer Aligning and pre-Bonding

Immediately after the plasma surface treatment, a bond aligner tool is used to align the etched holes on two wafers. Next, wafers are brought together which results in formation of pre-bonds as soon as they get in atomic contact. The following occurs during the pre-bonding process and the formed water molecule will migrate or diffuse along the interface during the high-temperature annealing step [86]:

Si–OH + OH–Si $\rightarrow$ Si–O–Si + H_2O
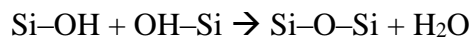
After aligning and pre-bonding which is done at room temperature and in air (atmospheric pressure), the pre-bonded silicon wafers are placed in a Suss MicroTec SB 6e bonder tool to apply force to the wafers in vacuum and heat them to further strength the bonds formed during the pre-bonding step and significantly reduce the voids formed at the interface of the bonding wafers. We have applied a force of 5 kN at 100 °C and pressure of 20 µTorr for 1 hour.

Figure 3.11 shows the infrared (IR) microscope image of two aligned wafers after the pre-bonding step, as shown the misalignment is around 6 µm.
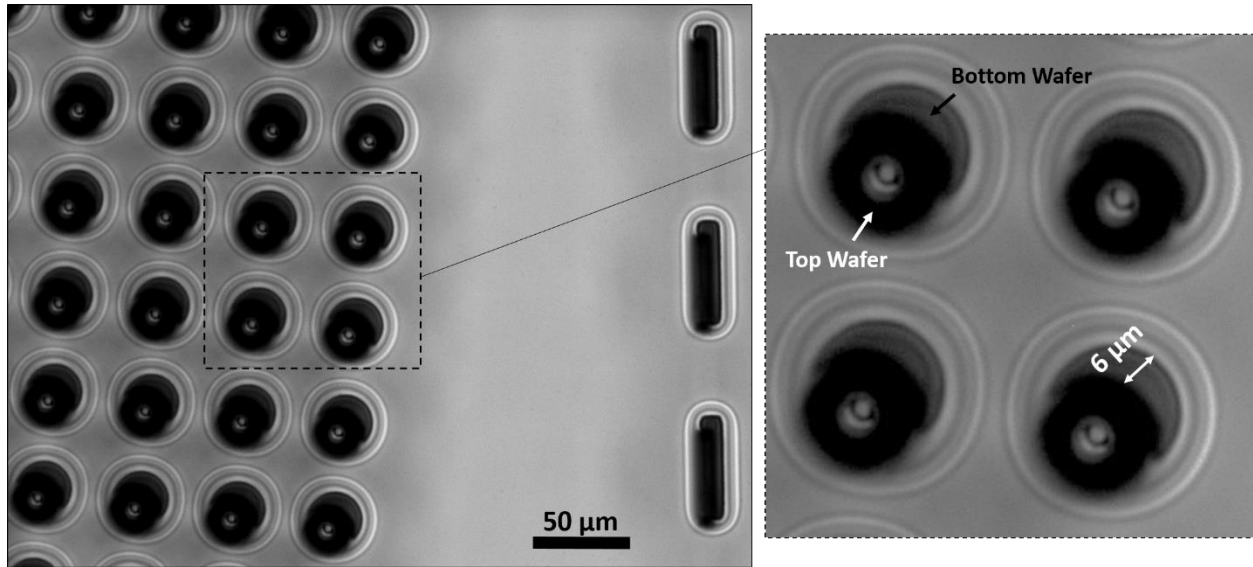
Figure 3.11: IR microscopy image of two aligned wafers after the pre-bonding step, as shown the misalignment is around 6 μm.

3.2.2.2.4 High-Temperature Annealing

Annealing at temperatures above 1000 $^{\circ}$C for several hours should result in almost complete bonding of the interface [91]. Above 800 °C native oxide gets viscous and starts to flow at the interface, which increases the area of contacted surfaces. So, the diffusion of trapped hydrogen molecules along the interface is enhanced and interface voids may reduce in size or disappear altogether [94]. After the pre-bonding step, the wafers are annealed at 1100 $^{\circ}$C in N_2 environment at atmospheric pressure for 12 hours. Figure 3.12 shows the Si-Si and Si-SiO_2 hydrophilic fusion bonding results. It should be noted that in case of Si-SiO_2 fusion bonding, it is recommended to use a high-quality oxide layer with high thickness uniformity across the wafer to prevent formation of gaps or voids, therefore dry or wet thermal oxidation is preferred to CVD deposited SiO_2 layers. The thickness of oxide layer in this bonding test was 2 μm, however, successful fusion bonding of Si-SiO_2 for various thicknesses is reported.

Imperfect local bonding interface is likely to form as shown in the Si-Si fusion bonding interface in Figure 3.12. However, relatively thick sacrificial polysilicon layer (~4 μm) used in our process completely fills these formed gaps and voids and prevents any major issues.
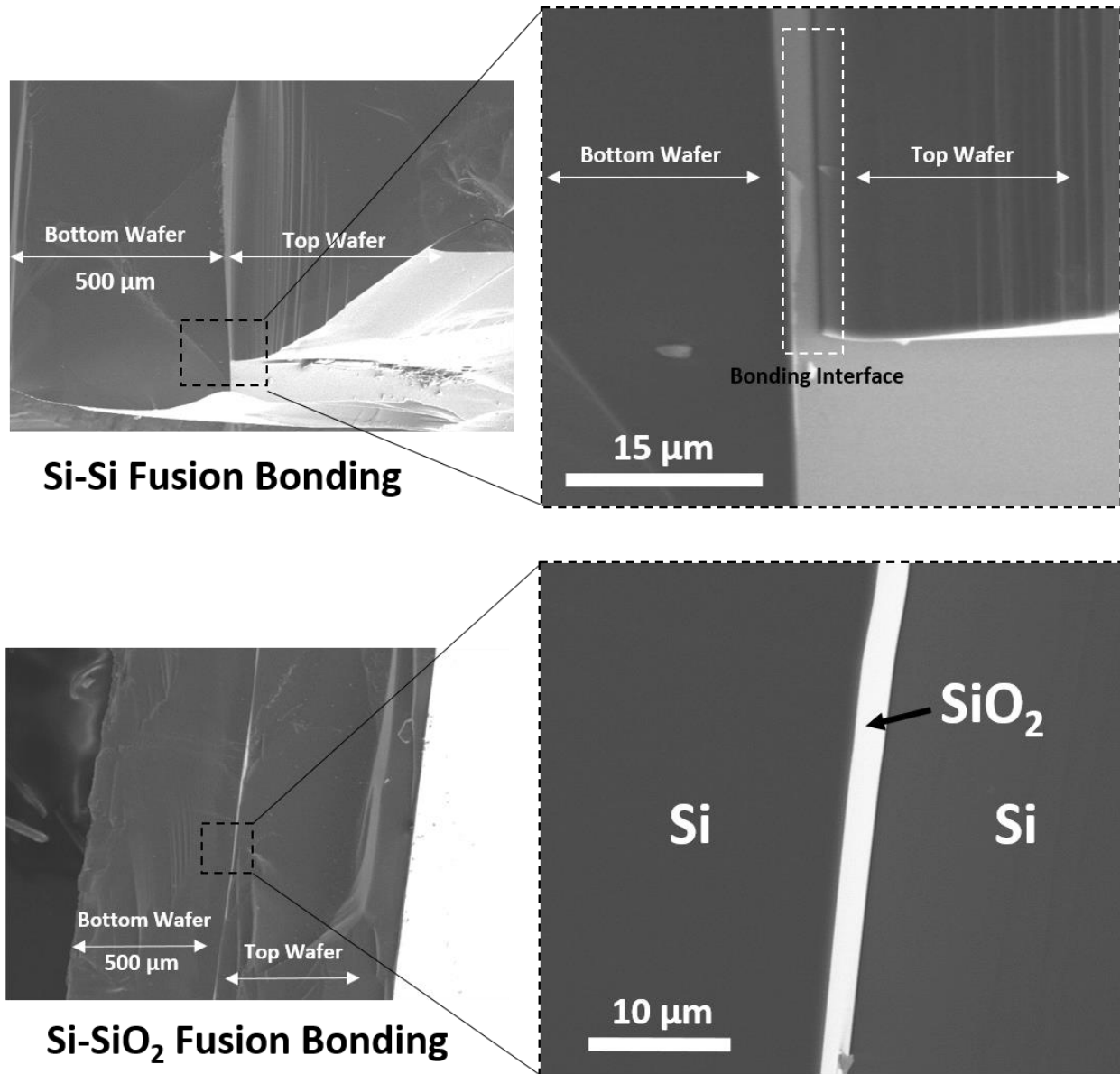
Figure 3.12: SEM images of hydrophilic Si-Si and Si-SiO$_2$ fusion bonding interfaces after high-temperature annealing step.

3.2.2.3 Electrodes Recording/Stimulation Site Formation

Conventional planar micro-electrode arrays use standard patterning techniques to define the electrode sites, this includes metal deposition, photolithography and dry/wet etching. The developed electrode array in this thesis, however, has an out-of-plane design which is incompatible with the mentioned standard patterning techniques. The tip metallization process described in section 3.2.1.3 exhibited yield issues and also limitations for arrays with electrodes of various length, therefore another process to define the recording sites is developed. We have developed a self-aligned site metallization process which relies on direction-dependent reactive ion etching (RIE) and metal deposition to circumvent the lithography step. Figure 3.13 shows the electrode site metallization process flow.

EDP etching dissolves the silicon substrate and sacrificial polysilicon layer, leaving behind the electrodes protected by the outer ONO dielectric layer (Figure 3.13A). Next, a highly directional RIE recipe is used to remove the ONO dielectric layer from the top-most joint between the electrode conical part and main shank body and exposing the underlying n-type polysilicon conductive electrode core (Figure 3.13B). This etching step duration should be optimized to make sure ONO etching only occurs at the topmost joint and the rest of the electrode remains insulated by the ONO dielectric layer. Electrode site electroplating seed layer (chromium and gold) is then deposited using an evaporation technique. Evaporation is used to exploit line-of-sight deposition (poor step coverage) to avoid deposition on electrode sidewalls (Figure 3.13C). Next, gold electroplating is done to reduce the electrode site impedance (Figure 3.13D). A wet etching step is then performed to remove the excess seed layer from the rest of the electrode array to avoid any electrical short circuit (Figure 3.13E). It's worth mentioning that the electrode site metallization is simplified by this self-aligned process which is based on direction-dependent RIE etching and

metal deposition. Another advantage of this approach is controllability over the electrode site surface area, which directly impacts the site impedance.
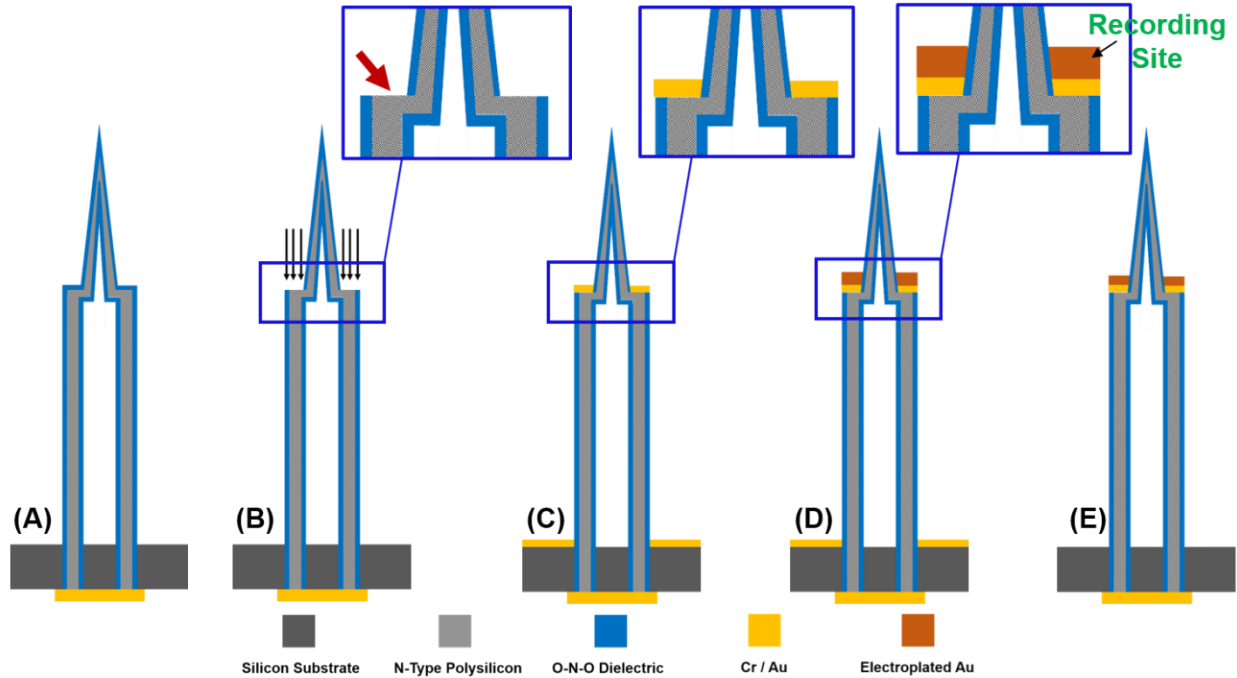
Figure 3.13: Electrodes recording/stimulation site formation: (A) Electrodes protected by the outer ONO dielectric layer after dissolving the silicon substrate and sacrificial polysilicon by EDP etching, (B) Removing the ONO layer from the topmost joint using a highly direction-dependent RIE process to expose the underlying n-type polysilicon conductive layer, (C) Metal seed layer (Cr/Au) deposition using evaporation technique, (D) Gold electroplating over the exposed n-type polysilicon coated with seed layer, (E) Wet etching to remove the excess seed layer from the rest of the electrode array to avoid any electrical short circuit.

The shortcomings and drawbacks of this process include: 1- Recording site surface area depends on the flat horizontal surface area exposed to the RIE plasma etching, therefore, it is hard to control the metallized site area and the site impedance post-fabrication. 2- The shifts along the electrode shank due to wafer bonding misalignment (discussed in section 5.2.2) result in unwanted horizontal surfaces that are exposed to the plasma and if RIE etching process is not accurately controlled can expose the n-type polysilicon at multiple positions along the shank. 3- The metal-deposited area can drastically change by even small tilting of the array, resulting in large variations

of site impedance. 4- In general, relying on the dielectric layer (ONO) thickness differences along the shank, directionality of the RIE etching and metal deposition processes is susceptible to repeatability and reliability issues, in particular by changing the array design such as electrodes length, diameter, etc.

We have employed the recording site formation process described in this section to make functional electrode arrays for *in vivo* recording, however, further research is required to obtain recording sites with proper impedance with high reliability, repeatability and stability.

3.3 Conclusions

In this chapter, we presented the developed techniques to fabricate 3D high-density high-count electrode arrays capable of realizing the near-ideal neural interface described in the previous chapter. These techniques include:

- A custom-developed DRIE process to make deep (500 μm) high aspect-ratio (20-30) thru-wafer holes with controlled sidewall slope,
- A method of extending the thru-wafer holes depth by bonding multiple silicon substrates using fusion bending technique,
- A process for conformal refilling of ultra-deep (~2 mm) ultra-high aspect-ratio (80-100) holes with dielectric and conductive films using LPCVD process,
- Methods of forming the recording sites using self-aligned maskless metallization processes.

Using this technology, we have obtained millimeter-long (1.2mm), narrow (10 to 20μm diameter), sharp (submicron tip size), high-density (400 electrodes/mm^2) high-count (5000+) electrode arrays. Some of the limitations and capabilities of these developed techniques are discussed in this

chapter. The experimental results including fabrication results, characterization data, *in vivo* tests and more detailed discussions on the technology capabilities and limitations are presented in chapter 4 and chapter 5.

Chapter 4: Sea of Electrodes Array (SEA) Experimental Results

The Sea of Electrodes Array (SEA) microfabrication technology described in the previous chapter was used to obtain high-density high-count electrode arrays to demonstrate the capability of this technology in terms of scalability, density and electrode count. In this chapter, we present the fabrication results of these technologies, mechanical and electrical characterizations of electrodes, and acute *in vivo* tests.

4.1 High-Density High-Electrode-Count Array

In this section the fabrication results of the proposed technology described in Figure 3.1 are presented. Figure 4.1A shows ~500µm deep, 25µm diameter holes with tapered bottom. Figure 4.1B shows a single electrode after exposing the conductor core (n-type polysilicon) by selectively etching the ONO dielectric layer from the electrode tip. Figure 4.1C is SEM image of a 72×72 electrode array with 50µm pitch, each electrode being ~500µm long, 20µm thick at the base and <2µm at the tip. A close-up of the metallized tip is shown in the lower inset. Figure 4.2 shows three sets of arrays with different electrode shank diameters, tip shape and sharpness. Scalability of this technology is demonstrated by fabricating arrays with various electrode counts. Figure 4.3 shows optical image of 32×32, 50×50 and 72×72 arrays of ~500µm long, 20µm diameter electrodes with spacing of 50µm. The mechanical strength of high-density electrode arrays is tested by inserting them into different materials similar to brain tissue such as Agar, hard-baked egg yolk and tofu; no electrodes broke in any test as shown in Figure 4.4.
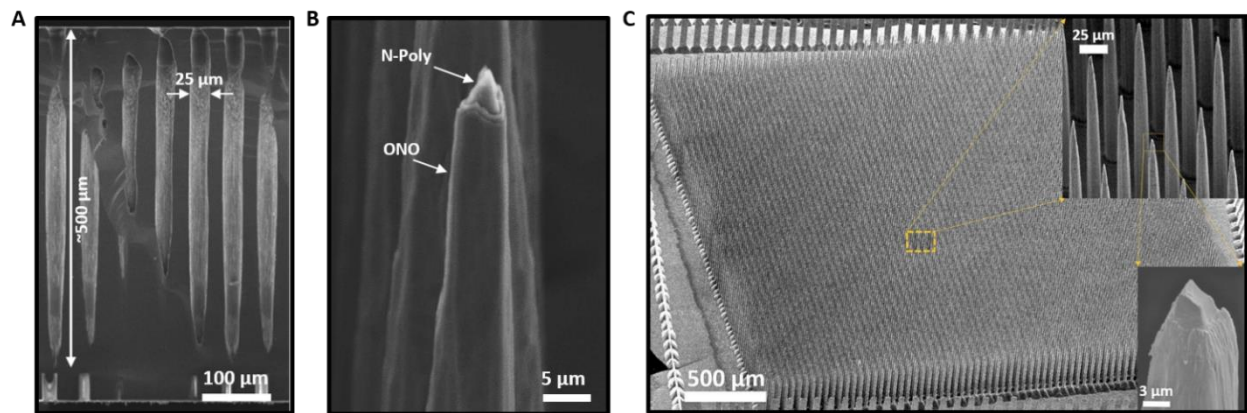
Figure 4.1: SEM images of fabrication process flow. (A) Deep high-aspect-ratio holes fabricated by the fixed-parameter DRIE process. (B) N-type poly-silicon (conductor core) at the electrode tip is exposed by RIE etching of the outer ONO layer. (C) SEM image of a 72×72 array: (upper inset) close image of individual electrodes, (lower inset) Metallized electrode tip.

4.2 Millimeter-Long Electrode Arrays

Millimeter-long probe arrays fabricated using the bonding-refilling technique described in Figure 3.9 are shown in Figure 4.5. In this process, four 500µm-thick silicon wafers are bonded using fusion bonding to obtain ~1.7 mm deep holes. The bonded stack of wafers is then processed using the fabrication technique described in Figure 3.1. 1.2mm long probe arrays with various number of shanks, pitch and size are realized by etching the top three silicon wafers away and leaving the bottom wafer as the substrate. For longer needles, more wafers can be bonded.

4.2.1 Electrode Recording/Stimulation Site Formation

Figure 4.6 shows the electrode recording/stimulation site formation using the approach described in Figure 3.13. As mentioned in the previous section, the ONO plasma etching duration is optimized to make sure ONO etching only occurs at the topmost joint and the rest of the electrode remains insulated, then a chromium/gold (300/1000 Å) seed layer is be deposited using the evaporation technique to obtain a directional deposition. Next, gold electroplating is done with

current density of 1.27 mA/cm^2 for 2 minutes. Figures 4.6A and 4.6C demonstrate the controllability of the metallization approach if the ONO etching is done properly (with optimized etching time). The electrode site is gold-plated.   Electroplating does not occur at the tip since the conductive n-type polysilicon is not exposed. Sites are gold-plated to reduce the impedance by increasing the surface roughness which results in larger surface area (Fig 4.6D). The electrode tip can also be metallized by increasing the ONO etching time and exposing the tip n-type polysilicon (Fig. 4.6E).
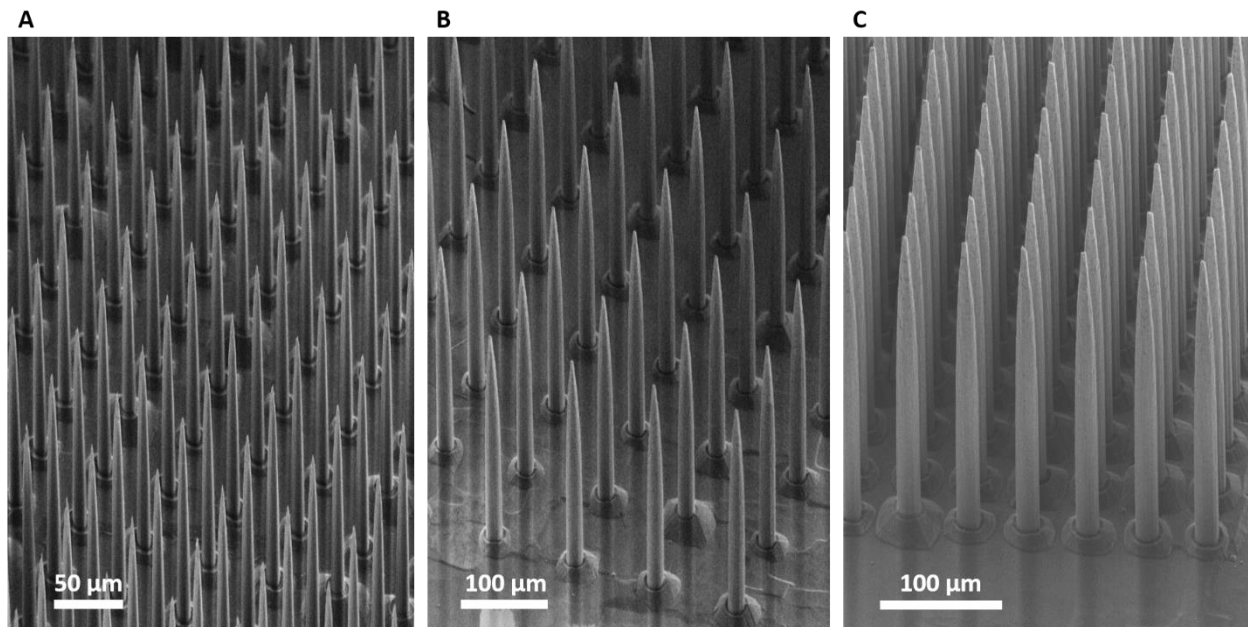
Figure 4.2: Fabricated electrode arrays using starting holes with different diameters: (A) ~10 um (B) ~20 um (C) ~30 um thick probe shanks resulted from 15 um, 25 um and 35 um hole diameter respectively.
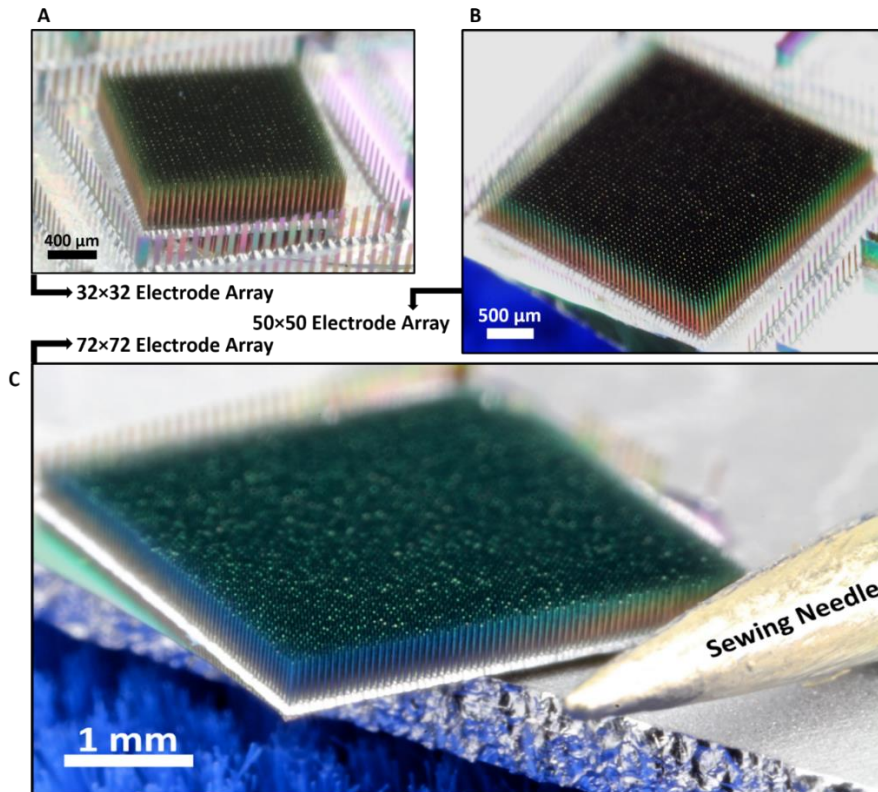
Figure 4.3: Demonstration of scalability of this approach: (A) 32×32 electrode array, (B) 50×50 electrode array, (C) 72×72 electrode array. Electrode pitch, length, thickness at the base and tip are 50 μm, 500 μm, 20 μm and <2 μm respectively for all the arrays.
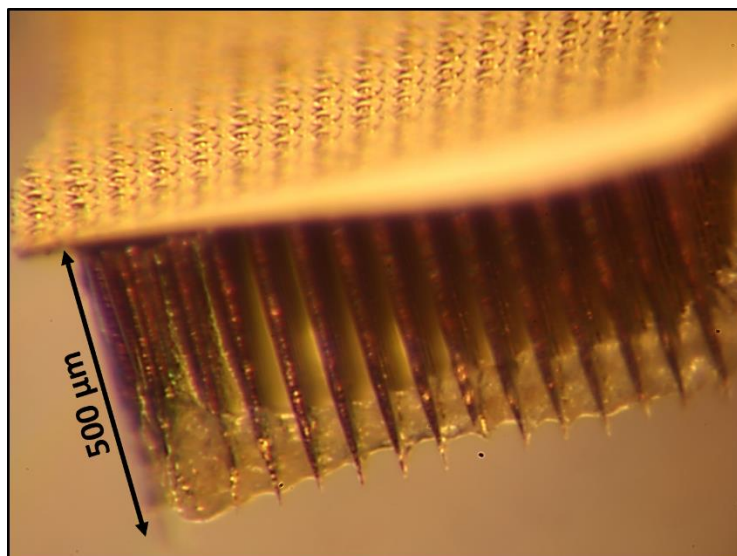
Figure 4.4: The electrode array strength is tested by implantation into various brain-like materials such as Agar, hard-baked egg yolk and tofu with no electrode breakage. Part of an array with 500 μm long electrodes, ~20 μm diameter and 50 μm spacing is showed after implantation in tofu and explanting afterwards.
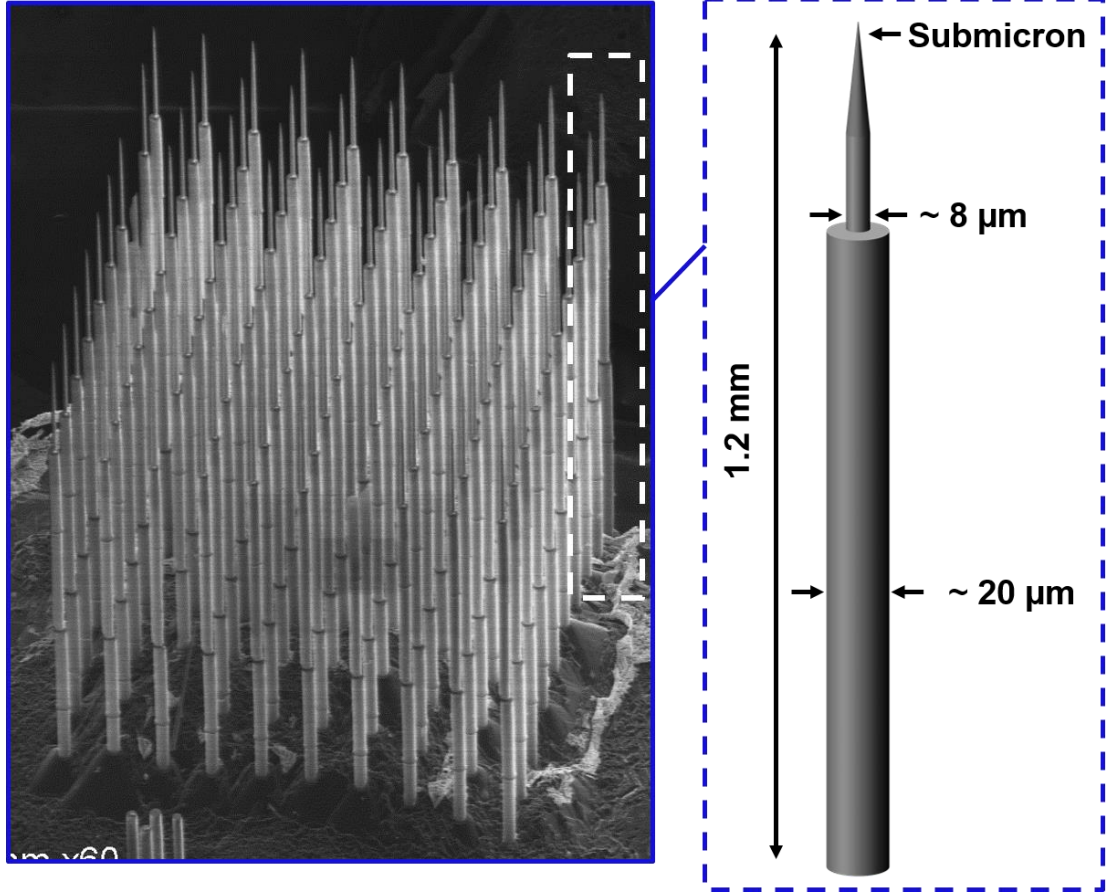
Figure 4.5: SEM images show the fabricated mm-long electrodes using the process described in Figure 3.9: 1.2 mm long shanks are realized by bonding four 500μm-thick silicon wafers and etching away the top three wafers to keep the last wafer as a backbone. As shown in the right part of the figure, electrode shanks are ~20 μm thick at the cylindrical base, ~8 μm thick at the tip conical base and submicron size at the tip.
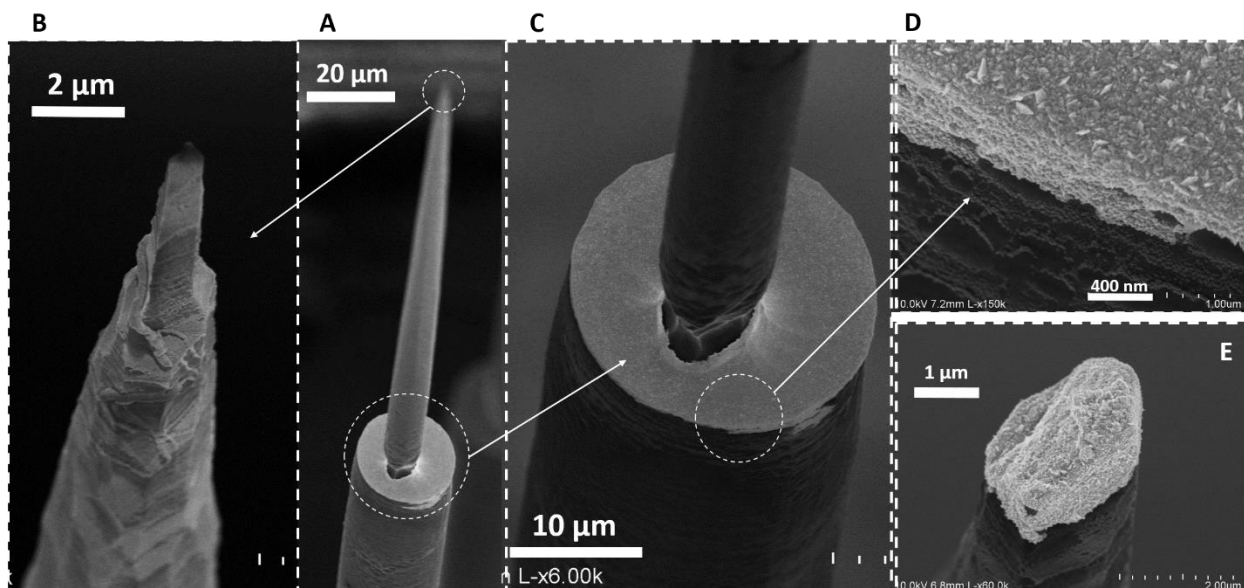
Figure 4.6: Electrodes recording site formation using the method described in Figure 3.13: (A) A single electrode after metallization of the recording site by gold electroplating, (B) A close-up of the electrode tip shows the controllability of the metallization process; tip ONO dielectric is not fully removed by optimizing the plasma etching time due to the thickness difference. (C) Gold-plated recording site with surface area >300 μm^2, (D) The interface between the electroplated gold layer and the electrode sidewall ONO layer. (E) Tip metallization can be obtained by increasing the ONO etching time to remove the tip ONO and expose the n-type polysilicon at the tip.

4.3 Electrochemical Impedance Spectroscopy (EIS)

Electrochemical Impedance Spectroscopy (EIS) is used to characterize the recording sites electrical properties. Figure 4.7 (a) shows the impedance measurement setup which consists of a stainless steel rod as the counter electrode, Ag/AgCl electrode (RE-5B, BASi, West Lafayette, IN) as the reference electrode, a 1x phosphate buffered saline (PBS) solution (BP3994, Fisher, Waltham, MA) and the probe. As shown, the counter electrode, reference electrode, and the probe recording site are submerged in the PBS solution and impedance measurements are obtained by applying a 10 mV$_{pk-pk}$ signal from 10 Hz to 50 kHz. Figure 4.7 (b) shows the impedance magnitude and phase values for recording site# 1 at frequencies between 10 Hz and 50 kHz. Figure 4.8 shows the impedance magnitude and phase values for 9 electrode recording sites measured at 1 kHz.

74
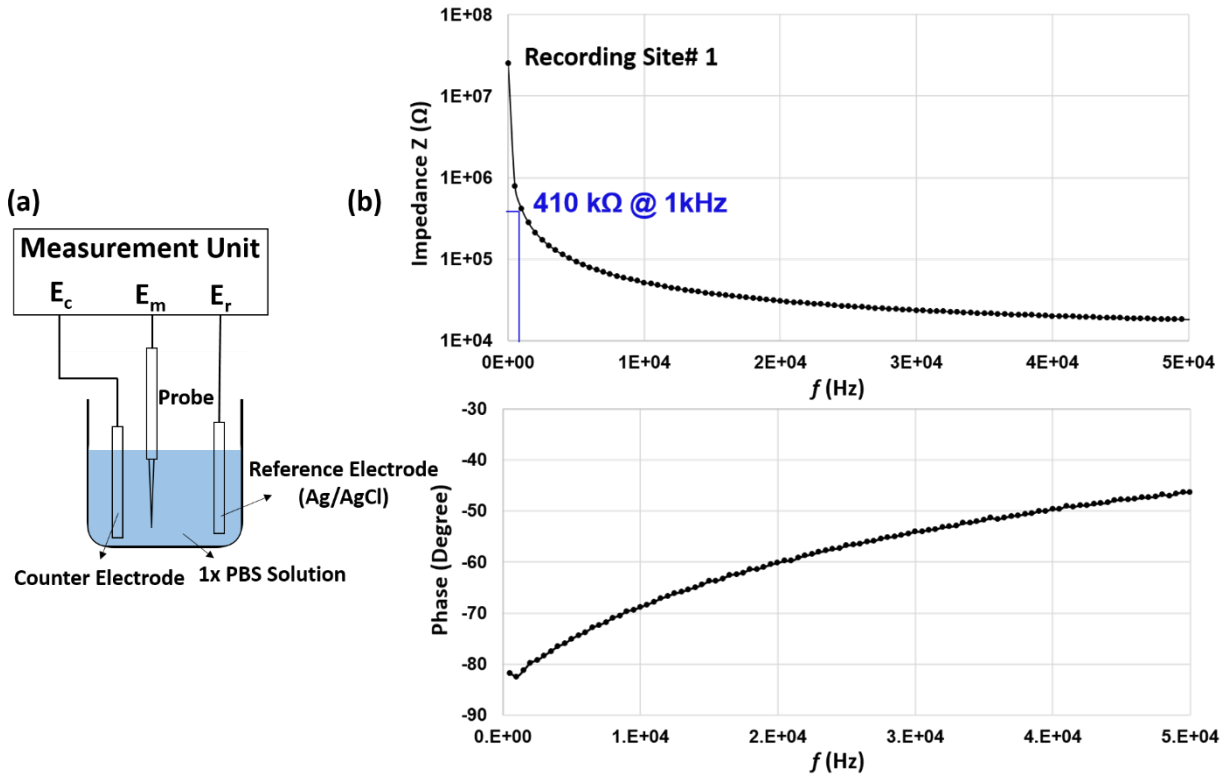
Figure 4.7: Electrode recording site impedance spectroscopy setup and measurement results. (a) EIs setup consists of a counter electrode (stainless steel), reference electrode (Ag/AgCl), 1x PBS solution, a measurement unit and the electrode. (b) Impedance measurement results (amplitude and phase) of one of the recording sites which is measured to be 410 kΩ at 1 kHz.
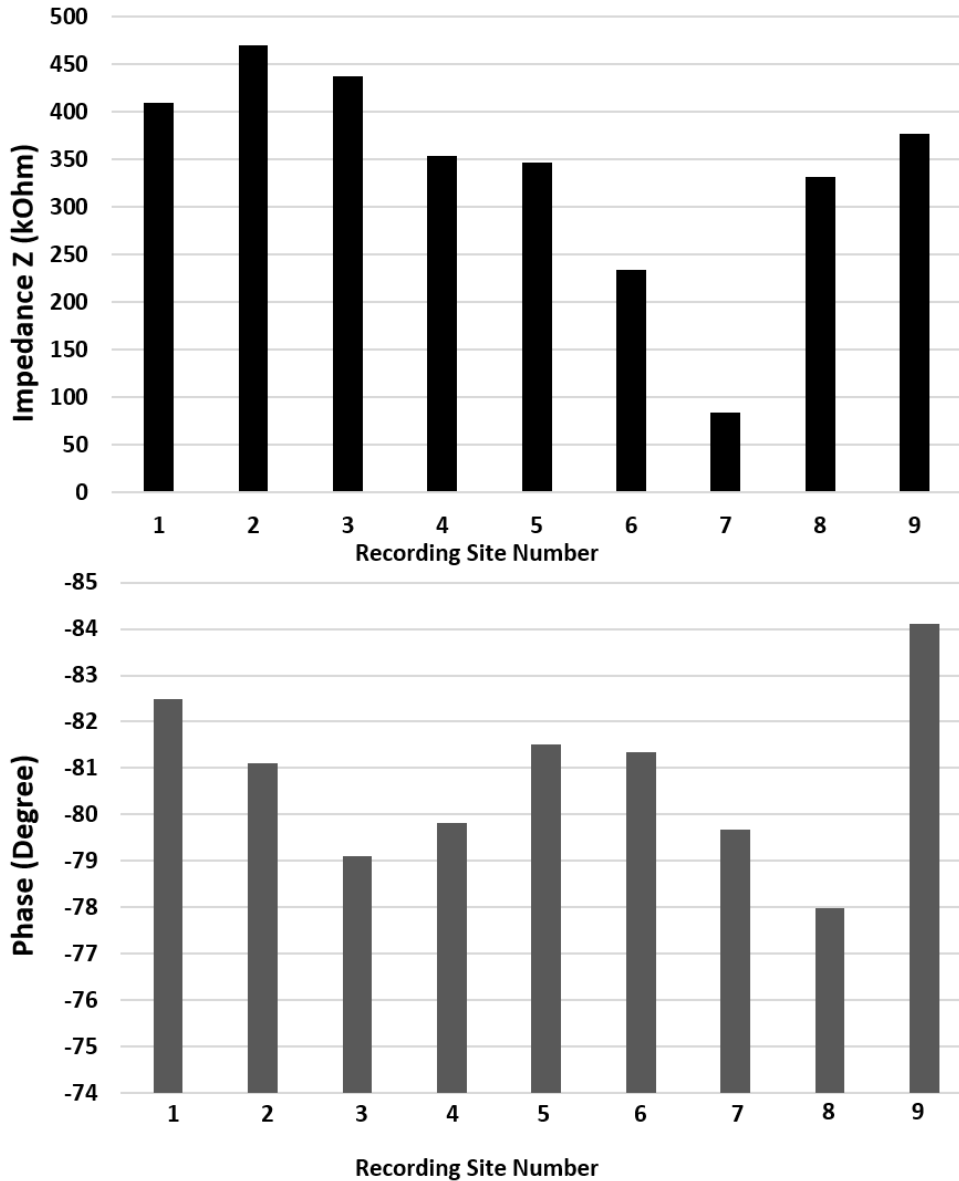
Figure 4.8: EIS measurement results (impedance magnitude and phase) for 9 electrodes recording sites measured at 1 kHz.

4.4 Mechanical Characterization of the Electrodes

Mechanical robustness and flexibility of the electrodes is tested by applying a bending force at the tip of the electrodes using a micromanipulator probe tip under the probe station microscope. Figure 4.9 shows the electrode before and during application of the bending force at the electrode tips. As shown, the electrode can bend for ~28° with ~115 μm lateral displacement at the tip before

breakage. The breakage ultimately occurs at the junction of the conical tip and cylindrical base as expected (Fig. 4.9C). As shown in Figure 4.10, a neck is formed at the junction that reduces mechanical robustness as a structural weak point. Although the bending test reveals the electrode's excellent flexibility and robustness, eliminating the neck and other weak points such as undesired shifts along the shank due to wafer bonding misalignment (Fig. 4.10C) can further improve electrode mechanical robustness which is critical for successful implantation and long-term *in vivo* stability post-implantation. In the next chapter we will discuss in detail how the necking and undesired shifts are formed and we propose solutions to eliminate or mitigate these issues.
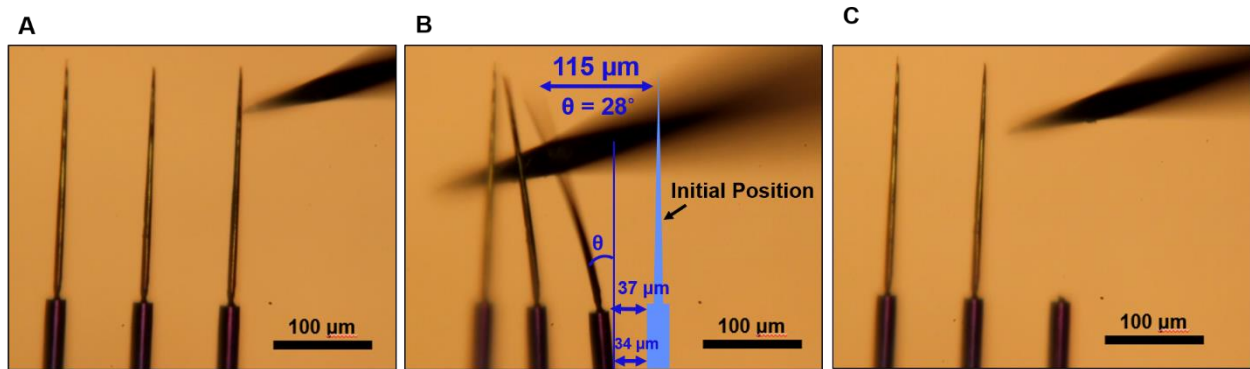
Figure 4.9: Mechanical characterization of electrodes using a bending test: Robustness and flexibility of electrodes is tested by applying a bending force at the electrode tips using probe station tips. (A) Electrodes before applying the force, (B) Electrodes maximum bending and lateral displacement right before breakage, the electrode tip is bent ~ 28° and displaced ~ 115 µm laterally before breakage occurs. (C) The breakage occurs at the junction of the tip conical part and cylindrical base (the most right electrode).
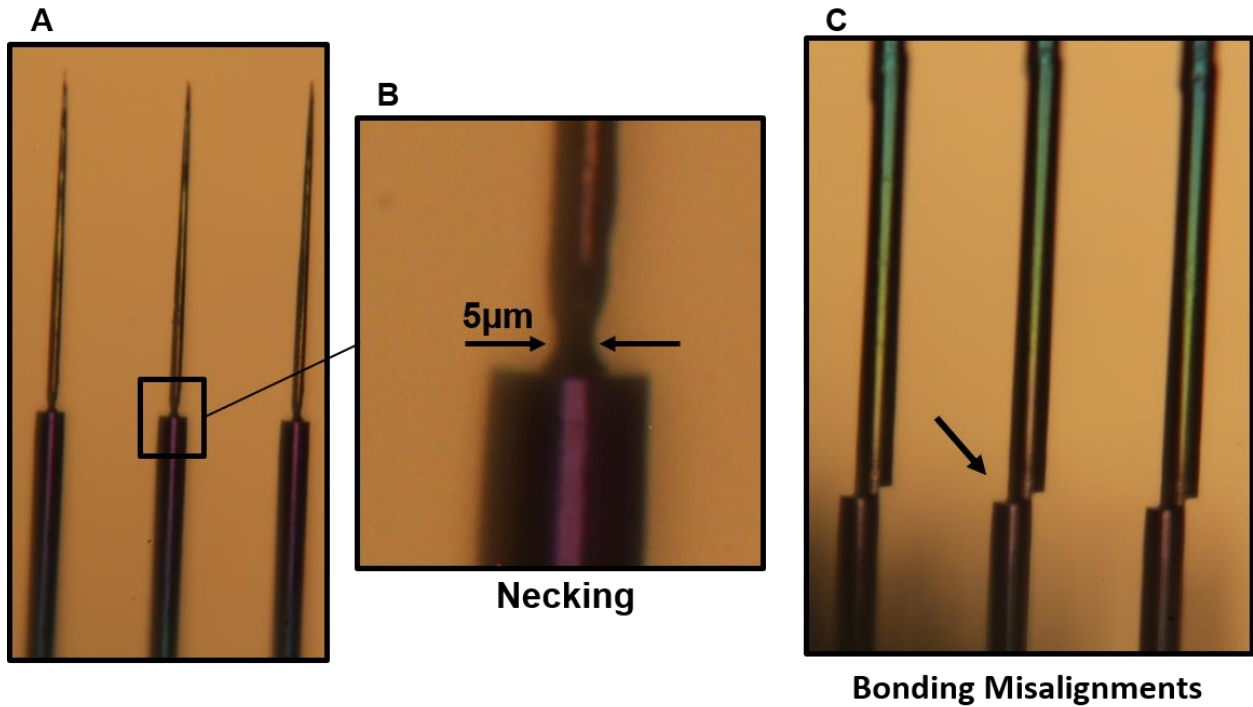
Figure 4.10: Electrodes structural weak points: (B) Necking at the junction of the conical tip and cylindrical base and (C) undesired shifts align the electrode shank due to wafer binding misalignment make the electrodes more susceptible to bending, buckling and breakage during implantation and post-implantation.

4.5 Acute *in vivo* Studies

The first step to perform acute studies is to make electrical interconnections between the electrodes and the external recording equipment. We used arrays with low electrode-count (<100 electrodes) and large pitch size (100µm-500µm) and millimeter-long shanks (1mm-1.5mm) for acute studies. We have devised a provisional method to make interconnections as shown in Figure 4.11. In this approach, the array is placed in a jig upside down to protect the electrode shanks from breakage during the interconnection process. Next, the electrode pads are wire bonded to the PC board pads using a wedge-bonder machine. To insulate the wires and enhance the flexibility and robustness, epoxy is applied to the wires to form a highly flexible insulated wire-bundle.
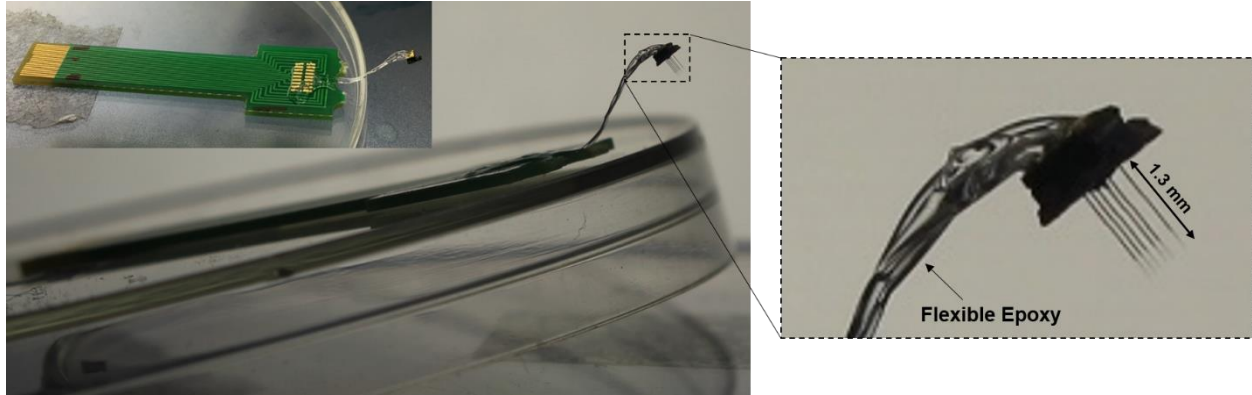
Figure 4.11: Electrical interconnection method: Electrodes pads are connected to a PC board using wire bonding. To insulate the wires and enhance the flexibility and robustness, an epoxy will be applied to the wires to form a highly flexible insulated wire-bundle.

Upon incorporating the interconnections, the device is ready for acute *in vivo* studies. We have used the electrodes with lower site impedances for *in vivo* recording. Acute studies are performed on mice/rats under anesthesia. Immunohistology data will be used to assess the acute tissue damage. The *in vivo* recordings and immunohistology studies are carried out in collaboration with Professor Ahmed's group at the University of Michigan, (Department of Psychology, Biopsychology division).

The SEA arrays manufactured using the microfabrication process described in section 3.2.2. 2×2 and 3×3 arrays of millimeter-long electrodes were implanted in a rat brain under anesthesia. The site impedance of the probes (the sites were located just below the tip), was in the range of a few hundred kOhms at 1 kHz as shown in Figure 4.8. The sharpness of the probes ensured an extremely straightforward insertion (Figure 4.12A). After recordings, the probes consistently remained fully intact (Figure 4.12B), indicating their stiffness despite their narrow, small footprint. Recordings under isoflurane anesthesia showed characteristic slow field potentials, along with occasional epochs of 11 Hz oscillations (Figure 4.12C, 12D) that have been recently reported in recordings

under isoflurane [95]. Thus, we have already performed the first series of implants to establish that the probes are viable, easy to insert, resistant to breakage, and able to record electrical signals. An acute histology study is done to investigate the electrodes insertion profile in the depth of the tissue. Electrode shanks are first coated with Fast DiI prior to insertion. Shanks remained in brain for 3.5 hours under isoflurane anesthesia, followed immediately by perfusion. DAPI is used as the counterstain and sections are 40 μm thick. Figure 4.13 shows the histology results confirming the penetration through the white matter with no bending or deviation.
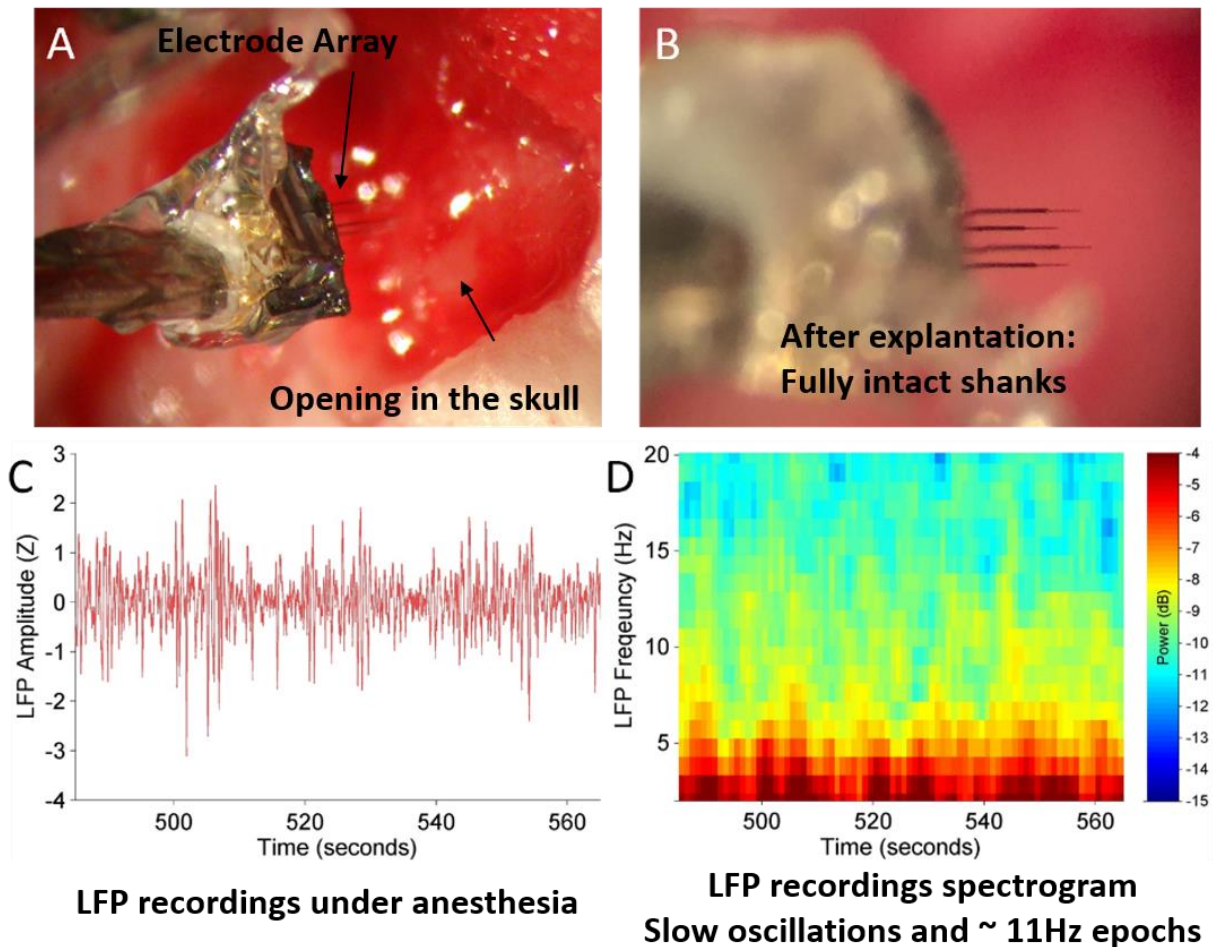
Figure 4.12: Acute recordings using the SEA array *in vivo*: (A) An image of a prototype SEA array during implantation into rodent brain. The array was able to seamlessly penetrate brain tissue thanks to the sharp needle design of the probes. (B) Image of SEA array after removal from the brain showing fully intact probes. (C) LFP recordings in a rat barrel field cortex under isoflurane

anesthesia recorded on one of the channels of the SEA arrays. (D) Spectrogram of the LFP recordings showing characteristic slow oscillations and ~ 11 Hz epochs that are both hallmarks of LFP under isoflurane anesthesia, demonstrating the ability of these probes to record high-quality neural signals.
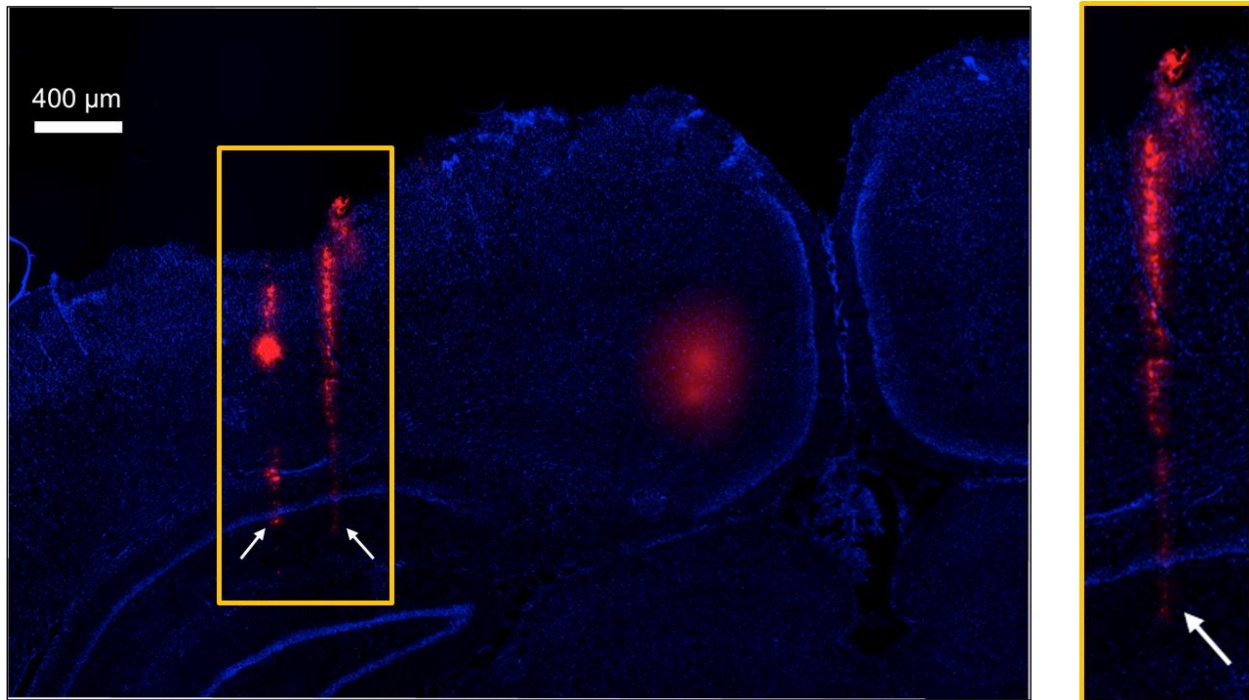
Figure 4.13: Acute histology results: The insertion profile of two electrode shanks of a 2×2 SEA array shows successful penetration through the white matter with no bending or deviation.

4.6 Conclusions

The Sea of Electrodes Array (SEA) technology fabrication, characterization and in vivo experiments are presented. These include:

- First generation SEA arrays: Arrays of 32×32, 50×50, and 72×72 electrodes with diameters of 15-35 μm, maximum length of 500 μm and spacing of 50-100 μm.

- Second generation SEA devices: Arrays of 2×2, 3×3, and 10×10 electrodes of 1.2 mm long, 10-20 μm, and spacing of 100-500 μm with functional recording sites.

- Electrochemical impedance spectroscopy (EIS) characterization of 2nd generation SEA devices showed an average impedance site of ~410 kΩ, however, recording sites impedance exhibited high variation among electrodes of the same array and arrays of the same batch. Further research is required to resolve the reliability and repeatability issue of the site formation step to obtain highly stable sites with proper impedance for long-term in vivo single unit recording applications.

- Acute in vivo studies are performed to show the electrodes robustness, insertion, and recording functionality by LFP recordings in a rat barrel field cortex under anesthesia using 2×2 and 3×3 arrays. Acute histology results showed successful penetration of electrodes in the white matter without shank bending or deviation.

In the next chapter, the SEA technology innovative features, potential capabilities and limitations are discussed.

Chapter 5: SEA Technology Features, Limitations and Potentials

5.1 Overview of the Innovative Features

The broad goal of this research has been to develop a new class of extremely dense, high-count, and versatile multi-mode and multi-functional electrode arrays for interfacing with neural structures through electrical, optical, and chemical means.

From a technology standpoint, the SEA technology design, fabrication, and structure are all novel and significantly different from current technologies. As explained in the previous chapters, many different kinds of multi-channel electrodes are available today, utilizing different fabrication technologies. One can categorize these fabrication technologies into two broad classes. One utilizes assembly and manipulation of individual electrodes (such as carbon fibers or microwire bundles), and the other relies on planar microfabrication technologies, such as those used for semiconductor electronics fabrication. Our approach allows us to combine the best features of both of these approaches. We can produce a very dense and high-count array of fine and slender insulated silicon needles with variable length and width, a tapered cross-sectional shape along their length, and sharp tips. Furthermore, the proposed new fabrication approach also allows each needle to have a recording/stimulating site near its tip, incorporate a waveguide within its core for optical transmission, and incorporate a fluidic channel that could be utilized for constructing chemical sensors. In addition, the technology allows the formation of tightly-spaced clusters of several extremely fine needles whose tips are at different heights, much like a tetrode, but with

much better-defined dimensions and feature sizes. Figure 5.1 illustrates the innovative features of the micro-electrodes that can be fabricated using the proposed technology. These features include:

1- Individual needles can have different lengths, and still reside side by side, and can be distributed in any arbitrary pattern. Needles as tall as several millimeters can be fabricated as needed in many applications.

2- Needles can have variable pitch/density, with needles capable of being spaced as close as 10μm.

3- Needles can have different shank diameters, which helps in engineering the stiffness of each shank. Shanks as small as a few microns in diameter can be fabricated. Obviously, there is a tradeoff between stiffness and flexibility, which can be tailored for different applications by the user.

4- Several needles with extremely small diameters can be fabricated in even closer proximity than typical needles and form a cluster, like a tetrode, to monitor neural activity in depth within the same column of tissue.

5- Although not shown in this figure, each needle can also function as an optical fiber and include a recording/stimulation site at its tip, thus enabling multi-mode function, allowing optical and electrical interface with neurons in the vicinity of the tip.

6- Finally, the needle can be hollow to form a micropipette. This micropipette can be instrumented for chemical sensing.

In the following sections, we will discuss the details of the unique features, potential capabilities, limitations and shortcomings of the developed SEA technology.
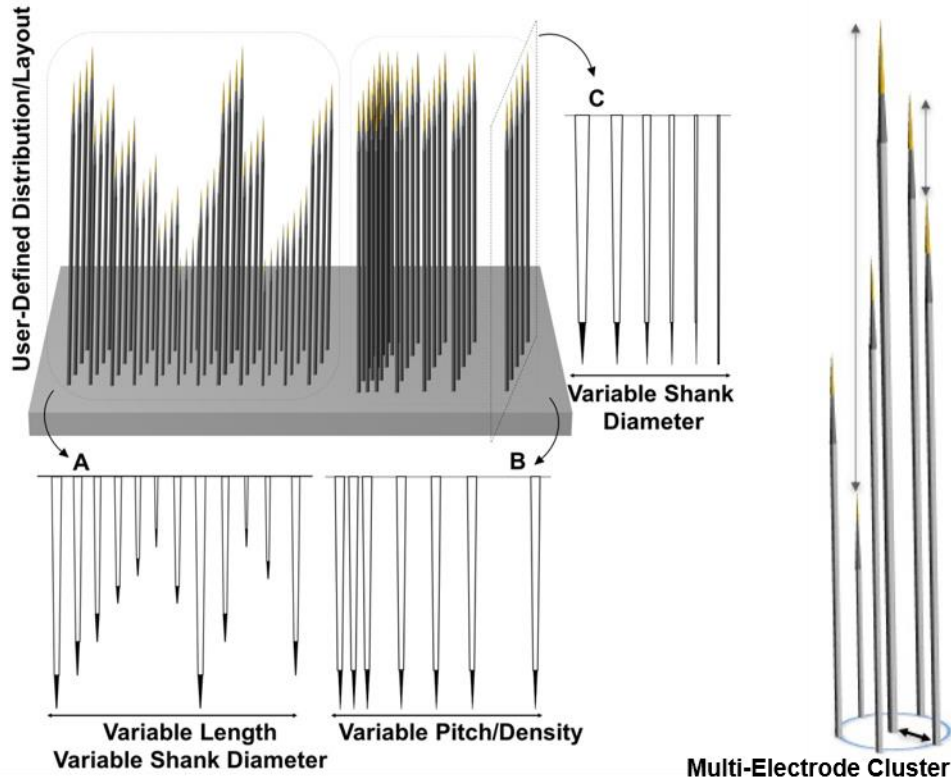
Figure 5.1: Innovative features of the proposed micro-needles: 1- Individual needles can have different lengths, and still reside side by side, can be distributed in any arbitrary pattern. Needles can be as tall as several millimeters. 2- Needles can have variable pitch/density, capable of being spaced as close as 10 μm. 3- Needles can have different shank diameters, to allow design of the stiffness of each shank. Shanks with diameters as small as a few microns can be fabricated. 4- A cluster of closely spaced needles with different heights will allow depth recording.

5.1.1 Probe Shank Conical Shape and Tip Sharpness

The conical shape of the shanks and tips shown above is naturally obtained through a special feature of the DRIE etch step called DRIE lag effect. DRIE etch rate is inversely proportional to the aspect ratio of the hole/trench, in other words, holes/trenches with higher ratio of depth to width are etched slower [96-102]. The variable etch rate at different depths will result in the conical shape of the shank, producing a sharp tip which improves probe insertion into the tissue. Figure 5.2 shows three sets of electrode arrays fabricated with different starting hole sizes (15, 25, and 35 μm) resulting in shanks with different sizes and conical shape. Figure 5.3 shows SEM images of

85

electrodes with various tips size and shape which is controlled by changing the opening hole diameter. As shown in Figure 5.2 and 5.3, holes with smaller diameters result in tips with smaller size and smaller opening angle and therefore increased sharpness.
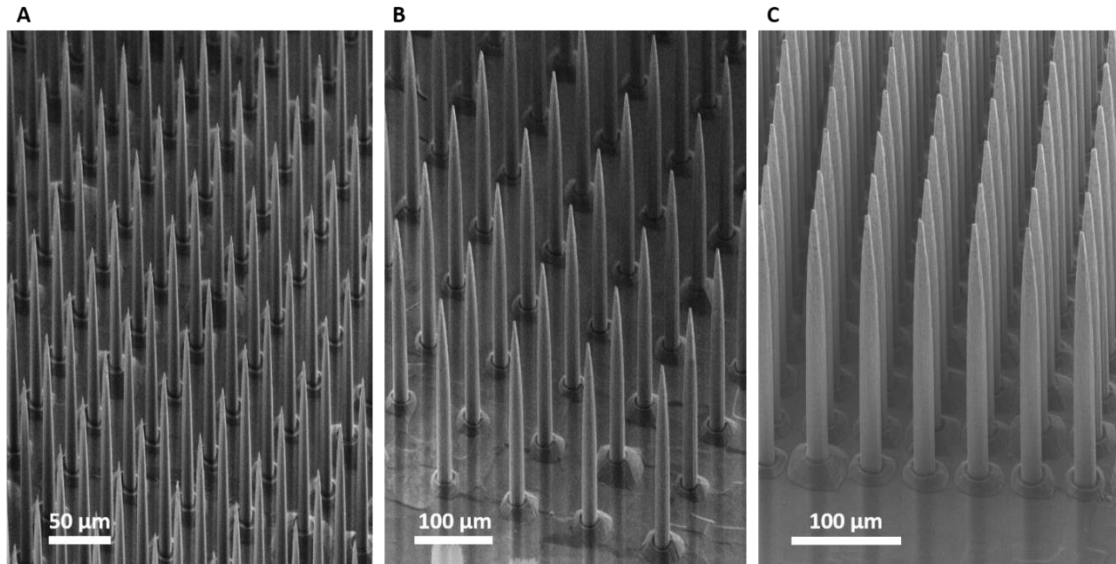
Figure 5.2: Fabricated electrode arrays using starting holes with different diameters: (A) ~10 um (B) ~20 um (C) ~30 um thick probe shanks resulted from 15 um, 25 um and 35 um hole diameter respectively.
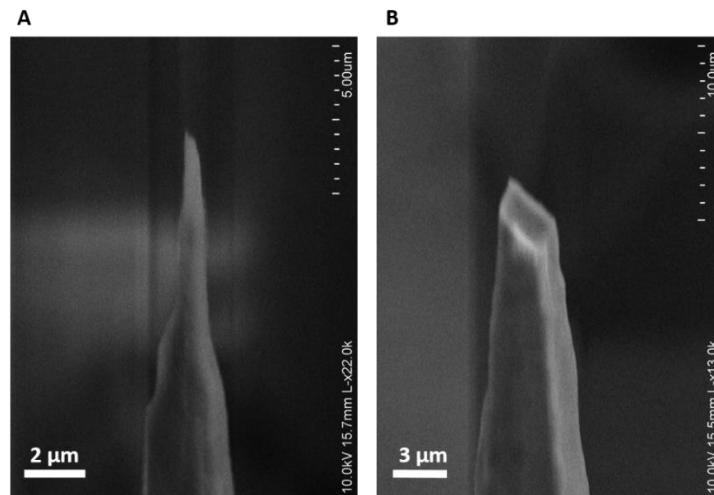
Figure 5.3: SEM images of the submicron size electrode tips: (a) 10 um thick, (b) 20 um thick electrode shank, sharp tips and small probe shank size reduces the tissue damage during the implantation and post-implantation, improves the chronic stability and increases the array density.

5.1.2 Varying Electrode Length, Size, Pitch and Distribution

There are several aspects of this fabrication technology that are critical for successful recording and manipulation of neurons across multiple spatial latitudinal and longitudinal planes with high spatial resolution. First, the length of side-by-side electrodes can be varied using two methods:

1- DRIE lag approach: By changing the hole diameters in the layout, due to the DRIE aspect-ratio dependent etching (ARDE) and DRIE lag effect in holes with various depth, and electrodes with various lengths as shown in Figure 5.4 can be produced.

2- Wafer bonding approach: By engineering the mask layouts used for patterning the holes in each wafer, the length of side-by-side electrodes within a die can be controlled as illustrated in Figure 5.5.

In the first technique (DRIE lag approach), reducing the holes opening size results in reduced transport of the DRIE process etchant agents and ion bombardment at the bottom of the features as the aspect-ratio increases throughout the deep etching process. This will cause reduced etch rate, tapering and convergence of the holes sidewalls, and eventually termination of the etch process. We have utilized this self-terminating process to obtain side-by-side electrodes with different heights (lengths) using holes with various opening diameters in a single process as shown in Figure 5.4. Using this technique, the maximum variation of length is limited to 500 μm for reasonable hole diameters (<35 μm). To extend the range of electrodes length, another technique based on wafer bonding is developed as described in the following.

In the second technique described schematically in Figure 5.5, electrodes length is dependent on the hole layout design in each substrate of the bonded stack. In other words, larger holes (20-35 μm) are replaced by small holes (<10 μm) to form a conical tapered hole instead of thru-wafer

87

holes with straight sidewalls. Depending on the substrates thickness and the relative position of hole sizes reduction along the bonded substrates stack, the final depth of the holes and therefore final electrode shank length is determined.

The electrode pitch can be locally modified within the array, in other words the density of recording sites can be customized based on the application by changing the layout. Studies have shown that the electrode size plays an important role in determining tissue damage and chronic stability of the implanted array [103]. Any arbitrary distribution of electrodes with various length, shank diameter and pitch across the array is obtained. Optical and SEM images show the fabricated array with all the features mentioned above (Figure 5.4). Employing the mentioned features (varying side-by-side electrode length, pitch, and distribution) will enable 3D access of neurons with extremely high spatial resolution. In particular the varying length feature is critical in implantation into the brain convoluted surface and simultaneous recording/stimulation of neurons at various depth of tissue.
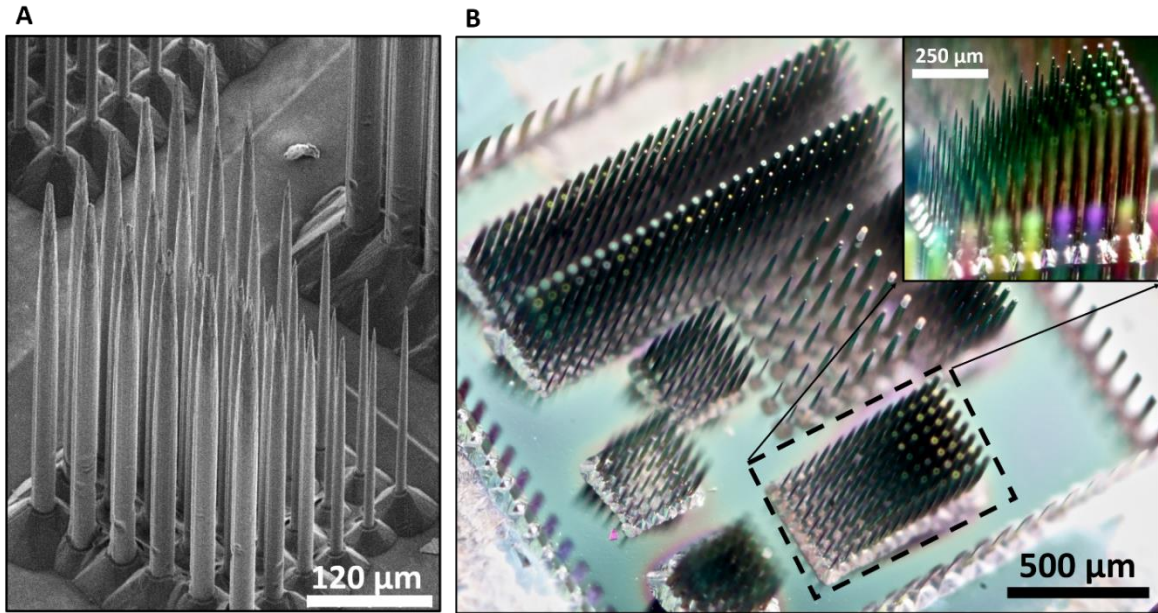
Figure 5.4: Arrays with various electrode length, thickness, pitch and distribution is realized using the refilling technology. These features enable recording and stimulation of larger number of neurons in the implanted tissue volume using minimum number of electrodes resulting in less tissue damage and improved chronic stability. (A) SEM image of fabricated side-by-side electrodes with varying length and diameter. (B) Optical image of an array with an arbitrary distribution of electrodes with various length, shank diameter and pitch.
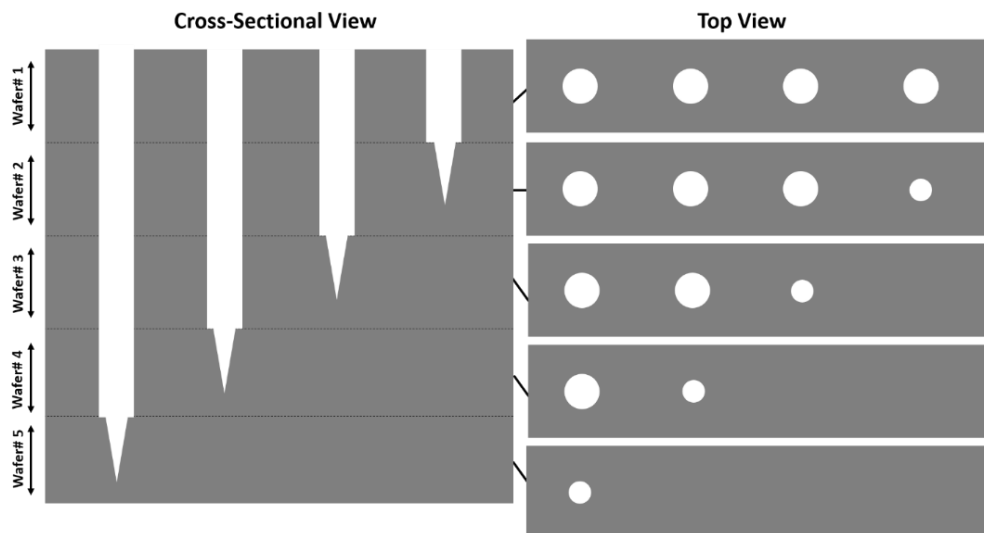
Figure 5.5: Realization of electrodes with various side-by-side lengths in steps of silicon wafer thickness. As shown in the right, the layout design in each wafer determines the final electrode shank length.

5.1.3 Integrated Multi-Modal Needles for Optical or Chemical Interfaces

Optical interaction with neurons has attracted much attention recently. In this approach light is used to study the neurons that have been genetically modified to demonstrate light-sensitive behaviors [104]. Therefore, it is desirable to guide light to the neurons in cellular and subcellular resolution by means of the neural probes. An important feature of the proposed technology and structure is the flexibility over the usage of materials that can be used to refill the holes/trenches. Optical fiber cladding and core can be formed by using materials with different refractive index in the refilling stack. Light waveguides can be easily formed by using popular microfabrication materials such as LPCVD oxide (SiO_2) and oxynitride (SiON) layer to add optical recording and stimulation and optogenetics functionality to the probe array. Figure 5.6A schematically depicts the waveguide concept which is based on the total internal reflection of light occurring at the interface of two materials with different refractive indexes. Figure 5.6B shows the realization of waveguides for optogenetics applications, using the fabrication technology described earlier with some minor modifications to the deposited materials.
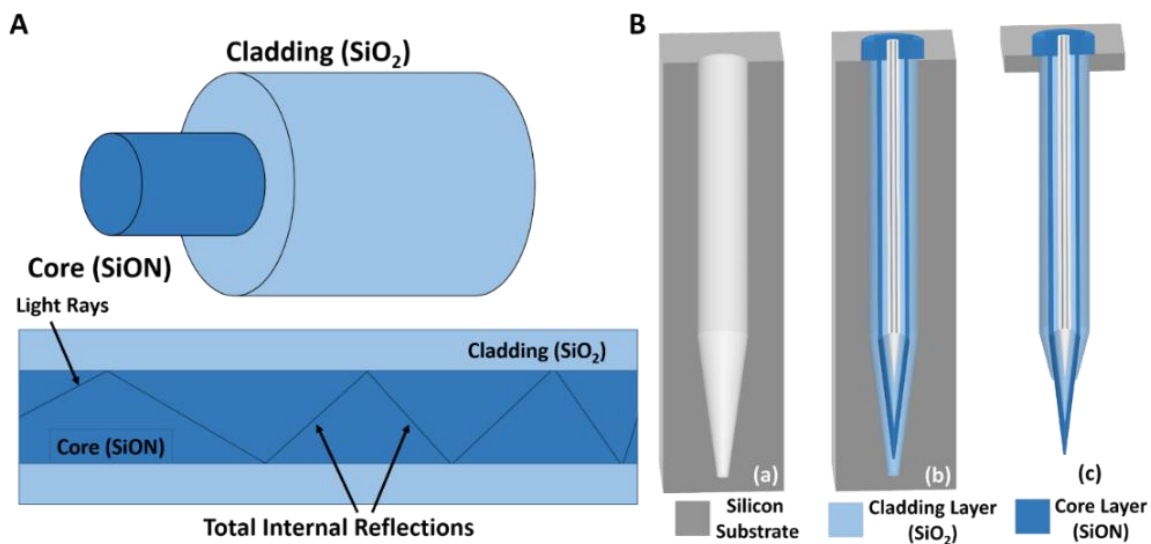
Figure 5.6: Formation of optical probes for optogenetics applications. (A) Optical waveguide consists of a core with different refractive index than the surrounding layer (cladding). Total internal reflections at the interface of the core and cladding layers guide light to the tip. This can be used to locally record/stimulate the neuron activities, (B) Optical electrodes can be fabricated using the same process flow described in Figure 3.1 by refilling the holes with materials having different refractive indexes, e.g. SiON and SiO_2.

In addition to the possibility of including optical guiding capability within the core of a single needle, some needles can also potentially be instrumented to function as chemical sensors. Drug delivery and chemical stimulation of the neurons are of great interest [105]. A microfluidic channel can be integrated in the existing design by forming an opening at the tip of the needles. As shown in Figure 5.7, if the hole diameter exceeds twice the deposited refilling layer thickness, the hole will not be refilled completely and will leave a channel in the center of the needle hole, which can be employed as the microfluidic port for drug delivery and chemical sensing. As shown in Figure 5.7, the fabrication process flow is the same as the one described in Figure 3.1 with an additional RIE etching of the needle tip as the last step to make an opening at the tip which forms a connection to the needle inner hollow. These hollow needles can be alternatively filled with appropriate solid polymeric electrolytes, similar to micropipette chemical sensing, to form chemical sensing electrodes. Although this is not the focus of this research, it is mentioned to indicate the potential that these needle arrays offer as a multi-functional interface to the tissue.
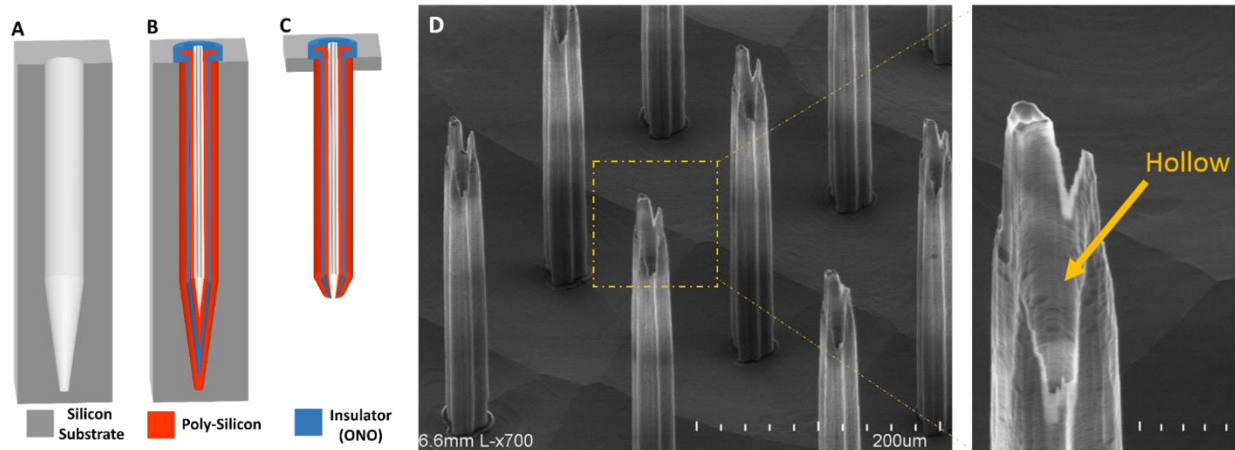
Fig. 5.7: Integration of microfluidic channel within the probe shank for drug delivery and chemical stimulation purposes: As shown the fabrication process flow is the same as the one described in Figure 3.1 with and additional RIE etching of the needle tip as the last step to make an opening at the tip which forms a connection to the needle inner hollow. The microfluidic channel can also be obtained by layout engineering as shown in the SEM image.

5.1.4 Multi-Electrode Clusters

Since the fabrication technology described in Figure 3.1 utilizes DRIE lag and ARDE effects, it is feasible to form multiple recording sites in a small area, which greatly increases the density of recording/stimulation sites per implanted volume. The concept of multi-electrode cluster probe arrays is conceptually depicted in Figure 5.8. As shown, holes with different opening areas are closely laid out, and the difference in opening areas results in various etch depths of the silicon substrate due to DRIE Aspect-Ratio Dependent Etching (ARDE) effect. After DRIE, the fabrication process is continued as described in Figure 3.1. At the end, a multi-electrode set of needles is formed with recording/stimulation sites created at the tip of each needle as shown in Figure 5.8. The number of recording sites per cluster is determined by the number of holes that are laid out along the perimeter of the main shank. In approach 1, the holes around the main shank can be laid out to be separated by solid silicon walls. In the second approach, holes can be connected to the main shank through a narrow channel to increase the DRIE etch depth by reducing the ARDE

effects. To ensure the channel is fully refilled by the sacrificial polysilicon layer, the channel width

should be narrow (<7 µm), otherwise the sites formed around the main shank will be electrically

shorted.
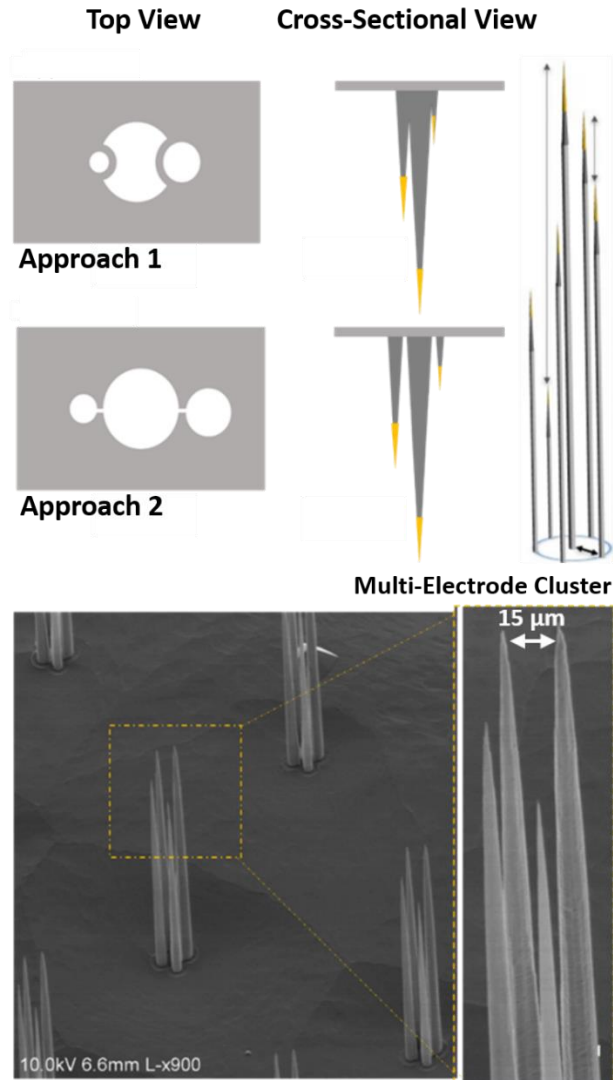
Figure 5.8: Realization of multi-site per shank using DRIE ARDE effect: Approach 1: holes with different openings are laid out around the perimeter of the main shank isolated with substrate silicon walls, sharp tips will form at various depths due to ARDE nature of DRIE. Approach 2: holes are connected to the main shank through a narrow (<7um) channel to increase the DRIE etch rate, the channel width is narrow enough to be fully refilled by the sacrificial polysilicon LPCVD and therefore provides isolation of the sites formed around the main shanks. SEM images show the fabricated multi-site (4 sites) per shank electrode using the approach described above. Electrode tips sizes are sub-micron and the shank diameter at the base is ~15 um.

5.2 SEA Technology Limitations:

In this section we will discuss some of the challenges and limitations of the SEA technology. These limitations include LPCVD deposition inside ultra-deep ultra-high-aspect-ratio features, wafer bonding misalignment when making long shanks, structural weak points (necking) and tissue damage when the number and density of shanks increases.

5.2.1 LPCVD Refilling Limitations

As mentioned in the description of the microfabrication process, Low Pressure Chemical Vapor Deposition (LPCVD) is used to refill the ultra-deep ultra-high aspect-ratio holes. LPCVD provides uniformity and coverage superior to that of other CVD methods such as Atmospheric-Pressure CVD (APCVD), Plasma-Enhanced CVD (PECVD) or physical deposition methods such as evaporation and sputtering [106]. Coverage is defined as the ratio of thickness of deposited film on the bottom of the etched feature to the film thickness at the surface as shown in Figure 5.9.
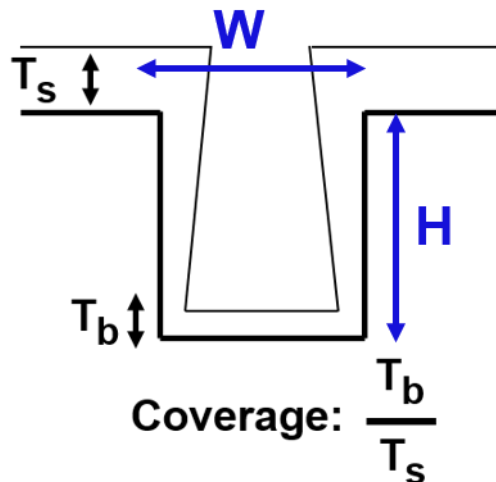
Figure 5.9: Deposition coverage is defined as the ratio of film thicknesses deposited on the bottom of the etched feature to the one deposited at the surface.

94

Experimental results and theoretical modeling have shown that the coverage degrades by increasing the feature aspect ratio [107]. In this section, we present a theoretical calculation to predict the limitation of LPCVD in refilling holes and trenches with various aspect ratios. Komiyama et al. have developed a theoretical model for CVD processes to study parameters such as coverage and surface sticking probability.

For a cylindrical hole with depth of H and diameter of W, and for sufficiently large aspect ratios (H/W), the deposition process inside the hole can be assumed a one-dimensional approximation governed by the following equations and boundary conditions [108]:

$$D\frac{d^2C}{dz^2} - \frac{S}{V}k_sC = 0 \tag{5.1}$$

$$D\frac{dC}{dz} = k_sC \text{ at } z = 0 \qquad \text{(boundary condition 1)}$$

$$C = C_0 \text{ at } z = H \qquad \text{(boundary condition 2)}$$

Where D is the coefficient of the precursors, C is the concentration of the gas-phase components, k_s is the surface reaction rate constant, and S, V are the surface area and volume of a hole/trench, respectively with the following analytical solution:

$$\frac{C}{C_0} = \frac{\cosh\left(\frac{z}{H}\phi\right) + \frac{2W}{H\phi}\sinh(\frac{z}{H}\phi)}{\cosh\phi + \frac{2W}{H\phi}\sinh\phi} \tag{5.2}$$

$$\phi = H\sqrt{\frac{S}{V}\frac{k_s}{D}} \tag{5.3}$$

For a high-aspect ratio etched feature (large H/W), the S/V ratio is 4/W for a cylindrical hole and 2/W for a trench. As the Knudsen diffusion dominates in a high aspect ratio micro hole/trench we will have:

$D = \frac{1}{3}Wv$ where v is the thermal velocity of a growth species molecule

$k_s = \frac{1}{4}v\eta$ based on Herz-Knudsen equation, where η is the sticking probability of the species

Therefore:

$$\phi = \frac{H}{W}\sqrt{\frac{3\eta}{2}} \quad \text{for a high aspect ratio trench,} \tag{5.4}$$

$$\phi = \frac{H}{W}\sqrt{3\eta} \quad \text{for a high aspect ratio hole,} \tag{5.5}$$

with the following equations for the coverage in hole/trench:

$$\text{Coverage} = \frac{1}{cosh\,\phi + \frac{2W}{H\phi}sinh\,\phi} \tag{5.6}$$

To calculate the coverage for a particular aspect ratio, we need to have the sticking probability value for a specific CVD process. As the sticking probability depends on various process parameters such as temperature, pressure, reacting gas species, etc. we have estimated the sticking probability of the LPCVD process used in our fabrication process based on experimental results.

Figure 5.10 shows the deposited LPCVD Oxide-Nitride-Oxide (ONO) film thicknesses at the junction of the cylindrical and conical parts of the shank. This corresponds to the bottom of the 1.5 mm deep cylindrical hole with a diameter of 22 μm, therefore, the total thickness of the ONO film at the bottom of the 1.5 mm deep hole is around 300 nm while the thickness of the ONO film

deposited on the surface of the silicon wafer is around 1.25 μm. To investigate the limitation of the LPCVD processes used in our technology, we focus on the ONO LPCVD process. Oxide and nitride LPCVD processes have the highest deposition temperature, and therefore the highest sticking coefficient (η), as shown in Figure 5.11 [108]. Therefore, the coverage of the LPCVD ONO films and the inability to refill very deep trenches is the limiting factor in obtaining longer electrodes. Figure 5.12 shows the thickness of the ONO and n-type polysilicon films on the sidewall of a hole. The polysilicon thickness is reduced by 50% while the ONO thickness is reduced by 68% (the polysilicon and ONO film thicknesses deposited on the surface of the wafer are 4 μm and 1.25 μm, respectively.)

From the values of coverage and hole aspect ratio we can calculate the sticking coefficient (η) using the equation (5.5) for the ONO LPCVD process which is calculated to be $\eta = 3.15 \times 10^{-4}$ as H/W = (1.5 mm)/(22 μm) = 68 and step coverage is (300 nm)/(1.25 μm) = 0.24.

Using the above values, we can plot the coverage versus aspect ratio (H/W) as shown in Figure 5.13. As shown in Figure 5.13, the coverage for an aspect ratio of 100 is around 0.1. This means that for a hole with a diameter of 25 μm, the maximum depth of the hole that provides the coverage of at least 10% is around 2.5 mm. This means electrodes with maximum length of ~2.5 mm and ~20 μm diameter (considering the sacrificial layers to reduce the final shank diameter) can be fabricated. Minimum coverage of 10% for ~ 1μm thick LPCVD layers of dielectric is chosen to ensure a minimum thickness of 100 nm at the bottom of the etched features which is required for electrical insulation and protection during the EDP etching step, however, for long-term recording applications, thicker dielectrics of alternative materials with better in vivo stability such as SiC should be considered.

As a comparison, in a trench with the same width (25 μm) an aspect ratio of around 140 yields a step coverage of 0.1 as shown in Figure 5.14. Therefore, the trench depth will be around 3.5 mm. This reduction of the dielectric layer (ONO) thickness as the aspect ratio increases is an issue, since it degrades the electrical insulation of electrodes and affects the longevity of the device in the tissue. Also, insufficient ONO thickness might result in fabrication failure during the EDP etching step in which ONO is employed as a protection etch stop layer. Increasing the holes opening size and/or increasing the deposited layers thickness can be employed to mitigate the LPCVD step coverage issues, however, there is a tradeoff between the larger holes with better LPCVD coverage and the tissue volume displacement induced by the larger electrode shanks.
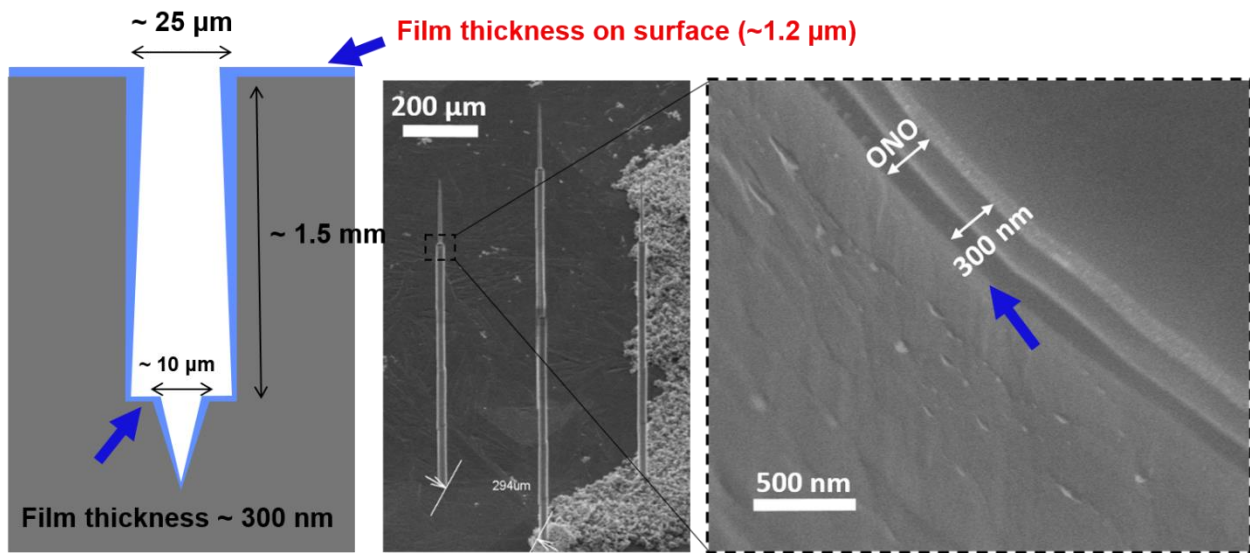
Figure 5.10: Measurement of the ONO layer thickness at the interface of the electrode shank and the conical tip (bottom of the 1.5 mm deep holes) using the SEM images. ONO layer thickness is measured ~300 nm at the bottom of the 1.5 mm deep holes with a diameter of 22 μm, while the surface deposited layer thickness is 1.2 μm.
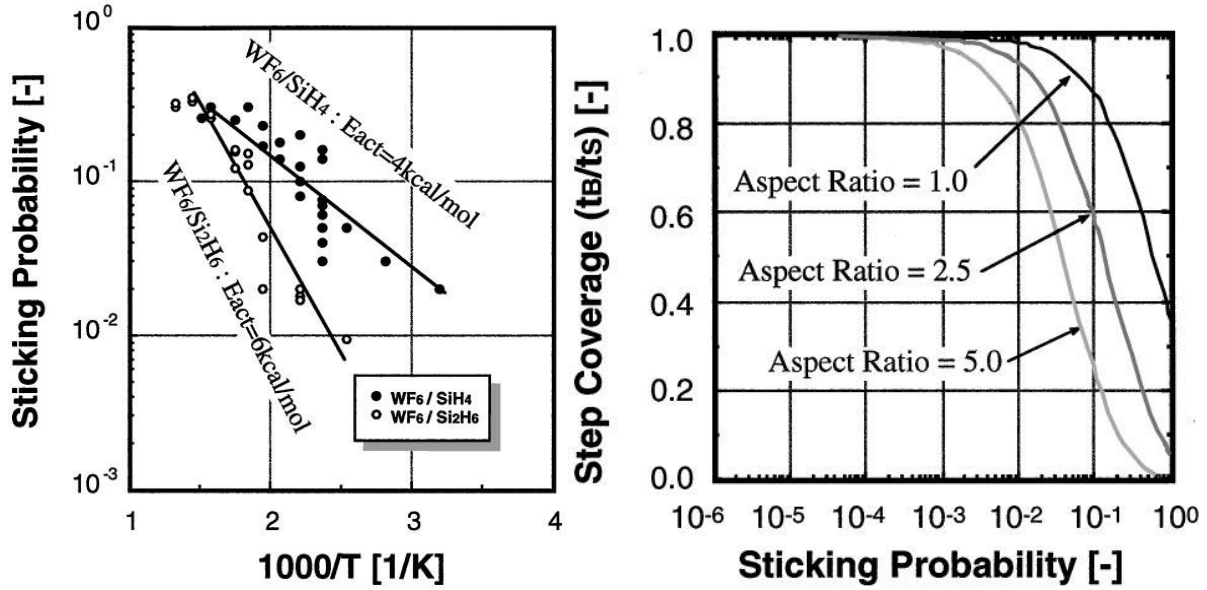
Figure 5.11: LPCVD process dependency on the process temperature and sticking coefficient: Sticking coefficient (η) is increased by increasing the LPCVD process temperature (left) which reduces the deposition step coverage (right) [108].
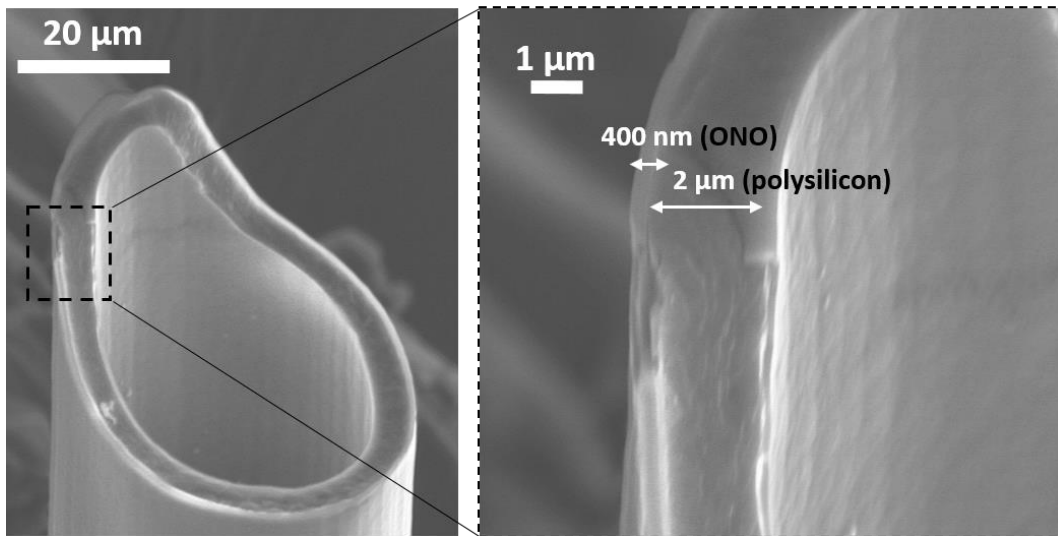
Figure 5.12: SEM images of a broken electrode shank exposing the inner/outer ONO layers and n-type polysilicon. N-type polysilicon layer thickness is measured ~2 μm along the shank while the ONO layer is ~ 400 nm thick.

99
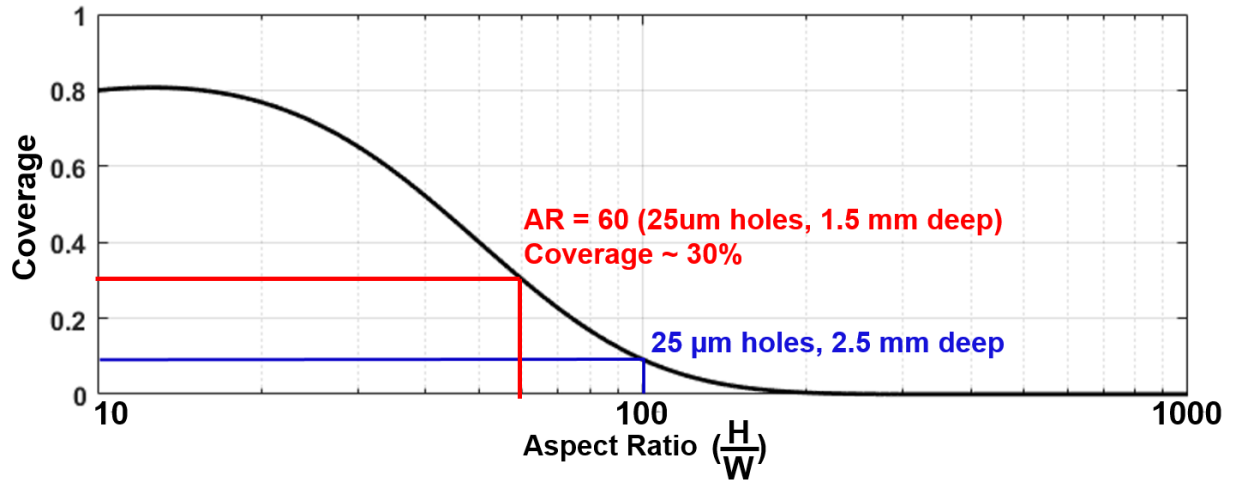
Figure 5.13: LPCVD process coverage of ONO deposition in holes for various aspect ratio values. The coverage is below 10% for aspect ratio of larger than 100.
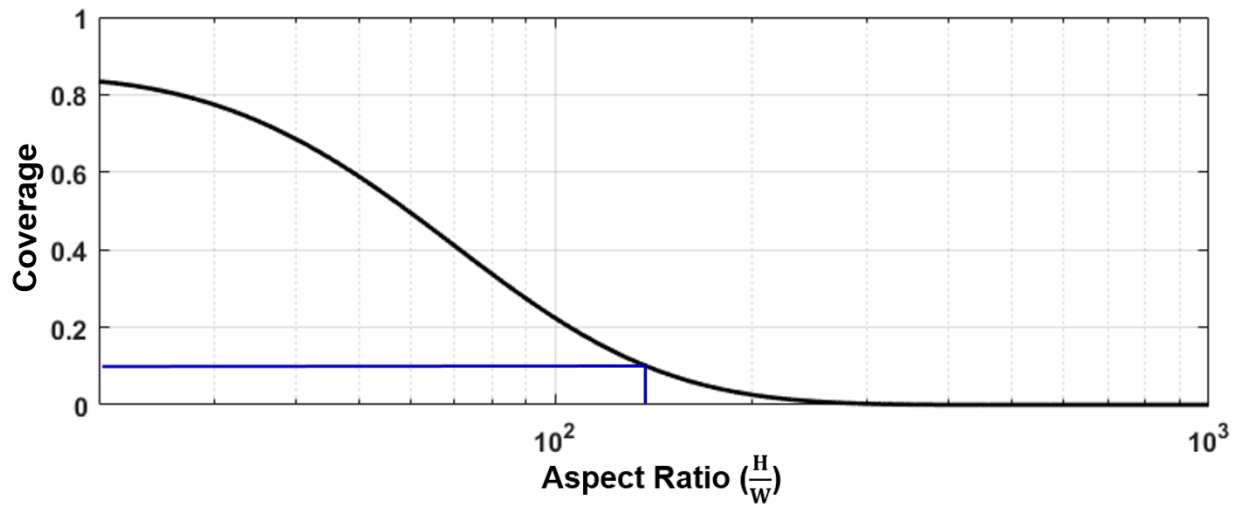
Figure 5.14: LPCVD process coverage of ONO deposition in trenches for various aspect ratio values. The coverage is below 10% for aspect ratio of larger than 140.

5.2.2 Electrodes Structural Weak Points: Wafer Bonding Misalignment

As mentioned in section 3.2.2, increasing the electrode length is achieved by a fabrication process which is based on aligning and bonding multiple wafers. Each wafer bonding step introduces an inevitable misalignment that results in undesired shifts along the electrode length as schematically depicted in Figure 5.15. This results in reduced shank stiffness and lowers the chance of successful penetration into the tissue. Also, for thinner electrodes, the misalignment becomes comparable to the shank diameter and might prevent electrical connection through the conductive core (n-type polysilicon layer) along the electrode shank. Although the bonding misalignment can be minimized to as small as 1 µm or smaller [109], we have observed misalignments as large as 6 µm due to bond aligner tool precision as shown in Figure 5.16. To address the misalignment issues or at least to minimize its adverse effects, we have devised two approaches.
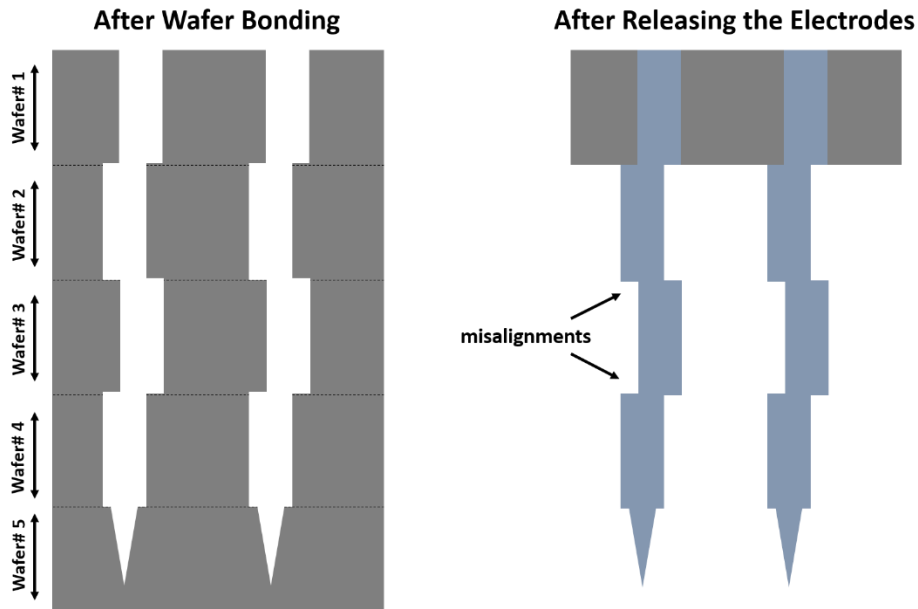
Figure 5.15: Wafer bonding misalignment (left) results in undesired shifts along the electrode shanks (right).
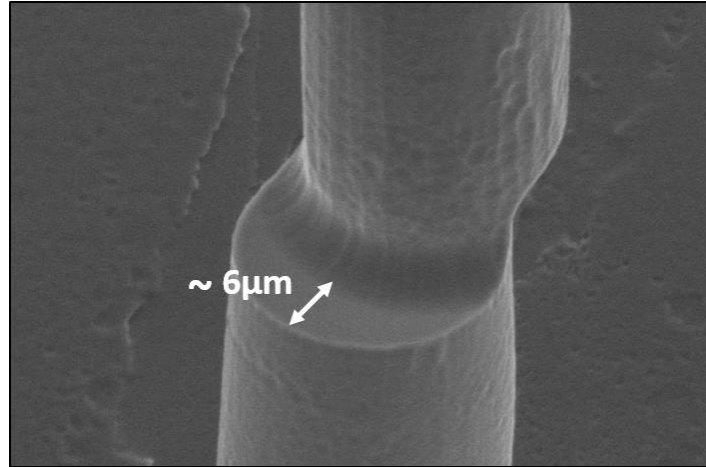
Figure 5.16: Wafer bonding misalignment can be as large as 6 μm in some parts of the wafer.

5.2.2.1 Progressive Electrode Shank Size

As mentioned before, wafer bonding misalignment can result in reduced shank stiffness, increasing the chance of breakage during and post implantation, and/or cause electrode conductive core layer (n-type polysilicon) discontinuity. In order to prevent these failures, the thru-wafer holes diameter can be designed in a way that the difference between adjacent bonded wafers holes radii are larger than the bonding process misalignment, i.e., $(D_k - D_{k-1})/2 >$ misalignment (Figure 5.17). The progressive increase in the hole diameters as shown in Figure 5.17 also provides more mechanical robustness. The drawback of this approach is increased shank thickness along the electrode length which results in more tissue displacement. We have devised another process to reduce the effects of misalignment with no need to increase the shank thickness, as described in the next section.
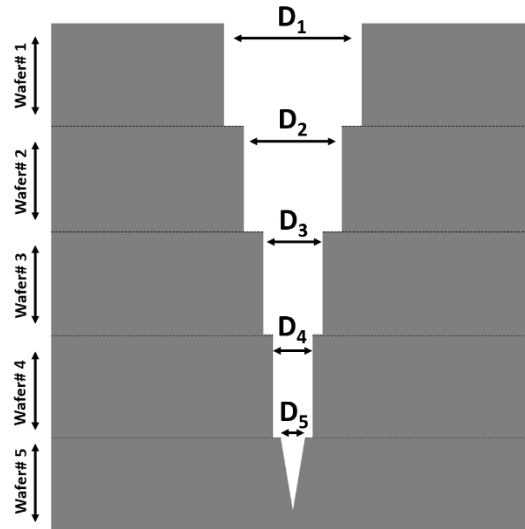
Figure 5.17: Thru-wafer holes diameter is increased progressively in the bonded wafers stack to prevent the issues caused by the wafer bonding misalignment. Adjacent holes radii difference should be larger than the bonding process misalignment, i.e., $(D_k - D_{k-1})/2 >$ misalignment.

5.2.2.2 Bond-then-Align Approach

As shown in Figure 5.16, the misalignment caused by the align-then-bond process can be relatively large (>5µm). Therefore, we have developed a process called "bond-then-align" to circumvent the need for "bond" alignment, as schematically illustrated in Figure 5.18. The process begins with thru-wafer DRIE of one of the wafers (wafer# (n-1)) (Figure 5.18A). Then a blank double-side polished silicon wafer (wafer# n) is bonded to wafer# (n-1) without any alignment process (Figure 5.18B). Next, wafer# n is patterned using backside "pattern" alignment (not "bond" alignment) with wafer# (n-1) backside alignment mark. Therefore, instead of using "bond" alignment which causes large misalignment (>5µm), a lithographic patterning backside alignment is used which has smaller misalignment (<3µm). Steps B and C are repeated as many times needed to obtain the desired thru-wafer holes depth.
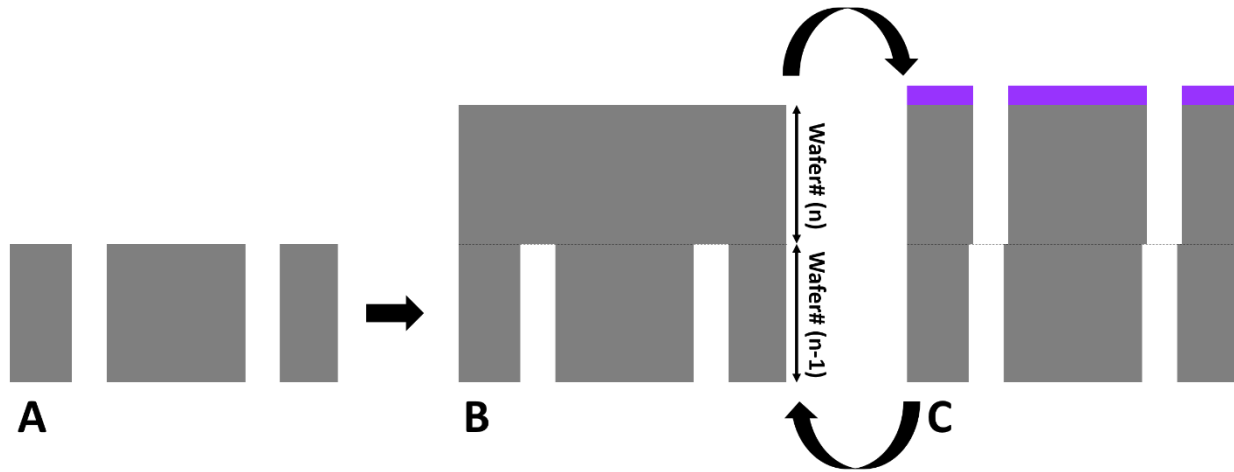
Figure 5.18: "Bond-then-Align" process: (A) thru-wafer DRIE is performed on one of the wafers (wafer# (n-1)), (B) then the next wafer (wafer# n) is bonded to the wafer# (n-1) without any alignment process. (C) Wafer# n is patterned using the wafer# (n-1) backside alignment marks.

5.2.3 Electrodes Structural Weak Points: Necking at the Bonding Junctions

As mentioned in section 4.4, in the millimeter-long electrodes a neck is formed at the junction of conical tip part and the cylindrical shank base. This is due to the degraded LPCVD deposition conformality as shown schematically in Figure 5.19, i.e., the sacrificial polysilicon layer is thicker around the step corners at the junction where two wafers are bonded. This results in reduced diameter of the conical tip part at the junction where it is connected to the shank cylindrical base as shown in Figure 5.19 which we call it "necking". The formed neck introduces a structural weak point which can potentially degrade mechanical robustness of the electrodes during the implantation and post-implantation.

Figure 5.20 schematically depicts a proposed method to prevent necking by a minor modification to the etched hole sidewall profile. As shown in Figure 5.20 A, the hole entry sidewall is tapered to avoid over-accumulation of LPCVD films at the sharp corners which are responsible for necking.

104
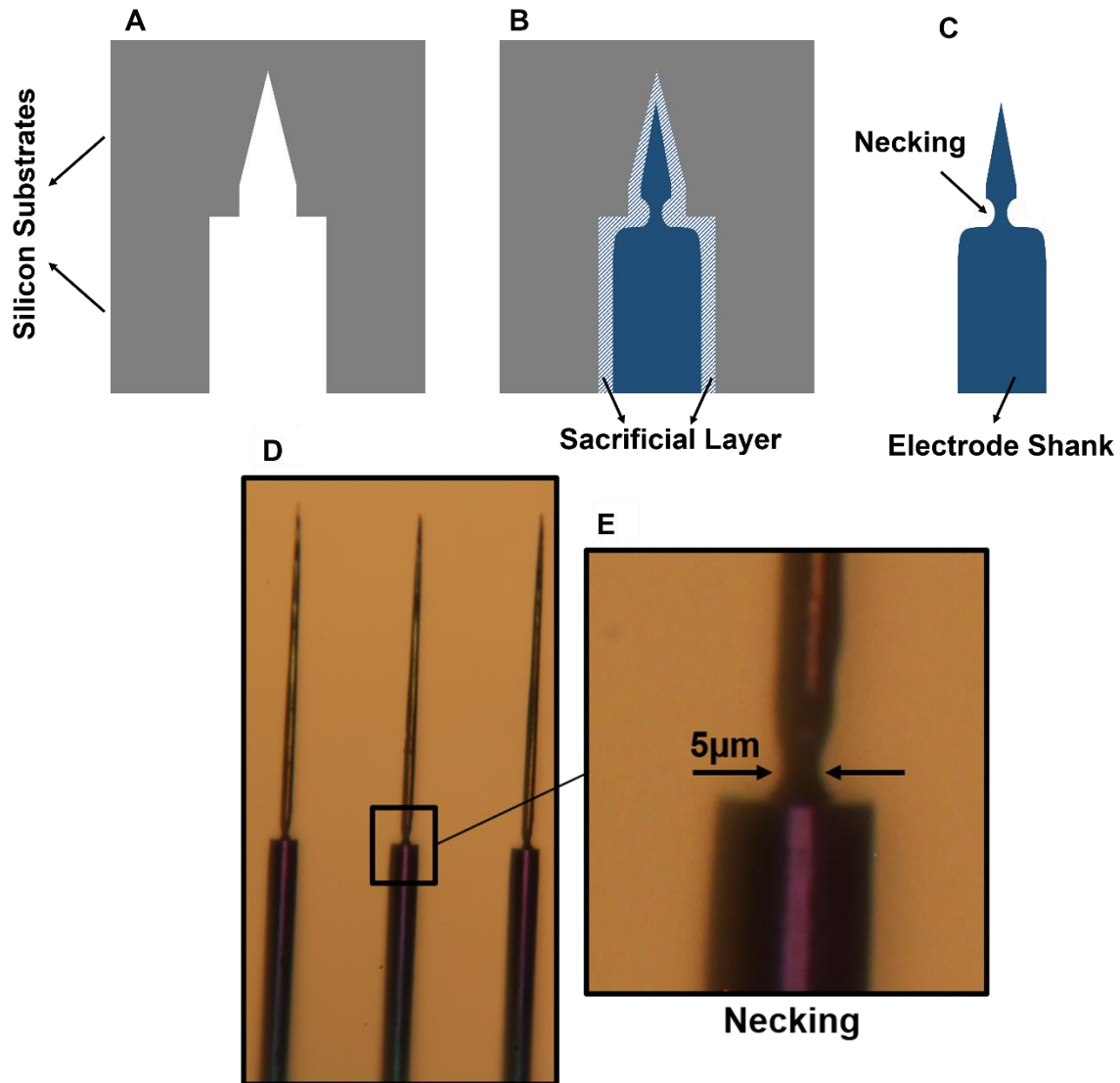
Figure 5.19: Formation of necking along the electrode shank at the bonded wafers junction: (A) Bonded wafers with etched holes prior to refilling by LPCVD films, (B) After refilling with sacrificial layer (LPCVD polysilicon) and other LPCVD films as described in Fig. 3.1, sacrificial polysilicon layer is thicker around the corners at the bonding junctions, (C) Final electrode shank after removing the silicon substrate and sacrificial polysilicon by EDP etching. The polysilicon layer thickness variation around the corners is transferred to the final electrode shank resulting in formation of necking where conical tip part is connected to the shank cylindrical base. (D,E) Optical microscope image of electrodes shank with the close view of necking at the bonding junction.
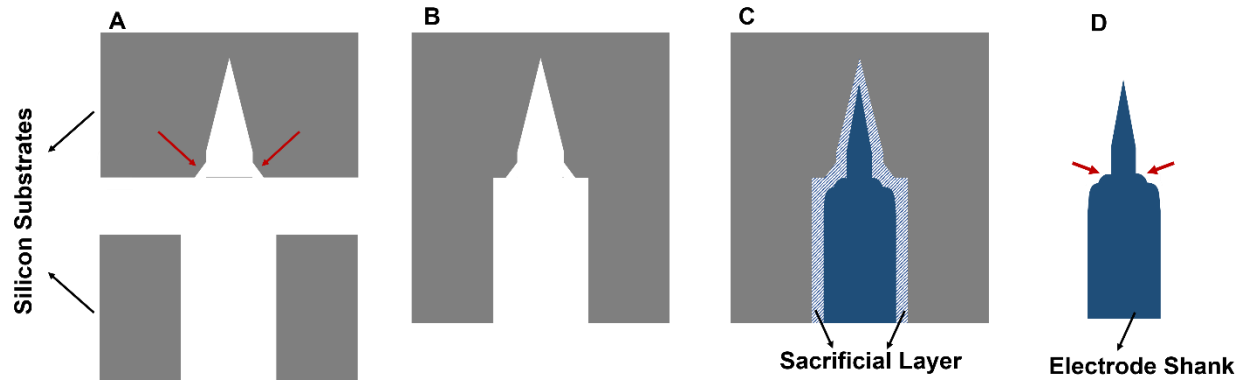
Figure 5.20: Proposed method to prevent formation of necking: (A) Silicon substrates with etched holes before wafer bonding. In the silicon substrate containing the tip holes, the holes entry sidewall is tapered to avoid over-accumulation of LPCVD films at the sharp corners which is responsible for formation of necking, (C) After refilling with sacrificial layer (LPCVD polysilicon) and other LPCVD films as described in Fig. 3.1, sacrificial polysilicon layer is thicker around the corners at the bonding junctions, (D) Final electrode shank after removing the silicon substrate and sacrificial polysilicon by EDP etching. The hole entry sidewall slope is transferred to the final electrode shank profile, increasing the diameter of the conical tip base at the junction of bonded wafers which improves the mechanical robustness of the structure.

5.2.4 Tissue Volume displacement

The penetration of any foreign object into the brain tissue activates the neighboring microglia cells that extend toward the implanted device and start encapsulating the implant. Due to this tissue response, the implant becomes surrounded by microglial cell bodies forming a thin cellular encapsulation that degrades the ionic exchange with the implant electrode site and impacts the chronic stability of the recording [110]. Reducing the cross-sectional dimension of the implanted electrodes will likely reduce the adverse tissue response caused by tissue volume displacement. A smaller displaced tissue volume reduces mechanical strain on the tissue, which reduces the pressure on transmembrane channels and pumps and also reduces the inflammatory tissue response. It has been demonstrated that electrodes with subcellular cross-sectional dimensions improve the electrophysiological recording performance [45,110].

In the case of an electrode array, the total tissue volume displaced by the whole implanted device also needs to be minimized to prevent damage to the brain. Although there is no consensus on the appropriate tissue volume displacement threshold, it is suggested that the displaced tissue volume should be <1% of the brain's volume [111].

In order to approximately determine the upper limits of the SEA array density, we have used a chronically implanted microwire array with similar out-of-plane structure as a reference for safe tissue volume displacement. In one study, Nicolelis et al. chronically implanted 96-704 electrodes of 50 µm diameter with spacing of 300 µm in a macaque monkey and demonstrated 18 months of recording [112]. Figure 5.21(a) shows the array of 96 microwires used in this study, the total volume displacement by this array is ~0.48 mm^3. A SEA array of 2400 electrodes with 10 µm diameter implanted in the same volume (3.5 mm × 3.5 mm opening area and 2.5 mm deep) will result in the same tissue volume displacement which sets the minimum safe spacing to be ~ 60 µm. It is worth mentioning that the tungsten microwires used by Nicolelis et al. had blunt tips while the SEA array electrodes have ultra-sharp tips with a conical tapered sidewall profile near the tip (Figure 5.21 (b) and (c)). This drastically facilitates insertion, reduces dimpling and tissue strain during insertion. Therefore, it is expected to obtain less tissue inflammatory response using SEA arrays compared to the mentioned microwire arrays with larger electrode cross-sectional size and blunt tips.

It is worth mentioning that above discussion has only considered the tissue volume displacement effects on the chronic stability of the brain implant. However, it is widely known that there are many more factors that affect the longevity of the device and the recording. These factors include vasculature damage, insulation material layers failure in the tissue environment, recording sites thin-film metal dissolution and delamination, interconnection fracture along the electrode shank,

107

tissue damage and electrode breakage due to differences of brain and electrode Young's modulus, device tethering and brain micro and macro motions and other explored/unexplored factors.
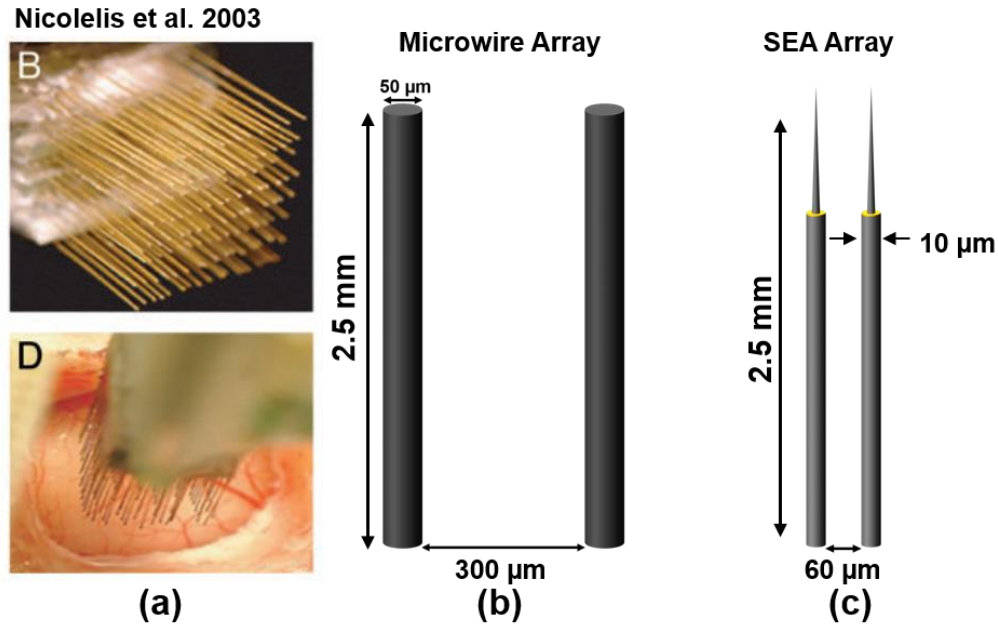
Figure 5.21: Approximate maximum safe electrode array density using a comparison with similar chronically-implanted arrays. (a) A tungsten microwire array of 96 electrodes used by Nicolelis et al. in a chronic recording (18 months) in macaque monkey [112], (b) The microwire array consists of tungsten electrodes of 50 μm diameter and spacing of 300 μm which results in a volume displacement of 0.48 mm^3, (c) SEA array with equivalent tissue volume displacement (0.48 mm^3) with 10 μm diameter electrodes and spacing of ~ 60 μm.

5.3 Conclusions

In this chapter innovative features, potential capabilities, and limitations of the developed SEA technology are discussed. The SEA technology features include:

- Individual needles can have different lengths, and still reside side by side, can be distributed in any arbitrary pattern. Needles can be as tall as several millimeters.

- Needles can have variable pitch/density, capable of being spaced as close as 10 μm.

- Needles can have different shank diameters, to allow design of the stiffness of each shank. Shanks with diameters as small as a few microns can be fabricated.

- A cluster of closely spaced needles with different heights will allow depth recording.

Two techniques have been developed to control the side-by-side electrodes length: The first one utilizes a self-terminating etch process based on the DRIE lag process. In this process the diameter of the side-by-side holes determines the final etch depth, i.e., holes with smaller diameter result in shallower etch depth and therefore shorter electrodes. Using this technique, the maximum variation of length is limited to 500 µm for reasonable hole diameters (<35 µm). To extend the range of electrodes length variation, another technique based on wafer bonding is developed. In the second technique, electrodes length is dependent on the hole layout design in each substrate of the bonded stack. In other words, larger holes (20-35 µm) are replaced by small holes (<10 µm) to form a conical tapered hole instead of thru-wafer holes with straight sidewalls. Depending on the substrates thickness and the relative position of hole sizes reduction along the bonded substrates stack, the final depth of the holes and therefore final electrode shank length is determined. A method for realization of semi-multisite per shank is proposed using closely packed cluster of electrodes with various length to record from different depths along the electrode shank.

As potential capabilities of this technology, modified fabrication process technologies and materials are proposed to achieve other recording and stimulation modalities such as optical and chemical integrated to the electrophysiological electrode arrays.

Some of the limitations of the SEA technology is discussed, these include the LPCVD deposition inside ultra-deep ultra-high-aspect-ratio features, wafer bonding misalignment when making long shanks, and tissue damage when the number and density of shanks increases.

One of the limiting factors that determines the maximum achievable electrodes length is the step coverage of the LPCVD process and the inability to refill very deep holes. Theoretical and modeling analysis is used to determine the LPCVD process step coverage for holes/trenches of various aspect-ratio values. These result suggest maximum electrode length of ~2.5 mm with diameter of ~20 µm can be fabricated.

The issues and limitations caused by the wafer bonding misalignment are discussed and possible solutions are proposed to prevent mechanical and/or electrical failure of the electrode array. These solutions include a progressive electrode shank size and another method, "Bond-then-Align", to circumvent the bond alignment step which causes relatively large misalignment.

Tissue volume displacement caused by the array insertion is used to determine the upper limits of the electrodes density. Comparison with chronically implanted arrays of similar structure (3D out-of-plane microwire array) suggest a maximum density of ~225 electrodes/mm^2 (60 µm electrode spacing) for 10 µm thick electrodes.

Chapter 6: Conclusion and Suggestions for Future Research

The research presented in this thesis involved the design and development of a new silicon-based fabrication technology for producing high-density, large-count, three-dimensional arrays of extremely fine electrodes with user-defined length, width, shape and tip profile. Simultaneous recordings from, and stimulation of, a large number of neurons with high spatiotemporal resolution across multiple spatial planes is crucial to decipher complex neural circuits with causal single cell precision.

Based on the results obtained in this thesis, the following conclusions can be drawn:

1- Near-ideal neural probe features are described as a guideline to design and develop a new electrode array technology. These features include:

- Control over electrodes length, count, distribution and density across the electrode array to obtain 3D spatial coverage.

- High spatial resolution in any arbitrary plane to obtain high-density large-scale electrode arrays.

- Small cross-sectional size with tapered shank sidewall profile and an ultra-sharp tip to minimize tissue damage during and post implantation.

- Multi-modal recording and stimulation of neurons using electrophysiological, optical and chemical methods.

2- Analysis of electrode insertion through the rat brain pia mater using FEM critical buckling load simulations in COMSOL Multiphysics. Simulation results suggest a minimum inner diameter of 10 μm and 14 μm for the base of the cylindrical and conical sections of the electrode shank respectively, and maximum length of 6 mm to ensure pial penetration without buckling. In these simulations the pial penetration force is assumed to be 0.62 mN, therefore, the electrode critical buckling load should be larger than 0.62 mN to prevent buckling/breakage during the insertion.

3- To overcome the shortcomings and issues of previously reported penetrating neural probe technologies, a fabrication process based on refilling deep ultra-high aspect-ratio holes in a silicon substrate with deposited layers followed by etching away the support substrate to leave thousands and eventually millions of needles, is developed.

4- The capabilities and limitations of standard fixed-parameter DRIE process have been tested. These results show that the etch depth for a 25 μm diameter hole is limited to ~ 500 μm due to aspect-ratio dependent etch (ARDE) effect of the DRIE process. Tapering and convergence of the sidewalls due to DRIE lag effect is utilized to form electrodes with tapered shank sidewalls approaching a sharp tip.

5- Electrode arrays with various design parameters are fabricated to demonstrate the capabilities of the proposed technology. This includes arrays with different electrode count (4 - 5184), pitch (50μm-500μm), electrode length (200μm-1.2mm), diameter (10μm-30μm) and arbitrary distribution of electrodes with varying length, pitch, diameter across the array. These results demonstrate our technology capabilities to make high-density large-scale arrays with true 3D spatial coverage which are characteristics of the near-ideal probe described in chapter 2.

6- A method of reducing the final electrode shank cross-sectional size is developed. This method utilizes a sacrificial polysilicon layer deposited inside the etched holes as the first layer deposited using the LPCVD process. This makes the sacrificial polysilicon to be the outermost layer of the electrode shank which will be dissolved during the EDP releasing step, therefore reducing the shank diameter.

7- A modified custom-developed ultra-deep ultra-high aspect-ratio DRIE (UDRIE) process to minimize the standard DRIE process shortcomings (ARDE induced tapered sidewall/etch termination/DRIE lag, and pattern dependency) is developed. Ultra-deep ultra-high AR features with controlled sidewall slope are obtained by dynamically ramping the Bosch DRIE process parameters. The ramp rates of different parameters are set in order to maintain as constant and high etch rate as possible as AR increases. Higher etch rate, larger depth, relatively straight sidewalls and flat bottom are obtained compared to the fixed-parameter recipe. 25 µm diameter holes are etched to >550 µm within 150 min using the ramped-parameter recipe, while 210 min etch by fixed-parameter DRIE recipe only reaches maximum depth of <500 µm.

8- A new fabrication technology based on bonding multiple wafers with thru-wafer holes is developed to obtain arrays with millimeter-long electrodes. This technology uses the ramped-parameter DRIE (UDRIE) process to etch thru-wafer holes in multiple wafers and the standard fixed-parameter DRIE to make the tapered holes. These wafers are aligned and bonded using hydrophilic Si-Si fusion bonding technique to form millimeter-deep holes along the depth of the bonded wafers stack.

9- A method for controlling the length of side-by-side electrodes is developed by using the following processes:

- DRIE lag approach: By changing the hole diameters in the layout, due to the DRIE aspect-ratio dependent etching (ARDE) and DRIE lag effect in holes with various depth and consequently electrodes with various length. The length variation using this process is limited to <500 µm.

- Wafer bonding approach: By engineering the mask layouts used for patterning the holes in each wafer, the length of side-by-side electrodes within a die can be controlled. The length variation using this approach depends on the silicon wafer thickness used in the process.

10- Limitations of refilling approach using LPCVD process have been studied theoretically and experimentally. These results show that the LPCVD process step coverage is drastically reduced as the hole aspect ratio increases. This issue is more severe for LPCVD processes with higher deposition temperature such as oxide and nitride deposition. The modeling results shows the LPCVD step coverage for holes with an aspect ratio of 100 is around 10%.

11- Limitations of the wafer bonding technique in terms of bonding misalignment and the issues caused by it are discussed and two new methods are proposed to prevent these issues.

12- Two maskless self-aligned metallization processes are developed to form the recording sites.

13- Functionalities of the developed SEA array is tested by acute *in vivo* recordings in a rat barrel field cortex using 2×2 and 3×3 arrays. The array was able to seamlessly penetrate the pia mater and tissue with no tissue dimpling or electrode buckling thanks to the sharp needle design of the probes. Local field potentials (LFP) recordings under isoflurane anesthesia showed characteristic slow field potentials, along with occasional epochs of 11 Hz oscillations. Acute histology results showed successful penetration through the white mater with no electrode bending or deviation.

The electrode array technology enables fabrication of customizable application-specific probes for various neural studies. We believe customization of neural probes based on the subject of the study (various species), the target region of the central nervous system, and the neurophysiological study type (acute, chronic) is key for studying different regions of the brain.

We believe the work presented in this thesis has provided solutions to some of the many challenges that prohibit realization of neural interfaces for therapeutics and brain-machine interface applications, however, further research is needed to address the unresolved problems. These include:

1- Fabrication of electrodes with smaller cross-sectional size and longer length using the proposed "bond-then-align" technique. It has been demonstrated that reducing the electrode shank diameter to 10 μm drastically alleviates the tissue inflammatory response. Longer electrodes are required to target deeper neuron-rich brain structures such as hippocampus.

2- Modification of the recording site formation process to improve the recording site impedance, repeatability, and reliability of the sites to obtain chronically stable recordings of single units.

3- Alternative dielectric and conductive materials for improved impedance and stability of electrodes *in vivo*. SiC deposited using PECVD or LPCVD is suggested as the dielectric material to replace the ONO as it has shown great *in vivo* stability in other electrode arrays. Pt, Ir and/or electrodeposited PEDOT is suggested as the recoding site material to improve the impedance and recording signal to noise ratio.

4- Design and development of flexible cables for interconnection and proper encapsulation and packaging. Rivet bonding is suggested to connect the cable to the array for dense high-count arrays

as manual wire bonding results in electrical shorts and reduced yield. Long-term recording in vivo requires proper packaging and encapsulation.

5- Modification of fabrication technology to realize other recording/stimulation modalities such as optical and chemical. Integration of all these modalities (electrophysiological, optical and chemical) in a single probe can provide neuroscientists a great tool to advance our understanding of the brain.

6- Design and development of functional multi-electrode clusters per shank to record from various depths of the brain and drastically increasing the site density with minimal tissue volume displacement.

7- Design and development of customized arrays for specific neural studies to unleash the potential of this technology and realize a near-ideal neural interface. More *in vivo* studies using arrays with various electrode configurations (length, cross-sectional size, density and distribution) are required to further explore the capabilities and limitations of this technology.

In conclusion, I deeply hope that the research presented in this thesis can help neuroscientists and technologists to decipher the brain circuitry and to develop new clinical, therapeutics, and prosthetic devices for different neurological disorders such as epilepsy, depression, addiction and paralysis.

Envisioning a future where brain implants are widely used to help people with mental and physical disabilities to have a normal life or to enhance human cognitive abilities might sound like James Cameron Sci-Fi movies! But, so did contact lenses, pacemakers, cochlear and retina implant in the past.

References

[1]   J. Liu, M. Li, Y. Pan, W. Lan, R. Q. Zheng, F. X. Wu, and J. X. Wang, "Complex brain network analysis and its applications to brain disorders: A survey," *Complexity*, vol. 2017, Article ID 8362741, 27 pages, 2017.

[2]   D. S. Bassett and M. S. Gazzaniga, "Understanding complexity in the human brain," *Trends Cogn. Sci.*, vol. 15, no. 5, pp. 200–209, 2011.

[3]   D. M. Lovinger, "Communication networks in the brain: neurons, receptors, neurotransmitters, and alcohol," *Alcohol Res Health*, vol. 31, no. 3, pp. 196–214, 2008.

[4]   R. G. Budynas, J. K. Nisbett, *Shigley's Mechanical Engineering Design.* (9th edition). New York, NY: McGraw-Hill, 2011

[5]   D. G. Myers, C. N. DeWall, *Psychology in Everyday Life*. (4th edition). New York, NY: Worth Publishers, 2017

[6]   M. P. van den Heuvel, R. S. Kahn, J. Goni, and O. Sporns, "High-cost, high-capacity backbone for global brain communication," *Proc. Natl. Acad. Sci. U.S.A.*, vol. 109, no. 28, pp. 11372–11377, 2012.

[7]   O. Sporns, "The human connectome: Origins and challenges," *NeuroImage*, vol. 80, pp. 53–61, 2013.

[8]   M. G. Mattar and D. S. Bassett, "Brain network architecture: Implications for human learning," preprint arXiv:1609.01790.

[9]   J. Lehrer, "Neuroscience: Making connections," Nature, vol. 457, no. 7229, pp. 524–527, 2009.

[10]   J. Horikawa, A. Hess, M. Nasu, Y. Hosokawa, H. Scheich, and I. Taniguchi, "Optical imaging of neural activity in multiple auditory cortical fields of guinea pigs," *Neuroreport*, vol. 12, no. 15, pp. 3335–3339, 2001.

[11]   N. K. Logothetis, J. Pauls, M. Augath, T. Trinath, and A. Oeltermann, "Neurophysiological investigation of the basis of the fMRI signal," *Nature*, vol. 412, pp. 150–157, 2001.

[12]   F. de Pasquale, S. D. Penna, A. Z. Snyder, C. Lewis, D. Mantini, L. Marzetti, P. Belardinelli, L. Ciancetta, V. Pizzella, G. L. Romani, and M. Corbetta, "Temporal dynamics of spontaneous MEG activity in brain networks," *Proc Natl Acad Sci USA*, vol. 107, no. 13, pp. 6040-6045, 2010.

[13]   R. M. Wightman, L. J. May, and A. C. Michael, "Detection of dopamine dynamics in the brain," *Anal. Chem.*, vol. 60, no. 13, pp. 769A–779A, 1988.

[14]   M. Teplan, "Fundamentals of EEG measurement," *Meas. Sci. Rev.*, vol. 2, sec. 2, 2002.

[15]   G. Buzsáki, C. A. Anastassiou, and C. Koch, "The origin of extracellular fields and currents—EEG, ECoG, LFP and spikes," *Nat. Rev. Neurosci.*, vol. 13, pp. 407–420, 2012.

[16]   B. Rubehn, C. Bosman, R. Oostenveld, P. Fries, and T. Stieglitz, "A MEMS-based flexible multichannel ECoG-electrode array," *J. Neural Eng.*, vol. 6, no. 3, 2009.

[17]   K. D. Wise, J. B. Angell, and A. Starr, "An integrated circuit approach to extracellular microelectrodes," *IEEE Trans. Biomed. Eng.*, vol. BME-17, no. 3, pp. 238–247, 1970.

[18]   K. Najafi, K. D. Wise, and T. Mochizuki, "A high-yield IC compatible multichannel recording array," *IEEE Trans. Electron Devices*, vol. ED-32, no. 7, pp. 1206–1211, 1985.

[19]   P. K. Campbell, K. E. Jones, R. J. Huber, K. W. Horch, and R.A. Normann, "A Silicon-based, three dimensional neural interface: manufacturing processes for an intracortical electrode array," *IEEE Trans. Biomed. Eng.*, vol. 38, no. 8, pp. 758-768, 1991.

[20]   A. C. Hoogerwerf and K. D. Wise, "A Three-dimensional microelectrode array for chronic neural recording," *IEEE Trans. Biomed. Eng.*, vol. 41, no. 12, pp. 1136-1146, 1994.

[21]   C. M. Lopez, J. Putzeys, B. C. Raducanu, M. Ballini, S. Wang, A. Andrei, V. Rochus, R. Vandebriel, S. Severi, C. V. Hoof, S. Musa, N. V. Helleputte, R. F. Yazicioglu, and S. Mitra, "A neural probe with up to 966 electrodes and up to 384 configurable channels in 0.13 μm SOI CMOS," *IEEE Trans. Biomed. Cicruits Syst.*, vol. 11, no. 3, pp. 510-522, 2017.

[22]   J. P. Donoghue, "Bridging the Brain to the World: A Perspective on Neural Interface Systems," Neuron, vol. 60, no. 3, pp. 511-521, 2008.

[23]   A. L. Hodgkin, A. F. Huxley, "Action potentials recorded from inside a nerve fibre," *Nature*, vol. 144, pp. 710-711, 1939.

[24]   M. Hajj Hassan, V. Chodavarapu, and S. Musallam, "NeuroMEMS: Neural probe microtechnologies," *Sensor*s, vol. 8, no. 10, pp. 6704–6726, 2008.

[25]   D. A. Robinson, "The electrical properties of metal microelectrodes," *Proc. IEEE*, vol. 56, no. 6, pp. 1065-1071, 1968.

[26]   C. A. Terzuolo, T. Araki, "An analysis of intra-versus extracellular potential changes associated with activity of single spinal motoneurons," *Ann. NY. Acad. Sci.*, vol. 94, no. 2, pp. 547-558, 1961.

[27]   K. Najafi, K. D. Wise, and T. Mochizuki, "A high-yield IC compatible multichannel recording array," *IEEE Trans. Electron Devices*, vol. ED-32, no. 7, pp. 1206–1211, 1985.

[28]   K. Najafi and K. D. Wise, "An implantable multielectrode array with on-chip signal processing,'' *IEEE J. Solid-State Circuits*, vol. 21, no. 6, pp. 1035-1044, 1986.

[29]   D. J. Anderson, K. Najafi, S. J. Tanghe, D. A. Evans, K. L. Levy, J. F. Hetke, X. L. Xue, J. J. Zappia, and K. D. Wise, "Batch-fabricated thin-film electrodes for stimulation of the central auditory system," IEEE Trans. Biomed. Eng., vol. 36, pp. 693–704, 1989.

[30]   S. J. Tanghe, K. Najafi, and K. D. Wise, "A planar IrO multichannel stimulating electrode for use in neural prostheses," *Sens. Actuators*, vol. B1, pp. 464–467, 1990.

[31]   C. Kim and K. D. Wise, "A 64-site multi-shank CMOS low-profile neural stimulating probe," *IEEE J. Solid-State Circuits*, vol. 31, pp. 1230–1238, 1996.

[32]   K. D. Wise, D. J. Anderson, J. F. Hetke, D. R. Kipke, and K. Najafi, "Wireless implantable microsystems: Electronic interface to the nervous system," *Proc. IEEE (Special Issue on Biomedical Applications for MEMS and Microfluidics)*, pp. 76–97, 2004.

[33]   P. K. Campbell, K. E. Jones, R. J. Huber, K. W. Horch, and R.A. Normann, "A Silicon-based, three dimensional neural interface: manufacturing processes for an intracortical electrode array," *IEEE Trans. Biomed. Eng.*, vol. 38, no. 8, pp. 758-768, 1991.

[34]   K. E. Jones, P. K. Campbell, and R. A. Normann, "A glass/silicon composite intracortical electrode array," *Ann. Biomed. Eng.*, vol. 20, pp. 423–37, 1992.

[35]   R. Bhandari, S. Negi, L. Rieth, and F. Solzbacher, "A wafer-scale etching technique for high aspect ratio implantable MEMS structures," *Sens. Actuators A, Phys.*, vol. 162, pp. 130–136, 2010.

[36]   R. Bhandari, S. Negi, and F. Solzbacher, "Wafer-scale fabrication of penetrating neural microelectrode arrays," *Biomed. Microdevices*, vol. 12, no. 5, pp. 797–807, 2010.

[37] S. J. Kim, S. C. Manyam, D. J. Warren, R. A. Normann, "Electrophysiological mapping of cat primary auditory cortex with multielectrode arrays," *Ann. Biomed. Eng.*, vol. 34, no. 2, pp. 300-309, 2006.

[38] I. H. Stevenson and K. P. Kording, "How advances in neural recording affect data analysis," *Nat. Neurosci.*, vol. 14, no. 2, pp. 139-142, 2011.

[39] J. D. Simeral, S-P. Kim, M. J. Black, J. P. Donoghue, and L. R. Hochberg, "Neural control of cursor trajectory and click by a human with tetraplegia 1000 days after implant of an intracortical microelectrode array," *J. Neural Eng.*, vol. 8, pp. 025027, 2011.

[40] A. B. Ajiboye, F. R. Willett, D. R. Young, W. D. Memberg, B. A. Murphy, J. P. Miller, B. L. Walter, J. A. Sweet, H. A. Hoyen, M. W. Keith, P. Hunter Peckham, J. D. Simeral, J. P. Donoghue, and L. R. Hochberg, and R. F. Kirsch, "Restoration of reaching and grasping movements through brain-controlled muscle stimulation in a person with tetraplegia: a proof-of-concept demonstration," *The Lancet*, vol. 389, pp. 1821-1830, 2017.

[41] J. Scholvin, J. P. Kinney, J. G. Bernstein, C. Moore-Kochlacs, N. Kopell, C. G. Fonstad, and E. S. Boyden, "Close-packed silicon microelectrodes for scalable spatially oversampled neural recording," *IEEE Trans. Biomed. Eng.*, vol. 63, no. 1, pp. 120-130, 2016.

[42] D. A. Schwarz, M. A. Lebedev, T. L. Hanson, D. F. Dimitrov, G. Lehew, J. Meloy, S. Rajangam, V. Subramanian, P. J. Ifft, Z. Li, A. Ramakrishnan, A. Tate, K. Z. Zhuang, and M. A. L. Nicolelis, "Chronic, wireless recordings of large-scale brain activity in freely moving rhesus monkeys," *Nat. Methods*, vol. 11, no. 6, pp. 670-679, 2014.

[43] M. A. L. Nicolelis, *Methods for Neural Ensemble Recordings.* (1st edition). Boca Raton, FL: CRC Press, 1999.

[44] M. Armstrong-James, J. Millar, "Carbon fibre microelectrodes," *J. Neurosci. Methods.*, vol. 1, no. 3, pp. 279– 87, 1979.

[45] T. D. Y. Kozai, N. Langhals, P. R. Patel, X. Deng, H. Zhang, K. L. Smith, J. Lahann, N. A. Kotov, and D. R. Kipke, "Ultrasmall implantable composite microelectrodes with bioactive surfaces for chronic neural interfaces," *Nat. Mater.*, vol. 11, pp. 1065–1073, 2012.

[46] G. Guitchounts, J. E. Markowitz, W. A. Liberti, and T. Gardner, "A carbon-fiber electrode array for long-term neural recording," *J. Neural Eng.*, vol. 10, no. 4, Art. no. 046016, 2013.

[47]   P. R. Patel, K. Na, H. Zhang, T. D .Y. Kozai, N. A. Kotov, E.Yoon, and C. A. Chestek, "Insertion of linear 8.4μm diameter 16 channel carbon fiber electrode arrays for single unit recordings," *J. Neural Eng.*, vol. 12, art. no. 046009, 2015.

[48]   B. Tian, J. Liu, T. Dvir, L. Jin, J. H. Tsui, Q. Qing, Z. Suo, R. Langer, D. S. Kohane, and C. M. Lieber, "Macroporous nanowire nanolelectronic scaffolds for synthetic tissues," *Nat. Mater.*, vol. 11, pp. 986-994, 2012.

[49]   J. Liu, C. Xie, X. Dai, L. Jin, W. Zhou, and C. M. Lieber, "Multifunctional three-dimensional macroporous nanoelectronic networks for smart materials," *Proc. Natl. Acad. Sci. U. S. A.*, vol. 110, no. 17, pp. 6694-6699, 2013.

[50]   C. Xie, J. Liu, T.Fu, X. Dai, W. Zhou, and C. M. Lieber, "Three-dimensional macroporous nanoelectronic networks as minimally invasive brain probes," *Nat. Mater.*, vol. 14, pp. 1286-1292, 2015.

[51]   H. A. C. Wark, R. Sharma, K. S. Mathews, E. Fernandez, J. Yoo, B. Christensen, P. Tresco, L. Rieth, F. Solzbacher, and R. A. Normann, "A new high-density (25 electrodes/mm^2) penetrating microelectrode array for recording and stimulating sub-millimeter neuroanatomical structures," *J. Neural Eng.*, vol. 10, no. 4, 045003, 2013.

[52]   A. C. Hoogerwerf and K. D. Wise, "A Three-dimensional microelectrode array for chronic neural recording," *IEEE Trans. Biomed. Eng.*, vol. 41, no. 12, pp. 1136-1146, 1994.

[53]   M. D. Gingerich, J. F. Hetke, D. J. Anderson, and K. D. Wise, "A 256-site 3D CMOS microelectrode array for multipoint stimulation and recording in the central nervous system," *Int. Conf. Solid-State Sensors and Actuators*, Munich, Germany, 2001.

[54]   Y. Yao, M. N. Gulari, J. F. Hetke, and K. D. Wise, "A self-testing multiplexed CMOS stimulating probe for a 1024-site neural prosthesis," *Proc. IEEE Int. Conf. Solid-State Sensors, Actuators, and Microsystems (Transducers'03)*, pp. 1213–1216. 2003.

[55]   G. Rios, E. V. Lubenov, D. Chi, M. L. Roukes, and A. G. Siapas, "Nanofabricated neural probes for dense 3-D recordings of brain activity," *Nano Lett.*, vol. 16, pp. 6857-6862, 2016.

[56]   J. P. Seymour, F. Wu, K. D. Wise, E. Yoon, "State-of-the-art MEMS and microsystem tools for brain research," *Microsyst. Nanoeng.*, vol. 3, 16066 , 2017.

[57] P. R. Patel, H. Zhang, M. T. Robbins, J. B. Nofar, S. P. Marshall, M. J. Kobylarek, T. D. Y. Kozai, N. A. Kotov, C. A. Chestek, "Chronic *in vivo* stability assessment of carbon fiber microelectrode arrays," *J. Neural Eng.*, vol. 13, Art. no. 066002, 2016.

[58] J. J. Clark, S. G. Sandberg, M. J. Wanat, J. O. Gan, E. A. Horne, A. S. Hart, C. A. Akers, J. G. Parker, I. Willuhn, V. Martinez, S. B. Evans, N. Stella, amd P. E. Phillips, "Chronic microsensors for longitudinal, subsecond dopamine detection in behaving animals," *Nat. Mater.*, vol. 7, pp. 126-129, 2010.

[59] S. F. Bernatchez, P. J. Parks, and D. F. Gibbons, "Interaction of macrophages with fibrous materials in vitro," *Biomaterials*, vol. 17, no. 21, pp. 2077–2086, 1996.

[60] J. E. Sanders, C. E. Stiles, and C. L. Hayes. "Tissue response to single-polymer fibers of varying diameters: evaluation of fibrous encapsulation and macrophage density," *J. Biomed. Mater. Res.*, vol. 52, no.1, pp. 231–237, 2000.

[61] B. Ghane Motlagh, M. Choueib, A. Hajhosseini Mesgar, M. Hasanuzzaman, M. Sawan, "Direct growth of carbon nanotubes on new high-density 3D pyramid-shaped microelectrode arrays for brain-machine interfaces," *Micromachines*, vol. 7, no. 9, p. 163, 2016**.**

[62] C. M. Owen, A. Howard, and D. K. Binder, "Hippocampus minor, calcar avis, and the Huxley-Owen debate," *Neurosurgery*, vol. 65, no. 6, pp. 1098–1105, 2009.

[63] A. Mouritzen Dam, "The density of neurons in the human hippocampus," *Neuropathol. Appl. Neurobiol.*, vol. 5, pp. 249-264, 1979.

[64] B. A. Strange, M. P. Witter, E. S. Lein, and E. I. Moser, "Functional organization of the hippocampal longitudinal axis," *Nature Rev. Neurosci.*, vol. 15, pp. 655–669, 2014.

[65] S. P. Marshall, W. Lin, P. R. Patel, A. J. Shih, and C. A. Chestek, "Effects of geometry and material on the insertion of very small neural electrode," *IEEE 38th Annual Int. Conf. of the Engineering in Medicine and Biology Society (EMBC)*, pp. 2784–8, 2016.

[66] J. P. Harris, A. E. Hess, S. J. Rowan, C. Weder, C. A. Zorman, D. J. Tyler, J. R. Capadona, "In vivo deployment of mechanically adaptive nanocomposites for intracortical microelectrodes," *J. Neural Eng.*, vol. 8, no. 4, Art. no. 046010, 2011.

[67] W. Jensen, K. Yoshida, U. G. Hofmann, "In-vivo implant mechanics of flexible, silicon-based ACREO microelectrode arrays in rat cerebral cortex," *IEEE Trans. Biomed. Eng.*, vol. 53, pp. 934–940, 2006

[68] B. A. Wester, R. H. Lee, M. C. LaPlaca, " Development and characterization of in vivo flexible electrodes compatible with large tissue displacements," *J. Neural Eng.*, vol. 6, Art. no. 024002, 2009.

[69] M. A. Howard, B. A. Abkes, M. C. Ollendieck, M. D. Noh, C. Ritter, G. T. Gillies, "Measurement of the force required to move a neurosurgical probe through in vivo human brain tissue," *IEEE Trans. Biomed. Eng.*, vol. 46, pp. 891–894, 1999.

[70] J. A. Molloy, R. C. Ritter, M. S. Grady, M. A. Howard, E. G. Quate, G. T. Gillies, "Experimental determination of the force required for insertion of a thermoseed into deep brain tissues," *Ann. Biomed. Eng.*, vol. 18, pp. 299–313, 1990.

[71] C. X. Tian, J. He, "Monitoring insertion force and electrode impedance during implantation of microwire electrodes," in *Proc. IEEE conf. Eng. Med. Biol. Soc.*, pp. 7333–7336. 2005.

[72] F. Deku, C. L. Frewin, A. Stiller, Y. cohen, S. Aqeel, A. Joshi-Imre, B. Black, T. J. Gardner, J. J. Pancrazio, and S. F. Cogan, "Amorphous silicon carbide platform for next generation penetrating neural interface design," *Micromachines*, vol. 9, no. 10, p. 480, 2018.

[73] A. Andrei, M. Welkenhuysen, B. Nuttin, W. Eberle, "A response surface model predicting the in vivo insertion behavior of micromachined neural implants," *J. Neural Eng.*, vol. 9, Art. no. 016005, 2011.

[74] N. H. Hosseini, R. Hoffmann, S. Kisban, T. Stieglitz, O. Paul, P. Ruther, "Comparative study on the insertion behavior of cerebral microprobes," in *Proc. IEEE conf. Eng. Med. Biol. Soc.*, pp. 4711–4714, 2007.

[75] A. Weltman, J. Yoo, and E. Meng, "Flexible, penetrating brain probes enabled by advances in polymer microfabrication," *Micromachines*, vol. 7, no. 10, p. 180, 2016.

[76] D. J. Edel, V. Toi, V. M. McNeil, L. D. Clark, "Factors influencing the biocompatibility of insertable silicon microshafts in cerebral cortex," *IEEE Trans. Biomed. Eng.*, vol. 39, pp. 635–643, 1992.

[77] K. Najafi and J. F. Hetke, "Strength characterization of silicon microprobes in neurophysiological tissues," *IEEE Trans. Biomed. Eng.*, vol. 37, pp. 474–481, 1990.

[78] P. Schiavone, F. Chassat, T. Boudou, E. Promayon, F. Valdivia, Y. Payan, "In vivo measurement of human brain elasticity using a light aspiration device," *Med. Image Anal.*, vol. 13, no. 4, pp. 673–678, 2009.

[79] A. Olamat, N. Nkemasong, B. Pohl and U. Hofmann, "Physical and FEM Simulation of Microprobe Insertion into Rat Brain," in *COMSOL Conference*, Paris, 2010.

[80] M. Hrapko, J. A. W. Van Dommelen, G. W. M. Peters, J. S. H. M. Wismans "On the consequences of non linear constitutive modelling of brain tissue for injury prediction with numerical head models," *Int. J. Crashworthiness*, vol. 14, no. 3, pp. 245–257, 2009

[81] L. E. Bilston, *Neural tissue biomechanics Studies in Mechanobiology, Tissue Engineering, and Biomaterials*. (3rd edition). New York, NY: Springer.

[82] R. C. Ritter, E. G. Quate, G. T. Gillies, M. S. Grady, M. A. Howard, and W. C. Broaddus, "Measurement of friction on straight catheters in *in vitro* brain and phantom material," *IEEE Trans. Biomed. Eng.*, vol. 45, no. 4, pp. 476–485, 1998.

[83] Y. Tang, A. Sandoughsaz, K. J. Owen, and K. Najafi, "Ultra deep reactive ion etching (UDRIE) of high aspect-ratio and thick silicon using a ramped-parameter process," J. Microelectromech. Syst., vol. 27, no. 4, pp. 686-697, 2018

[84] Y. Tang, A. Sandoughsaz, K. Najafi, "Ultra high aspect-ratio and thick deep silicon etching (UDRIE)," in *Proc IEEE MEMS*, Las Vegas, NV, USA, pp. 700-703, 2017.

[85] K. J. Owen, B. VanDerElzen, R. L. Peterson, and K. Najafi, "High aspect ratio deep silicon etching," in *Proc IEEE MEMS*, Paris, France, Jan. 2012.

[86] P. W. Barth, "Silicon fusion bonding for fabrication of sensors, actuators and microstructures," *Sens. Actuators*, vol. 23, pp. 919–926, 1990.

[87] Z. Liu and D. L. DeVoe, "Micromechanism fabrication using silicon fusion bonding," *Robot. Comput. Integr. Manuf.*, vol. 17, pp. 131–137, 2001.

[88] D. Graf, M. Grundner, R. Schulz, "Reaction of water with hydrofluoric acid treated silicon (1 1 1) and (1 0 0) surfaces," *J. Vac. Sci. Technol. A*, vol. 7, no. 3, pp. 808-813, 1989.

[89] Q. Y. Tong, U. Gosele, and M. Reiche, "Hydrophobic silicon wafer bonding," *Appl. Phys. Lett.*, vol. 64, no. 4, pp. 625-627, 1994.

[90] K. Petersen, P. Barth, J. Poydock, J. Mallon, and J. Bryzek, "Silicon fusion bonding for pressure sensors," in *Tech. Dig. IEEE Solid-State Sensor and Actuator Workshop*, Hilton Head, SC, p. 144, 1988.

[91] C. Harendt, H. G. Graf, B. Höfflinger, and J. E. Penteker, "Silicon fusion bonding and its characterization," *J. Micromech. Microeng.*, vol. 2, pp. 113–116, 1992.

[92]   G. Kissinger, W. Kissinger, "Void-free silicon-wafer-bond strengthening in the 200-400 C range," Sens. Actuators A, vol. 36, pp. 149-156, 1993.

[93]   S. N. Farrens, J. R. Dekker, J. K. Smith, and B. E. Roberds, "Chemical free room temperature wafer to wafer direct bonding," *J. Electrochem. Soc.*, vol. 142, no. 11, p. 3949, 1995.

[94]   Q. Y. Tong and U. Gösele (1998). The Electrochemical Society, ed. Semiconductor Wafer Bonding: Science and Technology (1st edition). Wiley-Interscience.

[95]   B. Lustig, Y. Wang, and E. Pastalkova, "Oscillatory patterns in hippocampus under light and deep isoflurane anesthesia closely mirror prominent brain States in awake animals," *Hippocampus*, vol. 26, no. 1, pp. 102-109, 2016.

[96]   B. Wu, A. Kumar, and S. Pamarthy, "High aspect ratio silicon etch: A review," *J. Appl. Phys.*, vol. 108, no. 5, p. 051101, 2010.

[97]   S. Tachi, K. Tsujimoto, and S. Okudaira, "Low-temperature reactive ion etching and microwave plasma etching of silicon," *Appl. Phys. Lett.*, vol. 52, no. 8, pp. 616–618, 1988.

[98]   M. J. D. Boer et al., "Guidelines for etching silicon MEMS structures using fluorine high-density plasmas at cryogenic temperatures," *J. Microelectromech. Syst.*, vol. 11, no. 4, pp. 385–401, 2002.

[99]   A. Sandoughsaz, S. Azimi, H. Mazreati, and S. Mohajerzadeh, "Realization of complex three-dimensional free-standing structures on silicon substrates using controllable underetching in a deep reactive ion etching," *J. Micromech. Microeng.*, vol. 23, no. 3, p. 035022, 2013.

[100] S. Azimi, A. Sandoughsaz, B. Amirsolaimani, J. Naghsh-Nilchi, and S. Mohajerzadeh, "Three-dimensional etching of silicon substrates using a modified deep reactive ion etching technique," *J. Micromech. Microeng.*, vol. 21, no. 7, p. 074005, 2011.

[101] M. Gharooni, A. Mohajerzadeh, A. Sandoughsaz, S. Khanof, S. Mohajerzadeh, and E. Asl-Soleimani, "A novel non-sequential hydrogen-pulsed deep reactive ion etching of silicon," *J. Micromech. Microeng.*, vol. 23, no. 9, p. 095014, 2013

[102] S. Azimi, A. Sandoughsaz, and S. Mohajerzadeh, "Realization of three-dimensional Si and SiO_2 nanowall structures using reactive ion etching," *J. Microelectromech. Syst.*, vol. 20, no. 2, pp. 353–354, 2011.

[103]   L. Luan, X. Wei, Z. Zhao, J. J. Siegel, O. Potnis, C. A. Tuppen, S. Lin, S. Kazmi, R. A. Fowler, S. Holloway, A. K. Dunn, R. A. Chitwood, and C. Xie, "Ultraflexible nanoelectronic probes form reliable, glial scar–free neural integration," *Sci. Adv.*, vol 3, p. e1601966, 2017.

[104]   K. Deisseroth, "Optogenetics," *Nat. Methods*, vol. 8, no. 1, pp. 26-29, 2011.

[105]   H. J. Lee, Y. Son, J. Kim, C. J. Lee, E. Yoon, and I. Cho, "A multichannel neural probe with embedded microfluidic channels for simultaneous in vivo neural recording and drug delivery," *Lab chip*, vol. 15, no. 6, pp. 1590-1597, 2015.

[106]   K. Watanabe and H. Komiyama, "Micro/marcocavity method applied to the study of the step coverage formation mechanism of SiO2 films by LPCVD," *J. Electrochem. Soc.*, vol. 137, no. 4, p. 1222, 1990.

[107]   A. Hasper, J. Hollemann, J. Middelhoek, C. R. Kleijn, and C. J. Hoogendoorn, "Modeling and optimization of the step coverage of tungsten LPCVD in trenches and contact holes," *J. Electrochem. Soc.*, vol. 138, no. 6, pp. 1728-1738, 1991.

[108]   H. Komiyama, Y. Shimogaki, and Y. Egashira, "Chemical reaction engineering in the design of CVD reactors," *Chem. Eng. Sci.*, vol. 54, pp. 1941-1957, 1999.

[109]   S. H. Lee, K. N. Chen, and J. J. Q. Lu, "Wafer-to-wafer alignment for three-dimensional integration: A review," *J. Microelectromech. Syst.*, vol. 20, no. 4, pp. 885–898, 2011.

[110]   T. D. Y. Kozai, A. S. Jaquins-Gerstl, A. L. Vazquez, A. C. Michael, and X. T. Cui, "Brain tissue responses to neural implants impact signal sensitivity and intervention strategies," *ACS Chem. Neurosci.*, vol. 6, pp. 48–67, 2015.

[111]   A. H. Marblestone, B. M. Zamft, Y. G. Maguire, M. G. Shapiro, T. R. Cybulski, J. I. Glaser, D. Amodei, P. B. Stranges, R. Kalhor and D. A. Dalrymple, "Physical principles for scalable neural recording," *Frontiers in Computational Neuroscience*, vol. 7, 2013.

[112]   M. A. Nicolelis, D. Dimitrov, J. M. Carmena, R. Crist, G. Lehew, J. D. Kralik, and S. P. Wise, "Chronic, multisite, multielectrode recordings in macaque monkeys," *Proc. Nat. Acad. Sci.*, vol. 100, pp. 11041–11 046, 2003.

[113]   D. E. Gunning, J. M. Beggs, W. Babrowski, P. Hottowy. C.J. Kenney, A. Sher, A. M. Litke, and K. Mathieson, " Dense arrays of micro-needles for recording and electrical stimulation of neural activity in acute brain slices," *J. Neural Eng.*, vol. 10, Art. no. 016007, 2013.